STUDY OF WHITE LIGHT CAVITY EFFECT VIA STIMULATED BRILLOUIN SCATTERING INDUCED FAST LIGHT IN A FIBER RING RESONATOR

A Dissertation

by

HO NAM YUM

Submitted to the Office of Graduate Studies of
Texas A&M University
in partial fulfillment of the requirements for the degree of

DOCTOR OF PHILOSOPHY

August 2009

Major Subject: Electrical Engineering

STUDY OF WHITE LIGHT CAVITY EFFECT VIA STIMULATED BRILLOUIN SCATTERING INDUCED FAST LIGHT IN A FIBER RING RESONATOR

A Dissertation

by

HO NAM YUM

Submitted to the Office of Graduate Studies of
Texas A&M University
in partial fulfillment of the requirements for the degree of

DOCTOR OF PHILOSOPHY

Approved by:

Chair of Committee,	Philip Hemmer
Committee Members,	Laszlo Kish
	Robert D. Nevels
	George R. Welch
Head of Department,	Costas N. Georghiades

August 2009

Major Subject: Electrical Engineering

ABSTRACT

Study of White Light Cavity Effect via Stimulated Brillouin Scattering Induced Fast Light in a Fiber Ring Resonator. (August 2009)

Ho Nam Yum, B.S., Yonsei University, Republic of Korea;

M.S., Texas A&M University

Chair of Advisory Committee: Dr. Philip Hemmer

Techniques to control dispersion in a medium have attracted much attention due to potential applications to devices such as ring laser gyroscopes, interferometric gravitational wave detectors, data buffers, phased array radars and quantum information processors. Of particular interest is an optical resonator containing a medium with an anomalous dispersion corresponding to fast-light, which behaves as a White Light Cavity (WLC). A WLC can be tailored to improve the sensitivity of sensing devices as well as to realize an optical data buffering system that overcomes the delay-bandwidth product of a conventional cavity.

This dissertation describes techniques to tailor the dispersion for fast-light in intracavity media. We present first a demonstration of fast-light in a photorefractive crystal. When placed inside a cavity, such a medium could be used to enhance the bandwidth of a gravitational wave detector. We then describe how a superluminal laser can be realized by adding anomalously dispersive medium inside a ring laser. We identify theoretical conditions under which the sensitivity of the resonance frequency to

a change in the cavity length is enhanced by as much as seven orders of magnitude. This paves the way for realizing a fast-light enhanced ring laser gyroscope, for example. This is followed by the development of a novel data buffering system which employs two WLC systems in series. In this system, a data pulse can be delayed an arbitrary amount of time, without significant distortion. The delay time is independent of the data bandwidth, and is limited only by the attenuation experienced by the data pulse as it bounces between two high-reflectivity mirrors. Such a device would represent a significant breakthrough in overcoming the delay-time bandwidth product limitation inherent in conventional data buffers.

We then describe our experimental effort to create a fiber-based WLC by using stimulated Brillouin scattering (SBS). Experimental results, in agreement with our theoretical model presented here, show that the WLC effect is small under the conditions supported by current fiber optic technology. We conclude that future efforts to induce a large WLC effect would require fibers with high Brillouin coefficient and low transmission loss, as well as optical elements with very low insertion loss and high power damage thresholds.

DEDICATION

To my parents and family

ACKNOWLEDGEMENTS

This dissertation is a product of cooperation. I could not finish this dissertation without my family, mentors and friends. I would like to express special thanks to my advisor, Dr. Philip Hemmer, for providing me exposure and the opportunity to work in various technical areas. In addition, I want to thank Dr. Selim Shahriar, at Northwestern University. He showed me what scientists pursue. I also learned from him how to explain and how to tackle some of the hardest problems in engineering, science and even affairs that humans stumble on. I also give many thanks to Dr. Mary Salit and Dr. Ken Salit. They were Dr. Shahriar's students. Dr. Ken Salit helped me settle down here at Northwestern. It was my pleasure to work with Dr. Mary Salit on the super-sensitive gyroscope project. I would like to give special thanks to Shih Tseng and May Kim. Shih gave me many solutions to circuit problems for Laser Diode. May revised this dissertation. I also learned a lot from my colleagues, Dr. Zhijie Deng, Dr. Mughees Khan, Dr. Chang-Seok Shin, Huiliang Zhang, and Chang-Dong Kim (Both are soon to be Dr.). I want to thank my previous committee members, Dr. Ohannes Eknoyan, Dr. Suhail Zubairy, and current committee members, Dr. Laszlo Kish, Dr. Robert Nevels, and Dr. George Welch, for their valuable instruction.

I give special thanks to my family. They are permanent supporters in my life. My parents make it possible for me to be where I am now. Haeyoon, as my wife, friend, and sometimes colleague, in my life helped me overcome the hardest moments. Finally, special thanks to my sister and my beautiful daughter, Emily.

TABLE OF CONTENTS

CHAPTER Page

LIST OF FIGURES

FIGURE Page

FIGURE Page

FIGURE Page

FIGURE Page

FIGURE Page

FIGURE Page

FIGURE Page

CHAPTER I

INTRODUCTION

Fast-light and slow-light have been of significant interest to scientific community for the last decade. A number of experimental demonstrations have been reported based on electromagnetically induced transparency (EIT) in cold atomic vapor [1], [2] or solid [3], stimulated Raman scattering in hot atomic vapor [4] two wave mixing in photorefractive crystal [5] and stimulated Brillouin scattering(SBS) in fibers [6], [7]. Significant research activities in these fields are still ongoing due to numerous potential applications such as optical buffers, optical variable delay lines, optical memories, quantum information processing, gravitational wave detection, and super-sensitive rotation sensing.

The study presented in this dissertation is about finding the method to create slow- and fast-light effect inside optical cavities for the application to gravitational wave detection, data buffering system, and rotation sensing. In order to see how these applications emerge and the related issued, it is important first to review the basic concepts of dispersion and fast- and slow-light, the White light cavity (WLC) effect.

If light propagates in a material with refractive index n, its wavelength is given by λ/n, where λ is the wavelength in vacuum. In general, the refractive index varies with the frequency of light, a process known as dispersion. In some materials, it can be large as well as artificially controlled by applying external optical beams. Under certain conditions, dispersion can have significant effects on optical pulses made up of many

This dissertation follows the style and format of IEEE *Transactions on Antennas and Propagation.*

frequency components. Each individual frequency component feels a different refractive index and thus experiences a different phase shift. The peak of the pulse coincides with the point where all constituent waves meet in phase. The point where the in-phase condition occurs can move faster (in a fast-light medium) or slower (in a slow-light medium) than it would in free space. As such, the optical pulse is seen to propagate in such a medium faster or slower than the speed of light in free space, corresponding to so-called superluminal (fast-light) or subliminal (slow-light) propagation, respectively. In the case of fast-light argument, one might worry about violating Special Relativity. However, since information is encoded in the leading edge of a pulse, corresponding to a bandwidth that always exceeds the bandwidth of any dispersion, information cannot be sent faster than the free space speed of light, so that there is no violation of Special Relativity.

The presence of a fast-light medium can modify the behavior of an optical cavity very significantly. Consider an optical cavity consisting of two high reflectivity partial mirrors. If the length corresponds to an integer times the wavelength of light, the cavity is said to be on resonance, and any light incident on it will transmit fully. Now, consider the same cavity filled with a fast-light medium. The index variation can be tailored in a way so that a large range of frequencies would have the same wavelength. If this wavelength fulfills the resonance condition, the cavity will resonate over the whole frequency range. At resonance, the light intensity builds up in the cavity. In general, the build-up factor is inversely proportional to the cavity linewidth, both being due to the finite losses and mirror transmittance. In the presence of the fast-light medium, the

cavity linewidth becomes broader, while the buildup factor remains unchanged. In other words, the cavity lifetime remains the same as before, since the losses and the mirror transitivity remain unchanged. This phenomenon is called the 'White Light Cavity' (WLC) effect. The system described here is called a passive WLC. In contrast, an active WLC is a cavity with similar properties, but contains an active gain material as well.

The dissertation is organized as follows. In chapter II, we demonstrate superluminal and subluminal pulse propagation using a photorefractive crystal. We use bi-frequency pumps to produce the anomalous dispersion. Fast-light in such a medium can be used to enhance the bandwidth of a gravitational wave interferometer without reducing its sensitivity.

In chapter III, we theoretically investigate fast-light in a laser cavity, i.e. an active WLC. We use a narrowband depletion embedded in broadband gain to produce the necessary dispersion for the fast-light. The broadband gain is provided by the active gain medium. For the application to gyroscope, the resonance property of the cavity is discussed. The active WLC exhibits high sensitivity to cavity length change such that it provides the prospect to realize a super-sensitive optical gyroscope.

In chapter IV and V, we propose a data buffering system using a pair of passive WLCs. The probe pulse corresponds to a data pulse. In the basic model, a Fabry-Perot (FP) cavity is used to realize each WLC. Numerical simulation indicates that the data pulse is delayed by thousands times the pulse duration, for a given choice of parameters. Other choices would lead to even longer storage time. The proposed buffering system exceeds the delay time-bandwidth product constraint encountered in a conventional data

buffer. Next, we describe the design of a buffering system based on fiber ring resonators. The SBS process can be used to control the dispersion [6]~[9] in a fiber resonator. As such, the fiber itself can become the fast-light medium. For the data buffer, two fiber resonators are connected in series. The pump beams are inserted into the resonators to turn them into passive WLCs. As in the FP based system, the delay time can be controlled independently of the bandwidth of the data pulses. Furthermore, we describe how the bandwidth of the system can be extended to be as large as several times the Brillouin frequency shift of nearly 10 GHz in a typical fiber.

In chapters VI and VII, we investigate the parameter constraints in realizing a passive WLC in fiber resonators. First, we measure the Brillouin characteristics of a conventional silica fiber. We describe the construction of a fiber resonator and the experimental demonstration of a passive WLC. In the experiment, the amount of linewidth broadening (i.e., WLC effect) observed is rather small, in agreement with the theoretical model Numerical analysis indicates that, using the current approach, a fiber with a high Brillouin coefficient and a low transmission loss, as well as fiber components with high damage thresholds are required to induce large WLC effect in fiber resonators. However, current fiber fabrication techniques do not yet yield such a fiber. For future works, we propose an alternative experimental setup to realize an efficient WLC under conditions which current fiber technology can support.

CHAPTER II

FAST LIGHT DEMONSTRATION IN A PHOTOREFRACTIVE CRYSTAL

A. Pulse propagation and group velocity

Scientists have discovered that a pulse can propagate extremely slower or faster than the speed of light in vacuum [1], [2], [4], [10]. To explain this observation, it is crucial to understand the nonperiodic wave and the group velocity.

Fig. 2.1 displays that the addition of two sine waves with different frequencies produce the beating output wave. The amplitude of the resultant wave becomes zero when two waves are completely out-of-phase. It gives maximum value as the two waves return in-phase. This phenomenon occurs periodically and it is called beating.

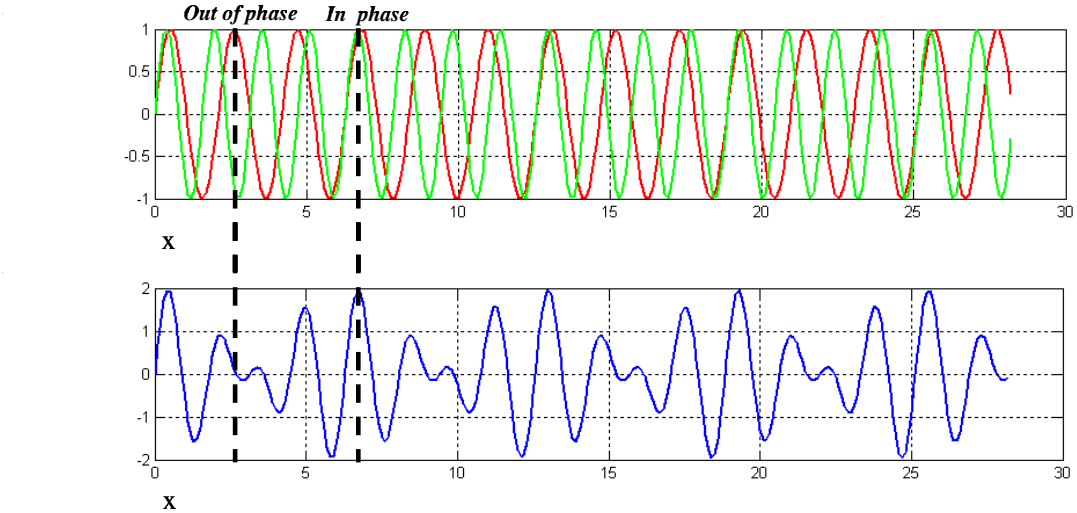

Fig. 2.1. Superposition of two sine waves sin(3***x***) (green) and sin(4***x***) (red) produces the beating (blue).

Let us extend this concept to a pulse made up of multiple frequencies. Fig. 2.2(a)~(e) illustrate how the localized pulse is generated [11]. As adding more frequency components, the separation between the neighboring beats increases. Note that a carrier frequency is equal to the average frequency of the harmonic components. If one adds more harmonics symmetrically around ω_0, the beats (envelopes for the carrier wave) separate more without changing the carrier frequency. Fig. 2.2(e) illustrates the amplitude of the perfectly localized pulse. If the spectrum of the sinusoidal harmonics is continuous, the sinusoids are in-phase in the localized region and out-of phase everywhere except over such a localized region. A single solitary pulse remains i.e. the pulse is localized. The amplitudes of the harmonics are enveloped with the Gaussian spectrum centered at ω_0 and thus the addition of the harmonics generates the Gaussian enveloped pulse in time domain.

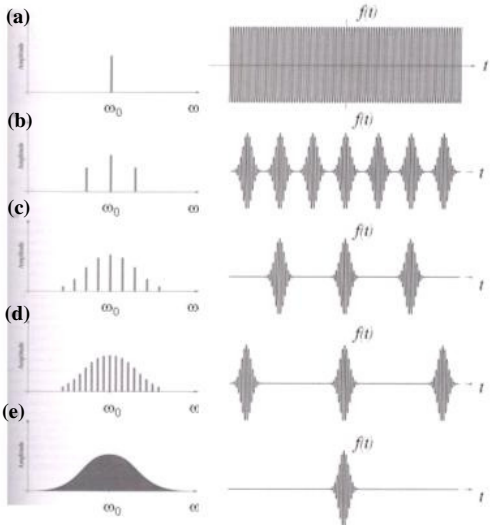

Fig. 2.2. 1st column shows the frequency spectra. The beats in time domain are displayed in the 2nd column.

Here, let us next consider that the pulse propagates inside the medium [12]. The harmonic components are added up in phase at the peak of the pulse. Define the phases of the waves $\phi = n(\omega)\omega z/c - \omega t$, where ω is the angular frequency of each wave, $n(\omega)$ is refractive index of the medium, c is speed of light in vacuum. Assuming that the pulse propagates without distortion, all harmonics are in-phase at the peak of the pulse. Note the propagation distance of z corresponds to the position where the pulse peak is present. As such, the harmonics are in-phase for all values of ω thereby ϕ being constant with respect to ω. It can be mathematically expressed as

$$\frac{dn}{d\omega}\frac{\omega z}{c} + \frac{n(\omega)z}{c} - t = 0 \text{ , i.e. } \frac{d\phi}{d\omega} = 0 \tag{2.1}$$

Using this equation, we express z in terms of time t. Defining the group velocity v_g, it leads to $z = v_g t$. Note that v_g tells where the peak of the pulse is located after time t. From Eq.(2.1), the group velocity is given by

$$v_g = \frac{c}{n_0 + \omega\frac{dn}{d\omega}} \tag{2.2}$$

where n_0 is the mean index of the material. We define the denominator $n_g = n_0 + \omega(dn/d\omega)$ as a group index. In a non-dispersive material system, i.e. $dn/d\omega = 0$, the group velocity corresponds to the phase velocity of a monochromatic wave. We are interested in the pulse propagation inside the dispersive media. The pulse propagates in normal dispersion medium $dn/d\omega > 0$ slower than c, i.e. $v_g < c$ or in

negative dispersion medium $dn/d\omega < 0$ greater than c, i.e. v_g>c. In next sections, we demonstrate pulse propagation in the dispersive medium.

B. Motivation for fast light in photorefractive crystal

In a so called fast-light medium, the dispersion is anomalous over a limited bandwidth. In such a medium, the group velocity for a pulse made up of frequency components within this bandwidth can be greater than the free space velocity of light. Scientists have been exploring a range of applications for such a medium [13]~[19]. These include enhancement of the sensitivity-bandwidth product of a LIGO-type gravitational wave detector, optical data buffering with a delay far exceeding the limit imposed by the delay-bandwidth product of a conventional cavity, a zero-area Sagnac ring laser gravitational wave detector with augmented strain sensitivity, and a super-sensitive ring laser gyroscope.

These applications are all based on so-called the White Light Cavity (WLC). A WLC is a cavity which resonates over a broader range of frequencies than ordinary empty cavities of equal length and finesse without a reduction in the cavity lifetime. As such, it can circumvent the tradeoff between the resonance bandwidth and the field build-up factor that ordinary cavities entail. A WLC also has the property that if the cavity length is moved away from the condition for empty cavity resonance, the frequency offset needed to restore the resonance is much larger than that for a conventional cavity, thus making it a more sensitive displacement and rotation sensor than an empty cavity can be.

A variety of approaches have been proposed and studied for realizing a white light cavity experimentally [20]~[22]. For example we have previously demonstrated one approach that uses a dispersive vapor medium within the cavity [15]. Specifically, the anomalous dispersion was produced by a rubidium vapor with bi-frequency pumped Raman gain. WLC operating at the wavelength of the Rb-transition, however, is not suitable for many of the applications listed above. For example, in order to apply the WLC concept for enhancing the bandwidth-sensitivity product of a LIGO-like gravitational wave detector, it is necessary to realize a WLC that operates at 1064 nm.

In this chapter, we show that the two wave mixing between pump and probe pulses in a photorefractive crystal creates a double gain profile similar to that of the bi-frequency pumped Raman gain in rubidium we have used previously, with the corresponding anomalous dispersion. We demonstrate superluminal propagation of pulses in such a medium. The anomalous dispersion produced in this way can also be employed to realize a WLC. The experiment reported here used a green laser at 532 nm, with a photorefractive crystal that has a relative slow (~seconds) response time. However, the technique demonstrated here is generic enough so that it can be employed with other photorefractive crystals as well. For example, a crystal of SPS [5], [23] is sensitive at 1064 nm, and has a much faster (~msec) response time. An extension of this technique to the SPS crystal at 1064nm could thus be used to make a WLC for enhancing the sensitivity-bandwidth product of a LIGO-type gravitational wave detector as mentioned above.

C. Gain doublet in photorefractive crystal

The gain doublet and corresponding anomalous dispersion are the product of non-degenerate two-wave mixing and angular multiplexing in a photorefractive crystal. Here, we summarize briefly the physical model used to study this process. A space charge field is generated by the interference of two strong pump beams with a weak probe, so that the refraction index is modulated by the electro-optic effect. The probe is coupled with the pump beams due to these refractive index gratings [24]. Assuming that the intensity of each pump is much higher than that of the probe, in undepleted pumps approximation the phase and intensity coupling coefficients can be written as functions of the angular frequencies of the pumps and the probe [25]:

$$\Gamma_{in} = \sum_{j=1,2} \frac{\Gamma_{0j}}{2} \left[\frac{d}{1+(\omega_s - \omega_{Pj})^2 \tau_j^{\,2}} \right] \tag{2.3a}$$

$$\Gamma_{ph} = \sum_{j=1,2} \frac{\Gamma_{0j}}{2} \left[\frac{d(\omega_s - \omega_{Pj})\tau_j}{1+(\omega_s - \omega_{Pj})^2 \tau_j^{\,2}} \right] \tag{2.3b}$$

where Γ_{in} and Γ_{ph} are the intensity and phase coupling coefficients respectively. Γ_{0j} depends on the incident angle between the jth pump and the probe [26]. τ_j is the rise time of the space charge field induced by the pumps, and d is the effective interaction length. ω_s and ω_{pj} are the angular frequencies of the probe and the j^{th} pump respectively. The intensity gain and the phase shift of the probe are determined by these coefficients. For our experiment, the 1st and 2nd pump beams are up-shifted and down-shifted respectively by $\Delta\omega$ from the source frequency of ω_0, so that $\omega_{p1}=\omega_0+\Delta\omega$, $\omega_{p2}=\omega_0-\Delta\omega$. This creates

two gain lines separated by $2\Delta\omega$, and a region of anomalous dispersion occurs between them. The probe is pulsed, with a Gaussian spectrum centered around ω_0. The group velocity of the Gaussian pulse can be expressed as $v_g = c/(n_0 + c \times \partial\Gamma_{ph}/\partial\omega)$ [12]. If the carrier frequency of the probe pulse is placed in the middle of the anomalous dispersion region and the pulse bandwidth is smaller than the negative dispersion bandwidth, the group velocity in the photorefractive medium can become larger than *c*, or may even become negative. It is instructive to view these parameters graphically. We consider the probe pulse to be of the form $\exp(-t^2/t_0^2)$. We choose the pump intensities to be equal so that $\Gamma_{01} = \Gamma_{02} \equiv \Gamma_0$ and $\tau_1 = \tau_2 \equiv \tau_M$. For illustration, we consider $\Gamma_0 d = 6$, $\tau_M = 1.1\text{sec}$, and $t_0 = 0.6\text{sec}$. Fig. 2.3(a) shows the normalized intensity and phase coupling coefficients (Γ_{in}, Γ_{ph}), and the Fourier Transform (S) of the probe as functions of $\omega_s - \omega_0$, for $\Delta\omega = 0$. Here the two gains overlap exactly and behave like a single gain line. The dispersion around the probe carrier frequency in this case is normal, and the v_g of the probe becomes smaller than *c*. The width of the gain here is close to τ_M^{-1}. In Figs. 2.3(b)~(d), we plot the same parameters for increasing separation between the pump frequencies. For $\Delta\omega = 1\text{Hz}$ (Fig. 2.3(c)), the separation is comparable to the gain width, so that two gain peaks are clearly distinguishable. This leads to negative dispersion between the peaks, as shown. In Fig. 2.3(d), the separation becomes sufficiently wide so that that negative dispersion region covers the whole bandwidth of the Gaussian spectrum of the pulse.

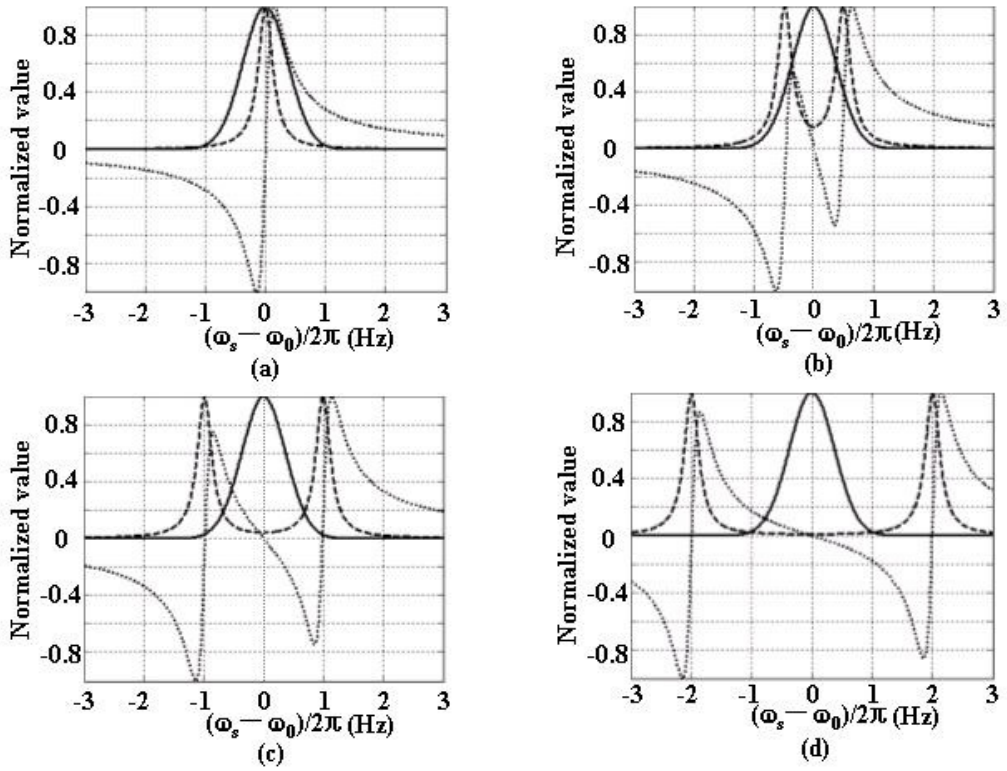

Fig. 2.3. Numerical, normalized plots of S(ω), the Fourier transform of the input pulse (solid line), Γ_{in}(dashed line), and Γ_{ph} (dotted line). The input pulse is assumed to be of the form $\exp(-t^2/t_0^2)$. For these plots, we have used for t_0=0.6sec, $\Gamma_0 d = 6$ and $\tau_1 = \tau_2 \equiv \tau_M = 1.1\text{sec}$. The four sets are for four different gain separations, $2\Delta\omega$ (a) 0Hz, (b) 1Hz, (c) 2Hz, (d) 4Hz.

D. Pulse propagation in gain doublet system

For the case of the Gaussian input pulse of the form $\exp(-t^2/t_0^2)$, the output pulse coupled in the frequency domain can be expressed as [5], [23] :

$$S(d,\omega_s) = S(0,\omega_s)\exp(\Gamma_{in1} + \Gamma_{in2})\exp[i(\Gamma_{ph1} + \Gamma_{ph2})] \qquad (2.4)$$

Here d is the propagation distance of the probe inside a photorefractive crystal. $S(0, \omega_s)$ is the Fourier transform of the input pulse at the entrance of the material. Hence, one can obtain the total output signal intensity in the time domain by squaring the inverse Fourier transform of $S(d, \omega_s)$. Figs. 2.4(a)~(d) show the numerical simulation of the normalized output signal intensity for different gain line separations corresponding to each case in Figs. 2.3(a)~(d). In Figs. 2.4(a) the output is clearly delayed compared to the pulse propagating in free space, as expected. Fig. 2.4(b) shows the resultant output from propagation under the two gain peaks configuration associated with Fig. 2.3(b). To understand the behavior of the probe in this case, note brief that the gain in Fig. 2.3(b) is peaked at $\omega_0 \pm \Delta\omega$ with a deep valley in the middle. As such, the components of the probe spectrum at $\omega_0 \pm \Delta\omega$ get amplified disproportionately, leading to a two peaked spectrum. This leads to the beat note at 1Hz in Fig. 2.2(b). Furthermore, each of these peaks experiences normal dispersion, which leads to slowing of the probe, also evident in Fig. 2.3(b). In the case of Fig. 2.3(c), the gain separation is large enough so that the spectrum of the probe is almost completely within the region where the dispersion is anomalous (i.e. negative). This leads to advancement of the probe pulse, as can be seen in Fig. 2.3(c). The advance in this case is rather small due to the moderate steepness in the anomalous dispersion, and is evident only near the peak. Note also that a residual beat note is present at 2Hz, as expected. As the gain separation increases further (Fig. 2.3(d)), the slope of the anomalous dispersion become smaller, thus reducing the pulse advancement, as seen in Fig. 2.4(d). It is evident from Figs. 2.3(c), (d) that

$\partial^2\Gamma_{ph}/\partial\omega^2 \neq 0$ for $\omega \neq \omega_s$. The resulting group velocity dispersion [27], [28] causes pulse compression in this case , as can be seen clearly in Figs. 2.4(c) ,(d).

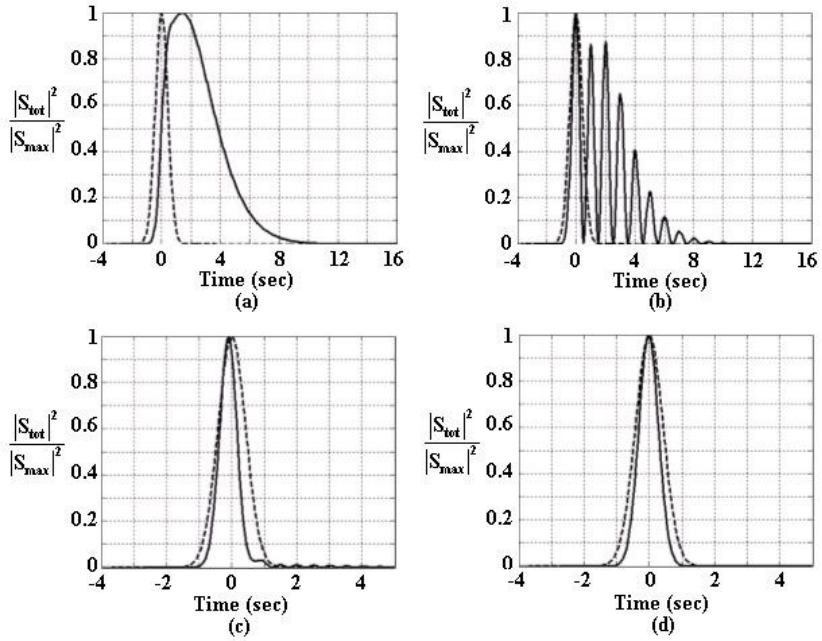

Fig. 2.4. Simulated output signal for the Gaussian input of $\exp(-t^2/t_0^2)$ for the same parameters as set in Fig. 2.1. The frequency difference between the gains is given as (a) 0Hz, (b) 1Hz, (c) 2Hz, and (d) 4Hz. Dashed line indicates reference, solid line indicates signal output.

E. Experimental set-up and results

We carried out an experiment that corresponds closely to the simulations. The experimental set-up is illustrated schematically in Fig. 2.5. A collimated 532nm doubled Nd-YAG laser was split into a probe and two pump beams. The acousto-optic modulator s (AOMs) were driven by frequency synthesizers (PTS's). The IQ modulator (JCIQ-176M, Minicircuit) and the AOM generated the Gaussian probe pulse with a carrier

frequency of f_L+110MHz+4Hz corresponding to $\omega_0/2\pi$, where f_L is the laser frequency. The Gaussian pulse with a temporal width of t_0=0.6sec was generated by a DAQ-Card (DAQCard−6036E, National instrument) with a repetition period of 20sec for $\Delta\omega/2\pi$=0 and 0.5Hz and, 10sec for $\Delta\omega/2\pi$=1 and 2Hz. The first and second pumps (P1 and P2) were shifted by $\pm\Delta\omega/2\pi$ from f_L+110MHz+4Hz, respectively, thereby producing two gain peaks with a separation of $2\Delta\omega/2\pi$. The incident angle of the probe is approximately 90° from the C-axis of the Ce:$BaTiO_3$ crystal used for this experiment. P1 and P2 were angular multiplexed at angles of 40° and 60° with respect to the probe. The probe was coupled to the two pumps over an interaction length of 0.5cm inside the crystal. The polarization direction of all the beams and the C-axis were parallel to the optical table. A part of the probe was split-off to provide a reference pulse. This probe was monitored simultaneously with the pulse that traveled through the crystal, and was used to determine the degree of pulse delay/advancement and compression.

Figs. 2.6(a)~(d) show the normalized reference and output signals as $\Delta\omega$ increases. For $\Delta\omega$=0 in Fig. 2.6(a), the two gains coincide to form a single gain which results in the time delay (1.3sec) of the Gaussian input pulse. As $\Delta\omega/2\pi$ increases to 0.5Hz, parts of the probe spectrum shifted from ω_0 by ±0.5Hz (the maximum gain and slowing region) become the primary frequency components which are amplified and delayed, thereby resulting in the beat frequency of 1Hz, corresponding to $2\Delta\omega/2\pi$, as shown in Fig. 2.6(b). In Fig. 2.6(c), since the gain doublet is sufficiently separated so that the spectrum of the probe exists entirely within the anomalous dispersion region, the

output is advanced by 0.28sec compared to the reference. As $\Delta\omega/2\pi$ increases up to 2Hz, the anomalous dispersion becomes very small. Hence, it is observed that the output has virtually no advancement, as can be seen in Fig. 2.6(d)

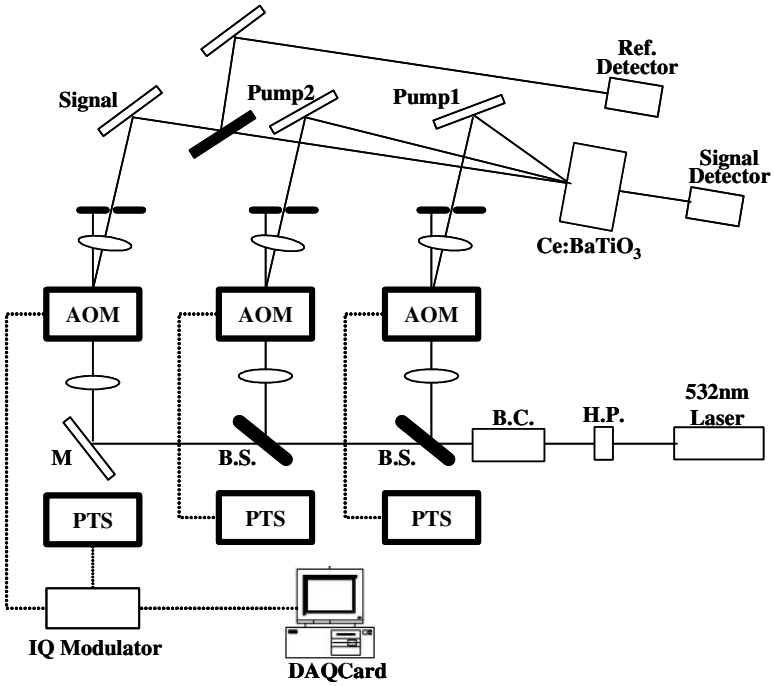

Fig. 2.5. Schematic diagram of the experimental set-up; AOM : Acousto-optic modulator, B.S : Beam Splitter, B.C : Beam Collimator, H.P: Half waveplate, M: Mirror, PTS : Frequency synthesizer, Pump1: f_L+110MHz+4Hz+$\Delta\omega$, Pump2: f_L+110MHz+4Hz−$\Delta\omega$, probe : Gaussian pulse with the carrier frequency of f_L+110MHz+4Hz.

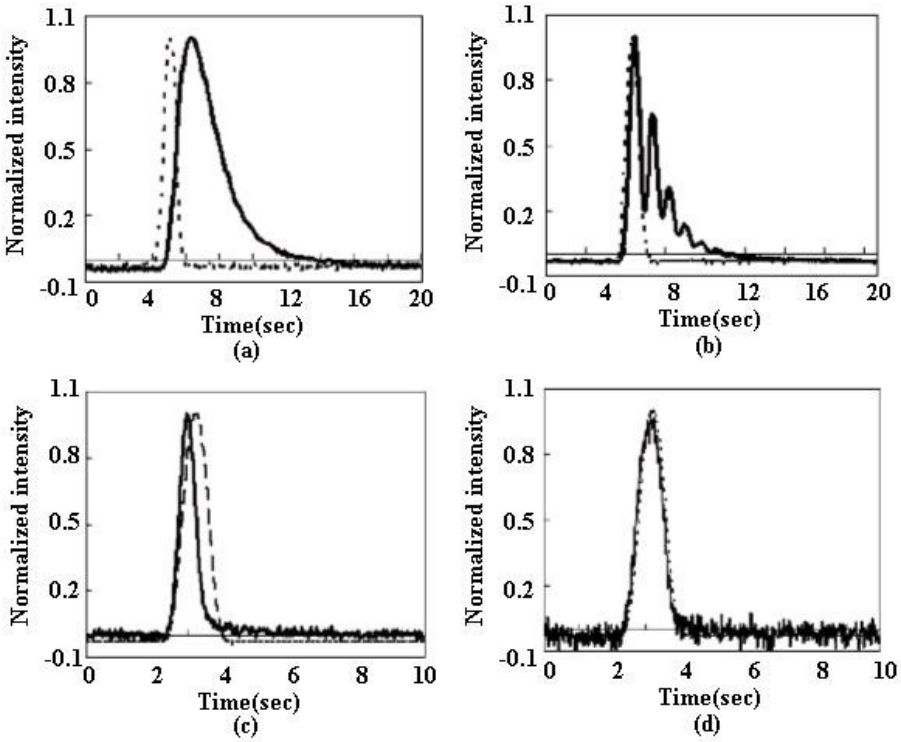

Fig. 2.6. Experimental results showing the group velocity variation of the signal output with setting the separation of the gain doublet to (a) 0Hz, (b) 1Hz, (c) 2Hz, and (d) 4Hz. Dashed line indicates reference, solid line indicates signal output

CHAPTER III

FAST LIGHT MEDIUM IN LASER CAVITY AND ITS APPLICATION

A. Motivation for superluminal lasers

Ring Laser Gyroscopes (RLGs) have been used in inertial navigation systems since the 1970s for everything from aerospace and military guidance systems to oil prospecting [29]. The basic principle is simple: the length of an optical cavity is perturbed under rotation by the Sagnac effect [30], so that the resonant frequency of the light with the cavity changes. The degree of this shift depends, as has been shown [16], [17] on the dispersion of the medium inside the cavity. In previous White Light Cavity (WLC) demonstration, it was realized by placing a fast-light medium inside a conventional cavity [15]. The WLC exhibit high sensitivity to mirror displacement and rotation [13]. However, the concomitant broadening of the linewidth, by essentially the same factor, means that there is virtually no net improvement in the smallest measurable displacement or rotation. We have shown that this constraint is eliminated if an active cavity is used, where the rotation (or any non-reciprocal change in the cavity length) is measured by monitoring the beat note between the counter-propagating lasing modes [13].

In this chapter, we develop the theoretical model for WLC behavior of such an active resonator: a superluminal ring laser. Since the laser operates under the condition where the gain per pass balances the loss per pass, the conventional model for WLC does not apply. However, we show that if the gain profile is flat over the region of

interest, with a dip in the middle, the lasing mode centered at the dip behaves like WLC, with its frequency becoming highly sensitive to mirror displacement or rotation. The enhancement factor can be as high as 10^7, comparable to what is achievable in a passive cavity. We also present a physical interpretation of this behavior in terms of an effective Kramers-Kroenig relation, and show that the process works with both homogeneously or inhomogeneously broadened gain media.

B. Signal from laser cavity, and homogenous and inhomogeneous gain medium in laser cavity

First, we consider the light in a laser cavity. The cavity contains a dispersive medium. Its resonant frequency can be described by [31]:

$$\nu + \dot{\phi} = \Omega - \frac{1}{2}\nu\chi'(E,\nu) \tag{3.1}$$

where χ' is a real part of the susceptibility, ϕ is a round-trip phase shift, ν is the resonant frequency of the medium-filled cavity, and Ω is that of the cavity in the absence of the medium so-called an empty cavity. The resonant frequency Ω is equal to $2m\pi c/L$. The parameter m is an integer and c is the speed of light in free space. The cavity length is represented by L. Note χ' is itself frequency and intensity dependent. The resonant frequencies Ω and ν are both initially equal to ν_0 when the cavity length is L_0. Let us assume that the gain (or absorption) profile of the medium in the cavity is symmetric about ν_0. For the sake of comparison, we define the normalized parameters, $\Delta = (\Omega - \nu_0)/\Gamma$ and $\delta = (\nu - \nu_0)/\Gamma$ where Γ is the linewidth of the absorption or gain line

in radian. The derivatives $d\Delta/dL$ and $d\delta/dL$ represent the resonant frequency shifts induced by the perturbation of L associated with the empty cavity and the medium-filled cavity, respectively. We consider the ratio, $R = [d\delta/dL]/[d\Delta/dL]$ to determine if the amount of the frequency shift is enhanced (R>1) or diminished (R<1) by the dispersive intracavity medium. In steady state ($\dot{\phi} = 0$) , dividing Eq.(3.1) by Γ, applying $\nu/\Gamma = \delta + \nu_0/\Gamma$, and differentiating with respect to L, it leads us to

$$\frac{d\delta}{dL} + \frac{1}{2}\frac{d\chi'}{dL}\frac{\nu}{\Gamma} + \frac{1}{2}\chi'\left(\frac{d\delta}{dL}\right) = \frac{d}{dL}\left(\frac{\Omega - \nu_0}{\Gamma}\right) \tag{3.2}$$

By substituting $(d\chi'/d\delta)(d\delta/dL)$ for $d\chi'/dL$, the ratio R can be expressed as

$$R = \frac{1}{1 + \frac{1}{2}\chi' + \frac{1}{2}\frac{d\chi'}{d\delta}\frac{\nu}{\Gamma}} \tag{3.3}$$

We apply $d\delta = 1/\Gamma d\nu$ and $n_0 = \sqrt{1+\chi'} \approx 1 + \chi'/2$, where n_0 is the mean index of the medium. One can easily prove that the denominator in Eq.(3.3) is the group index, $n_g = 1 + \chi'/2 + (\nu/2)(d\chi'/d\nu)$ of the dispersive intracavity medium. For normal dispersion (n_g>1) in the laser cavity, R(=n_g) becomes less than one. The resonant frequency shift with respect to the length variation dL decreases compared to the shift in the empty cavity. For n_g<1, i.e. in the cavity filled with anomalous dispersion medium, the frequency shift is amplified to be equal to $1/n_g$ times the amount of the shift in the empty cavity. Eq.(3.3) can be applied to any intracavity medium. As such, if one can calculate the dispersion $d\chi'/d\nu$ for any kind of a given medium, then the resonant frequency shift of the medium-filled cavity can be predicted by comparing it to that of

the empty cavity. ν_0 and Γ are properties of the medium and thereby independent of the length change dL. Eq.(3.3) can be modified as $(d\nu/dL)/(d\Omega/dL) = 1/n_g$. Recent study [13] showed $\Delta\nu=\Delta\nu_{ec}/n_g$ where $\Delta\nu$ is the resonant frequency shift for a passive cavity and $\Delta\nu_{ec}$ is for an empty cavity. Now, note that the modified equation associated with the laser (active) cavity is consistent with the previous results. To interpret this result for the case of the active cavity, however, we must further take into account the fact that the gain medium can be saturated.

Indeed, the field inside a laser cavity increases until it saturates the gain medium such that the resulting gain exactly balances the loss within the cavity. This is the steady-state lasing condition. Field amplitude and phase in the laser cavity are described by a set of self consistency equations [31]. As such, the steady-steady gain condition can be expressed as:

$$\dot{E} = -\frac{1}{2}\frac{\nu}{Q}E - \frac{1}{2}\nu E\chi''(E,\nu) = 0, \quad \dot{E} = 0 \tag{3.4}$$

where E is the laser field amplitude and χ'' is an imaginary part of the susceptibility. Q represents the internal loss characteristic of the cavity. It leads us to

$$\chi''(E,\nu) = -\frac{1}{Q} \text{ (for } E,\nu \neq 0) \tag{3.5}$$

χ'' implies the gain (or loss) characteristics and χ' in Eq. (3.1) is relevant to refractive index. Note that χ'' and χ' depend on E as well as its frequency ν.

To understand the relationship between the gain saturation and the self-consistency equations, let us consider homogeneously broadened gain medium. Fig. 3.1

illustrates the saturated gain corresponding to the cavity loss at steady state. We assume that a lasing mode frequency ν exists within the gain profile but is apart from the gain center. The saturated gain G(ν) and the non-saturated gain $G_0(\nu)$ are expressed as $G \sim \Delta N g(\nu)$ and $G_0 \sim \Delta N_0 g(\nu)$, respectively, where ΔN is the population inversion in the presence of the lasing field, ΔN_0 is the population difference without field and g(ν) is a normalized Lorentzian lineshape function [32]. Note that G and G_0 have the same

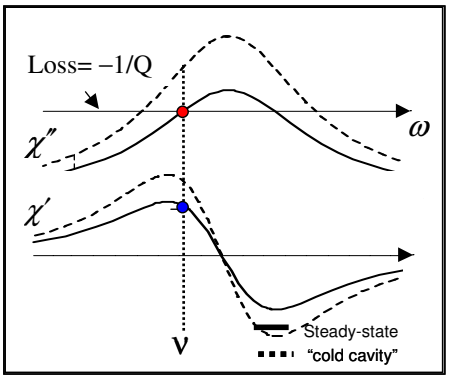

Fig. 3.1. Saturation of homogeneous gain profile to satisfy self-consistency equations at lasing frequency. Cold cavity represents a cavity before the gain reaches steady state. When the laser cavity reaches steady state, the lasing beam experiences gain and index, represented by red and blue points, respectively.

lineshape function. As such, the shape of profiles remains unchanged. The saturation effect by the lasing field depletes the population of the excited state, i.e. the reduction of ΔN. The magnitude of the homogeneous gain profile decreases but only until the gain at the frequency of the lasing field becomes equal to the loss in the cavity. The question then becomes, what effect does this gain saturation have on the dispersion associated with the gain profile? One might at first think that the equivalence of the steady-state

gain at every lasing frequency would mean that there could be no variation in the steady-state index of refraction as a function of frequency. This is not the case, however. In a homogenously broadened medium, the saturation effect is simply to decrease the magnitude of χ' over the whole profile [32], [33]. Note that the frequencies for which χ' is plotted here are not in general resonant in the cavity and cannot be sustained in steady state. Only the single point at $\omega=\nu$, the lasing frequency, provides us information about the phase shift that would be seen by a resonating beam. However, if we draw this graph for a range of different choices of ν corresponding to different choices of cavity length, we will see that each choice determines a different index value at steady state. Thus, the index does indeed depend on lasing frequency. This variation is the primary reason that the resonant frequency of a laser cavity differs from that of a passive cavity of equal length, usually being closer to the center of the gain line. This phenomenon is called mode-pulling.

Next, consider an inhomogeneously broadened gain medium. In such medium, we may regard such inhomogeneous gain profile as the sum of many narrower, homogeneously broadened gain profiles individually centered at a different frequency. The saturation does not reduce the gain over the whole profile, but at a localized frequency range around the lasing frequency. As such, the gain saturation occurs at the frequencies supported by the lasing mode. The lasing beam, the so-called hole burning laser, bleaches a narrow band "hole" into the inhomogeneously broadened gain. This result is referred to as spectral hole burning [32], [33]. Next, let us imagine that a gain profile contains four spectral holes separated approximately by the free spectral range

(FSR) of the cavity. We assume that the inhomogeneous gain bandwidth is sufficiently broad so that it can sustain 4 cavity modes. The net gain can then be modeled as sum of a broad Lorentzian (or more accurately, a Voigt profile) and four narrow, inverted Lorentzians. The associated χ'at any frequency is then determined by the sum of the phase shift due to such a broad Lorentzian gain and that due to each of the narrow Lorentzian "absorption" features, as illustrated in Fig. 3.2 [34]~[37].

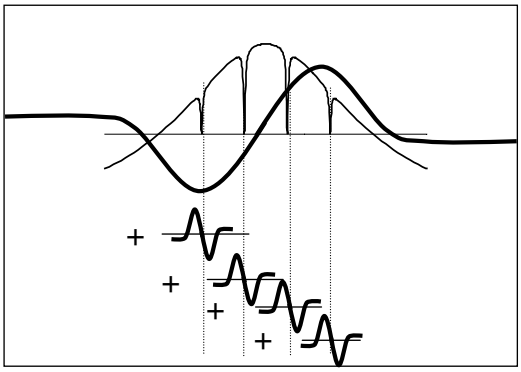

Fig. 3.2. Saturation of inhomogeneous gain profile (thin line) to satisfy self-consistency equations at lasing frequency or frequencies, and index profiles (large thick line and four small thick lines) corresponding to the saturated gain profile.

The phase associated with a hole is zero at the center of that hole, but the contributions to the phase from holes burned at other frequencies may cause the phase to be different from that which would be associated with the gain alone. At any given frequency, in other words, the phase depends on the shape of the entire profile. Let us assume that the inhomogeneous gain supports a single lasing mode. As such, there is only one spectral hole. The dispersion at the lasing frequency will be unaffected by the saturation. As a result, the lasing beam experiences the single phase associated with the inhomogeneous

gain. Again, the index of refraction depends on lasing frequency. This brief review is intended to elucidate the distinction between the dispersion of a medium in free space, and the dependence on frequency of the steady-state refraction index in a laser cavity. Though related, they are not the same. The group index which we refer to here is related to the velocity of groups composed entirely of lasing frequencies. Superluminal pulses of this type have in fact been observed [38] in inhomogenously broadened media.

C. Absorption dip embedded in flat broad gain

We have established that the resonant frequency shift is induced by the change of the laser cavity length. It is inversely proportional to the group index of the material. Furthermore, we have shown that the dispersion inside a laser in steady state is not zero, though it does depend on the saturating field. We now ask how to achieve the dispersion profile we desire. Anomalous dispersion is required to maximize the dependence of lasing frequency on cavity length. The Kramers-Kronig relations [32] tell us that anomalous dispersion is usually associated with an absorption feature, or equivalently, a reduction in gain. In this section, let us consider the case in which the cavity contains a medium with a narrow absorption as well as a medium with a saturable and infinitely broad gain. This configuration creates the absorption dip in the broad gain, resulting in anomalous dispersion within the absorption bandwidth. We then express the net susceptibility of the media as a sum [39]:

$$\chi' = -\frac{N_i \hbar \Omega_{ri}}{\varepsilon_0 E^2}\left(\frac{2\Omega_{ri}(\nu-\nu_0)}{2\Omega_{ri}^2+\Gamma_i^2+4(\nu-\nu_0)^2}\right) \tag{3.6a}$$

$$\chi'' = -\frac{N_e \hbar \Omega_{re}}{\varepsilon_0 E^2}\left(\frac{\Omega_{re}\Gamma_e}{2\Omega_{re}^2 + \Gamma_e^2}\right) + \frac{N_i \hbar \Omega_{ri}}{\varepsilon_0 E^2}\left(\frac{\Omega_{ri}\Gamma_i}{2\Omega_{ri}^2 + \Gamma_i^2 + 4(\nu - \nu_0)^2}\right) \qquad (3.6b)$$

Here ε_0 is the permittivity of free space, E is the field amplitude, and $\hbar$ is plank's constant. N_e and N_i represent the number of atoms per unit volume for the broadband gain medium and for the inserted narrow absorptive medium, respectively. We use the subscript "e" for the "envelope" gain profile and "i" for the narrower absorption profile, in order to remember that the absorption is "inside" the envelope of the gain. We assume $\Gamma_e >> \Gamma_i$. The gain and the absorption linewidth are denoted by Γ_e and Γ_i, respectively. Note that Γ_i corresponds to Γ in Eq.(3.3). The center frequency of the absorption line is represented by ν_0. The field with Rabi frequency Ω_{re} couples with the background gain medium. The absorption medium is driven by the field with Rabi frequency Ω_{ri}. Ω_{ri} and Ω_{re} are equal to $\wp_i E/\hbar$ and $\wp_e E/\hbar$, respectively, where $\wp_i$ and $\wp_e$ are the dipole moments associated with the media. We now define ξ_i and ξ_e such that $\Omega_{ri}^2 = \Gamma_i^2 E^2 \xi_i$ and $\Omega_{re}^2 = \Gamma_e^2 E^2 \xi_e$.

The field intensity inside the medium is given by $I_{e,i} = E^2/2\eta_{e,i}$ where $\eta_{e,i}$ is impedance. $I_{e,i}$ can be rewritten as $I_{e,i} = \Omega_{re,ri}^2 \hbar^2/2\eta_{e,i}\wp_{e,i}^2$ by using the Rabi frequencies $\left(\Omega_{ri,re} = \wp_{i,e} E/\hbar\right)$. According to $\Omega_{re,ri}^2 = \Gamma_{e,i}^2$ for the saturation, the saturation intensity is given by $I_{sat\_e,sat\_i} = \Gamma_{e,i}^2 \hbar^2/2\eta_{e,i}\wp_{e,i}^2$. As such, the ratio of $I_{e,i}/I_{sat\_e,sat\_i}$ can be written as $\Omega_{re,ri}^2/\Gamma_{e,i}^2$. Also, from $I_{e,i} = E^2/2\eta_{e,i}$, we can derive $I_{e,i}/I_{sat\_e,sat\_i} = E^2/2\eta_{e,i}I_{sat\_e,sat\_i}$. Using $I_{e,i}/I_{sat\_e,sat\_i} = \Omega_{re,ri}^2/\Gamma_{e,i}^2 = E^2/2\eta_{e,i}I_{sat\_e,sat\_i}$ and substituting $\Gamma_{e,i}^2 E^2 \xi_{e,i}$ for $\Omega_{re,ri}^2$,

one finds $\xi_{e,i} = 1/2\eta_{e,i}I_{sat\_e,sat\_i}$. To understand physical characteristics of $\xi_{e,i}$, note that according to $I_{sat\_e,sat\_i} = \Gamma_{e,i}^2\hbar^2/2\eta_{e,i}\wp_{e,i}^2$, the product $\eta_{e,i}I_{sat\_e,sat\_i}$ consists of the medium-dependant parameters such as absorption bandwidth and dipole moments in the absence of the lasing frequency-dependent parameters. Therefore, one recognizes that $\xi_{e,i}$ $(=1/2\eta_{e,i}I_{sat\_e,sat\_i})$ is independent of the lasing frequency. For the sake of simplicity, we introduce $G = N_e\hbar\xi_e\Gamma_e/\varepsilon_0$, $H = N_i\hbar\xi_i\Gamma_i/\varepsilon_0$, $\delta = (\nu - \nu_0)/\Gamma_i$ and $B = 2E^2$. Eq.(3.6) is modified as

$$\chi' = \frac{-2\delta H}{B\xi_i + 1 + 4\delta^2} \tag{3.7a}$$

$$\chi'' = -G\left(\frac{1}{B\xi_e + 1}\right) + H\left(\frac{1}{B\xi_i + 1 + 4\delta^2}\right) \tag{3.7b}$$

We are now in a position to evaluate the ratio R defined in Eq.(3.3). Before differentiating χ' with respect to δ, we should note that the steady-state field intensity inside the cavity is the frequency dependent function, i.e. $B(\delta)$, so that the derivative of χ' in Eq.(3.7a) can be expressed as $d\chi'/d\delta = \partial\chi'/\partial\delta + (\partial\chi'/\partial B)(dB/d\delta)$. The partial derivatives $\partial\chi'/\partial\delta$ and $\partial\chi'/\partial B$ are assessed by differentiating Eq.(3.7a) with respect to δ and B, respectively. To calculate $dB/d\delta$, we must find B as a function of δ. Let us recall the field amplitude equation in the laser cavity. In a steady state, it gives $\chi'' = -1/Q$. Inserting $-1/Q$ into χ'' of Eq.(3.7b) and modifying it, we find a quadratic equation for B,

$$\xi_e\xi_i B^2 + [\xi_i + \xi_e(1 + 4\delta^2) - QG\xi_i + QH\xi_e]B + 1 + 4\delta^2 - QG(1 + 4\delta^2) + QH = 0 \tag{3.8}$$

Keeping in mind that the intensity is always a positive number, we choose the solution for B that is positive over the lasing bandwidth. In Fig. 3.3, we can now plot the real part of the steady-state susceptibility as a function of frequency. For illustration, we consider $Q=3\times10^7$, Γ_i=10MHz and λ_0=780nm, with H=5, G=10 and $\xi_i/\xi_e = 1.1333333938$ ($\lambda_0=2\pi c/\nu_0$ where c is speed of light in vacuum)

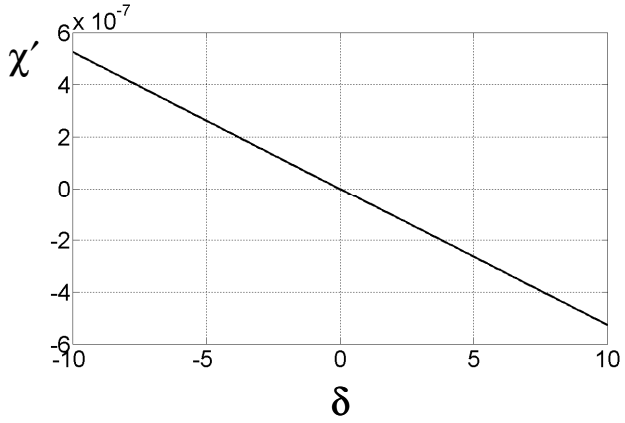

Fig. 3.3. Real part of the steady-state susceptibility as a function of lasing frequency.

The remaining procedure to calculate $R = [d\delta/dL]/[d\Delta/dL]$ is to express χ' and $d\chi'/d\delta$ in terms of δ. We found $\partial\chi'/\partial\delta$ and $\partial\chi'/\partial B$ from Eq.(3.7). $dB/d\delta$ is obtained by differentiating B(δ) of Eq.(3.8) with respect to δ. By inserting $\partial\chi'/\partial\delta, \partial\chi'/\partial B$ and $dB/d\delta$ into $\partial\chi'/\partial\delta + (\partial\chi'/\partial B)(dB/d\delta)$, it leads us to $d\chi'/d\delta$. Substituting B(δ) into Eq.(3.7a), one can find χ' as function δ as well. Inserting $\chi'(\delta)$ and $d\chi'/d\delta$ into Eq.(3.3), we obtain the ratio R for the narrow absorption medium in the environment of the infinite broadband gain as a function of δ. This R is a measure of the degree to which the sensitivity of a laser cavity with these dispersive media is enhanced over that of an

empty cavity. We note, however, that the equation for R is frequency dependent. This essentially tells us that once the lasing frequencies are outside the anomalous dispersion regime, there is no enhancement of their sensitivity to changes in length. We find, with the numbers above, that the profile of R gives a peak value of 11×10^6 and reduces to zero as the frequency deviates from the dispersion regime.

We find, furthermore, that the peak value of R, i.e. R_p varies with the ratio ξ_i/ξ_e . Fig. 3.4 displays the normalized R_{p_nor} by its maximum value for each case of the different H. For illustration, we use the same parameters as in Fig. 3.3. We consider more H's corresponding to the absorption dip. R_{p_nor} changes very rapidly with ξ_i/ξ_e . Note that ξ_i/ξ_e corresponds to $\Gamma_i^2\wp_e^2/\Gamma_e^2\wp_i^2$. Therefore, in order to significantly enhance the frequency shift compared to the empty cavity, one must carefully choose the media whose $\wp_e^2/\wp_i^2$ can yield the appropriate ξ_i/ξ_e for maximum R_p. Fig. 3.4 suggests that the optimal values of ξ_i/ξ_e for maximum of R_p varies with the depth of the absorption dip.

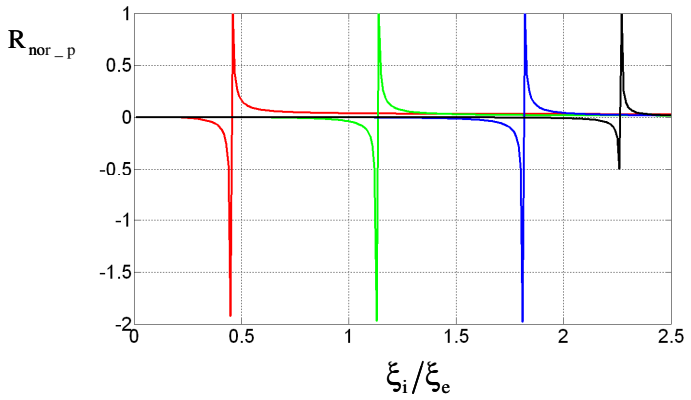

Fig. 3.4. Maxima of the ratio for different absorption depth. (red: H=2, green: H=5, blue: H=8, black: H=10) as the function of ξ_i/ξ_e . Each graph is normalized by its maximum value.

The variation of the absorption also has the effect of shifting the frequency of the maximum sensitivity as well as altering the bandwidth of that sensitivity. Fig. 3.5 displays R for different absorption dip. For illustration, we adjust ξ_i/ξ_e for different H's such that maximum R's for H=2, 5, 8, and 10 become equal to 1.1×10^7. The graph indicates that the peak of R is shifted from δ=0, and the bandwidth of R broadens as H increases from 2 to 10. We have carried out similar simulations for a wide variety of gain and absorption media, varying the bandwidth and depth of the gain and the "hole" in the gain, for homogeneously and inhomogeneously broadened media. The results in all cases support those we have seen in this presented example.

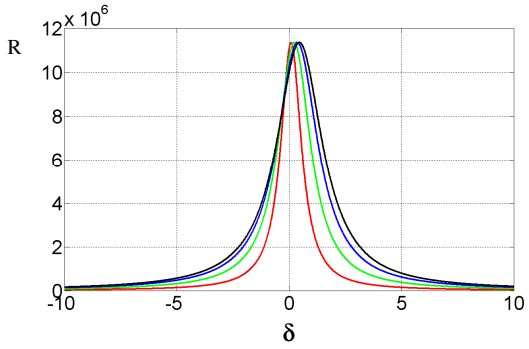

Fig. 3.5. R as a function of δ. ξ_i/ξ_e is equal to 0.4533333530 for H=2 (red), 1.1333333938 for H=5 (green), 1.8133334374 for H=8 (blue), and 2.2666668013 for H=10 (black).

D. Brief discussion about noise

These results imply that we may achieve the same sensitivity in lasers, whether based on homogeneously or inhomogeneously broadened gain media, which we have seen in passive cavities. Of course, an increased sensitivity is worthless if the noise is

also increased. We will not go into detail here about the effects of the fast-light medium on laser frequency noise. These details can be found in Ref. 40. However, we do wish to make one important point. The primary source of frequency noise for most lasers is mirror jitter, and we might expect that the fast-light medium would increase the sensitivity of lasers to such jitter, thus increasing the noise by the same factor as the sensitivity. However, laser gyroscopes do not involve direct frequency measurements, but rather measurements of the beat note between counter propagating modes, as illustrated in Ref. 29. Mirror jitter, thermal effects, and other macroscopic noise sources affect both beams, and this common-mode noise cancels out when one measures the beat frequency. The only noise on such a measurement is quantum noise, and Ref. 40 shows that this is unaffected by the fast-light material. Ultimately, the details of real, physical systems will determine how well the approach works for gyroscope applications. These theoretical results, however, are sufficiently promising to justify significant further experimental investigation.

CHAPTER IV

APPLICATION OF FAST LIGHT INTRACAVITY MEDIUM TO DATA BUFFER SYSTEM

A. Motivation for data buffer via white light cavity

Because of its significance in its application to optical buffers and optical memories, different methods for controlling the group index (n_g) were investiaged. It was controlled through manipulation of atomic resonances [1], [3]; light interactions in non-linear materials such as stimulated Brillouin scattering (SBS) in optical fibers [6]~[9]; or two-wave mixing in photorefractive crystal [5], [41]. So far, in a slow-light demonstration (n_g>1), a light pulse was delayed by less than or several times the pulse duration [1], [3], [5], [6], [8], [9]. SBS generated by pulsed Brillouin pump in fibers [42] was used to store an optical pulse, with the constraint that the storage time should be less than the acoustic lifetime of nanoseconds in optical fibers. In stored-light based on electromagnetically induced transparency (EIT), a photon wave packet is transferred to atomic coherence in collective atomic system so that the storage time corresponds to the coherence time of hyperfine transitions [43]. In low temperature environment, 20μs pulse was recorded as the coherence of the ground hyperfine states in $Pr:Y_2SiO_5$ for the time scale of several seconds [44].

A material that is anomalously dispersive over a limited frequency range is known as a fast-light medium because it can support group velocities greater than the speed of light in free space. An optical cavity, which contains such a fast-light medium

and has a broadened linewidth without a reduction of the cavity buildup, is called White Light Cavity (WLC) [15]. The WLC has been realized by filling a cavity with rubidium vapor where Raman gain lines were produced around the cavity resonance to achieve the fast-light condition ($n_g<1$). The pump intensity and the gain separation were controlled to adjust a negative dispersion slope so that the linewidth of the WLC was tunable. In the absence of the pumps, the WLC was converted to an ordinary cavity.

Utilizing such features of the WLC, we propose the details of a data pulse delay system in the next section. Due to the tunable bandwidth of the WLC, a data pulse is successfully delayed for sufficiently longer time than the pulse duration without distortion. Furthermore, the delay time is adjustable by switching the pumps to control the WLC effect. Unlike the previous works [44], this system can be possibly realized by simpler experimental configurations in room temperature.

B. Data buffering system via Fabry-Perot cavity in free space

Before presenting a distortion free pulse delay system, we briefly review a theoretical model to explain the aspects of a WLC. Fig. 4.1 displays a tunable-bandwidth WLC where a Fabry-Perot cavity contains a dispersive medium. For simplicity, the cavity is assumed to be completely filled with the medium.

We consider a Gaussian input pulse. To calculate the output of the WLC, note the transfer function analysis of a standard cavity [45]. We will find the complex amplitude transfer function for the WLC. First, let us start with a monochromatic optical wave $E_{in}(\omega) = E_0 e^{j\omega t}$ incident on the WLC displayed in Fig. 4.1.

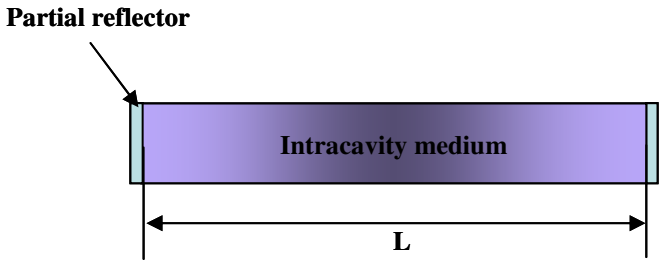

Fig. 4.1. Schematic of a tunable-bandwidth WLC; Two partial reflectors with reflectivity R enclose the intracavity medium.

The input wave can be related to the WLC output as

$$E_{out} = E_0 e^{j\omega t} \times \frac{t^2 e^{-jkL}}{1 - r^2 e^{-2jkL}} \tag{4.1}$$

where E_0 is the field amplitude, L is the cavity length, t and r are the amplitude transmission and reflection coefficients, respectively, (for intensity, $R=r^2$, $T=t^2$ and $R+T=1$) and ω is an angular frequency. The wave number k is expressed as $k = n\omega/c$. Here, n is the refractive index of the intracavity medium, and c is the speed of light in vacuum. For a cavity in the absence of the dispersive medium, i.e. empty cavity, n is simply equal to the index of vacuum (=1). For our case of the dispersive intracavity medium, n is a function of ω. As such, the wave number for the WLC can be modified as $k(\omega) = n(\omega)\omega/c$. $n(\omega)$ is expressed by Taylor expansion around ω_0 as $n(\omega) = n_0 + (\omega - \omega_0)n_1 + (\omega - \omega_0)^3 n_3$, where n_0 is the mean index of the medium, $n_1 = dn/d\omega\big|_{\omega=\omega_0}$ and $n_3 = (1/6)\,dn^3/d\omega^3\big|_{\omega=\omega_0}$. The resonance frequency of the cavity before creating dispersion in the medium is given by ω_0. More specifically, it is equal to

the center frequency of a gain doublet so that the medium can obtain a negative dispersion asymmetrically around ω_0 [15]. In the previous WLC demonstration, the bi-frequency pumps provided two gain lines. The negative dispersion was created in the region between the two gains. ω_0 was in the middle of the gain doublet such that the dispersion was asymmetric around it. Due to the asymmetric dispersion, we can consider $n_2 = (1/2)d^2n/d\omega^2\big|_{\omega=\omega_0}$ as a null value and thus eliminate n_2 in the Taylor expansion of $n(\omega)$. The cavity response for the tunable-bandwidth WLC is obtained by inserting the Taylor expansion of $n(\omega)$ into k of $t^2e^{-jkL}/(1-r^2e^{-2jkL})$ in Eq.(4.1). If the cavity represents a general system, then one can regard the cavity response as a transfer function of the system. For the case of WLC, the transfer function can be expressed as $H_{WLC}(\omega) = t^2e^{-jkL}/(1-r^2e^{-2jkL})$ where $k = \{[n_0 + (\omega-\omega_0)n_1 + (\omega-\omega_0)^3 n_3]\omega\}/c$. For the empty cavity, the transfer function can be written as $H_{EC}(\omega) = t^2e^{-jk_0L}/[1-r^2e^{-2jk_0L}]$ where $k_0=\omega/c$.

Next, we extend the monochromatic input to an arbitrary pulse. Consider the Fourier transform of the pulse, $S(\omega)$. By convolution theorem, the WLC output is the inverse Fourier transform of the product of $S(\omega)$ and $H_{WLC}(\omega)$. As such, the output intensity $|S_{WLC}(t)|^2$ is expressed as $S_{WLC}(t) = 1/\sqrt{2}\int_{-\infty}^{\infty} S(\omega)H_{WLC}(\omega)\exp(j\omega t)d\omega$. We choose the input pulse to be of the form $S(t) = \exp(-t^2/t_0^2)\exp[j(\omega_0+\xi)t]$, whose Fourier transform is written as $S(\omega) = t_0/\sqrt{2}\exp[\{(\omega-\omega_0-\xi)t_0\}^2/4]$. The carrier frequency of

the pulse is upshifted as much as ξ from the empty cavity resonance (ω_0). A reference pulse propagates in the free space for as much as the cavity length L. Likewise, the reference pulse after traveling the length L is $S_{free}(t) = 1/\sqrt{2}\int_{-\infty}^{\infty} S(\omega)H_{free}(\omega)\exp(j\omega t)d\omega$ where $H_{free}(\omega) = \exp(-j\omega L/c)$. Let us next consider the group velocity of the pulse in the WLC. The phase ϕ for a single frequency wave after passing through the cavity can be written as

$$\phi = \omega t - \frac{\omega n_{eff} L}{c} \tag{4.2}$$

where n_{eff} is an effective refractive index induced by the WLC. For simplicity, we assume that the pulse propagates through the WLC without distortion. All the frequency components of the input pulse are added in phase [12] at the exit of the WLC so that $d\phi/d\omega=0$. We can define the group velocity as $v_g=L/t$. After differentiating Eq.(4.2) with respect to ω, $L/t(=v_g)$ can be expressed as $c/[n_{eff} + \omega(d n_{eff}/d\omega)]$. From $v_g = c/[n_{eff} + \omega(d n_{eff}/d\omega)]$, we obtain the group index as $n_g = n_{eff} + \omega(dn_{eff}/d\omega)$. Next consider n_g in terms of the phase angle of H_{WLC}. The complex transfer function H_{WLC} is written as $|H_{WLC}|\exp(j\angle H_{WLC})$ in terms of the amplitude ($|H_{WLC}|$) as well as the phase angle ($\angle H_{WLC}$). The WLC output in frequency domain can be written as $S_{WLC}(\omega)=|H_{WLC}|\exp(j\angle H_{WLC})S(\omega)$. One can note that $\angle H_{WLC}(\omega)$ is the phase resulting from the propagation inside the WLC thereby being equal to the second term in Eq.(4.2).

From $\angle H_{WLC}(\omega) = -(\omega n_{eff} L)/c$, we can derive $n_{eff} = -(c\angle H_{WLC})/(\omega L)$. Inserting n_{eff} into $n_g = n_{eff} + \omega(dn_{eff}/d\omega)$, it leads us to

$$n_g = -\frac{c}{L}\frac{d\angle H_{WLC}}{d\omega} \tag{4.3}$$

In the treatment of pulse distortion, it is convenient to consider the group index dispersion, i.e. group velocity dispersion. The degree of pulse stretch (or compression) in time domain after propagation through a medium of length L is given by $\Delta T \approx (L/c)(dn_g/d\omega)\Delta\omega$ where $\Delta\omega$ is that pulse bandwidth [12]. By inserting Eq.(4.3) into ΔT, we obtain $\Delta T \approx -(d^2\angle H_{WLC}/d\omega^2)\Delta\omega$. From ΔT, we can notice that the pulse maintains its original shape after propagation on the condition that its spectrum belongs to the spectral region where $d^2\angle H_{WLC}/d\omega^2 = 0$.

Figs. 4.2~3 display the transfer functions $|H_{WLC}|^2$, $|H_{EC}|^2$, the phases $\angle H_{WLC}$,$\angle H_{EC}$, the frequency spectrum of the input pulse $|S|^2$ and the output pulses

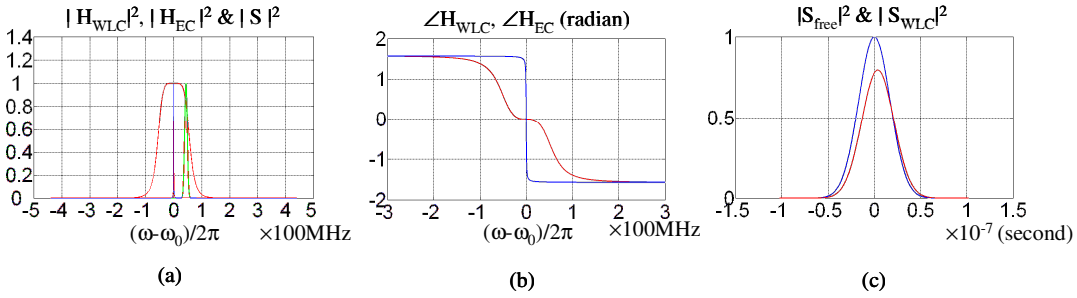

Fig. 4.2. (a) Transfer functions for empty cavity (blue) and for WLC (red), and the frequency spectrum of Gaussian input (green). (b) Phase of H(ω) for empty cavity (blue) and for WLC (red). (c) $|S_{free}|^2$ (blue) and $|S_{WLC}|^2$ (red). The parameters of the intracavity medium are $n_1 = -8.223\times10^{-16}$/rad, and $n_3 = 5.223\times10^{-35}$/rad^3.

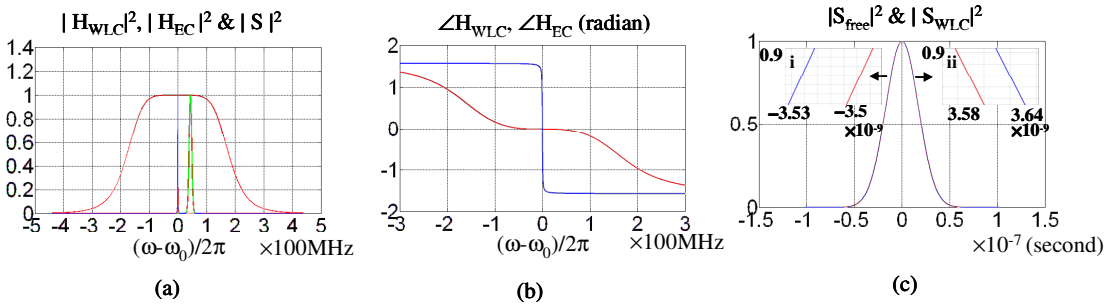

Fig. 4.3. For the medium with n_1=−8.223×10^{-16}/rad, and n_3=1.723×10^{-36}/rad^3. (a) Transfer functions for empty cavity (blue) and for WLC (red), and the frequency spectrum of Gaussian input (green). (b) Phase of H(ω) for empty cavity (blue) and for WLC (red). (c) $|S_{free}|^2$(blue) and $|S_{WLC}|^2$ (red).

$|S_{WLC}|^2$, $|S_{free}|^2$. For illustration, we choose the values for the cavity as length (L)=5cm, Finesse=999(R=0.999), and Full width at half maximum (FWHM)=2.9MHz.

The mean index of a dispersive medium (n_0) is assumed to be equal to that of vacuum i.e. n_0=1. Provided that n_3=0, n_1 is adjusted to fulfill the ideal WLC condition [15]. For our case in which the cavity is completely filled with the dispersive medium, the group index n_g is equal to 0. On the ideal condition, the WLC linewidth is infinite. Next, we take into account the additional dephasing effect on the linewidth due to n_3. We include n_3 so that the dephasing away from ω_0 results in a cavity response drop, i.e. a finite WLC linewidth. The input pulse width is $\Delta\nu_{pulse}$=29MHz (t_0=34ns) and the carrier frequency is shifted from ω_0 by ξ=1.5×$\Delta\nu_{pulse}$. Therefore, the frequency spectrum of the pulse is sufficiently separated from the spectral region of an empty cavity resonance. Later, we will discuss the necessity for the shifted pulse in our delay system.

For the WLC associated with $n_3=5.223\times10^{-35}$, Fig. 4.2(a) indicates the pulse spectrum ($S(\omega)$) belonging to the spectral region where the cavity response ($|H_{WLC}|=1$) begins to drop from the constant value ($|H_{WLC}|=1$). Since the amplitude of the transfer function decreases within the pulse spectrum, we can observe the reduced intensity of the output pulse (red) in Fig. 4.2(c). Fig. 4.2(b) illustrates $d\angle H_{WLC}/d\omega<0$ in the pulse spectrum and thus $n_g>1$. Due to $v_g<c$, the pulse slows down compared to the reference which propagates the free space. Consider $d^2\angle H_{WLC}/d\omega^2$: the pulse spectrum partially exists in the spectral region of $d^2\angle H_{WLC}/d\omega^2 \neq 0$ and thus the pulse compression occurs as indicated in Fig. 4.2(c).

Fig. 4.3(a) suggests that for $n_3=1.723\times10^{-36}$, WLC resonates over broader spectral range than in the case of $n_3=5.223\times10^{-35}$. The input pulse spectrum mostly belongs to the spectral region where $d\angle H_{WLC}/d\omega = 0$ and $d^2\angle H_{WLC}/d\omega^2 = 0$. Minor frequency components belong to the spectral region in which $d^2\angle H_{WLC}/d\omega^2 \neq 0$. Hence, in the insets of Fig. 4.3(c), $S_{WLC}(t)$ doesn't exhibit time delay or advancement but minor pulse compression.

In order to design a pulse delay system, we utilize the characteristics of the WLC in Fig. 4.3. We choose the shifted Gaussian pulse $S(\omega) = t_0/\sqrt{2}\exp[\{(\omega-\omega_0-\xi)t_0\}^2/4]$ to be an input pulse. Fig. 4.4 displays that the proposed system consists of two WLCs. The intermediate region between the WLCs is surrounded by a partial reflector (PR) on

the right hand side (RHS) of the left WLC (LWLC), and a PR on the left hand side (LHS) of the right WLC (RWLC).

In the previous WLC demonstration, bi-frequency pumps interact with the intracavity medium to create negative dispersion [15]. In the absence of the pumps, the dispersion vanished and thus WLC was converted to an ordinary cavity. Since n_0

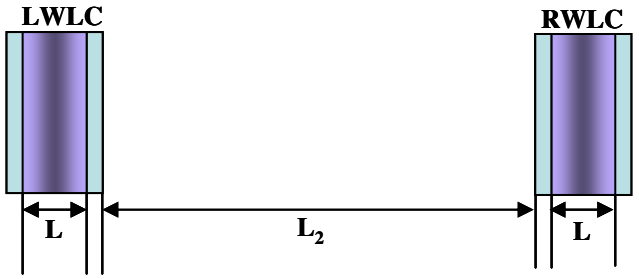

Fig. 4.4. Diagram of the proposed pulse delay system. Two identical WLCs are separated by L_2. Left and right white light cavity is represented by LWLC and RWLC, respectively.

corresponds to the mean index of vacuum, the transfer functions of the two WLCs in the absence of the WLC effect correspond to that of an empty cavity. The slope of the dispersion is determined by the separation of the pump frequencies as well as the pump intensity. As such, n_1 and n_3 are controlled by changing the pump parameters to manipulate the linewidth of LWLC (or RWLC). We use such tunable linewidth WLC to operate the delay system. Here, consider an operation scheme to delay the pulse without distortion. Imagine a Gaussian data pulse that has a broader bandwidth than the linewidth of RWLC without the WLC effect. The carrier frequency is shifted by $1.5\times\Delta\nu_{pulse}$ from the cavity resonance (ω_0). Before the pulse enters into RWLC, one activates the WLC effect. Fig. 4.3(c) suggests the output pulse of LWLC is neither

delayed nor distorted compared to the reference. We assume that the intermediate zone between LWLC and RWLC is long enough to spatially confine the data pulse. Afterward, the pulse propagates in the intermediate zone of the two WLCs and reaches the LHS PR of RWLC. Recall that RWLC in the absence of the WLC effect corresponds to the empty cavity. The pulse spectrum within the FWHM ($\Delta\nu_{FWHM}$=2.9MHz) of the cavity resonates with the empty cavity. Such spectral components can transmit through it and is leaked out of RWLC. Since the pulse is sufficiently shifted from the resonant frequency of ω_0, however, RWLC becomes a simple reflector with the reflectivity of R. The pulse is reflected with minor loss due to the transmission of the PR. Likewise, before the reflected pulse returns to the RHS PR of LWLC, we deactivate the WLC effect so that the pulse is reflected again without the leakage of spectral components. It will travel multiple rounds between the two WLCs until we activate the WLC effect on RWLC. As soon as RWLC is activated, the pulse passes through RWLC without the loss of frequency components. We can extract the data pulse from the buffer system without any distortion. Compared to the reference, the signal will be delayed by the amount of time spent inside the intermediate zone. Next, let us find a transfer

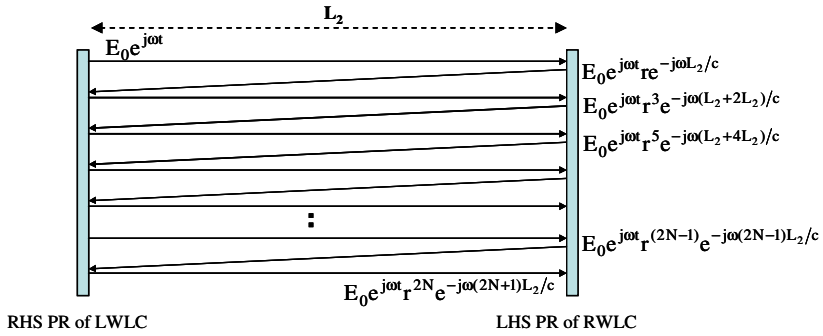

Fig. 4.5. Monochromatic wave travels N rounds between two reflectors.

function for the buffer system. First, consider a transfer function in the intermediate zone. As illustrated in Fig. 4.5, a monochromatic wave begins to propagate from RHS PR of LWLC and travels N rounds. The wave before LHS PR of RWLC is written as $E_0 e^{j\omega t} R^N e^{-j\omega(2N+1)L_2/c}$ where L_2 is the distance between the two PRs. Since $E_0 e^{j\omega t}$ represents the input wave, one can write the transfer function as

$$H_i(\omega) = R^N e^{-j\omega(2N+1)L_2/c} \tag{4.4}$$

Since $H_{WLC}(\omega)$ describes the response of the WLCs, Eq.(4.4), together with $H_{WLC}(\omega)$, leads us to a transfer function $H_{total}(\omega)$ of the pulse delay system in Fig. 4.4. $H_{total}(\omega)$ can be expressed as $H_{total}(\omega) = H_L(\omega)H_i(\omega)H_R(\omega)$ where $H_R(\omega)$ and $H_L(\omega)$ are the transfer functions of RWLC and LWLC, respectively. We employ the identical WLCs so that $H_R(\omega) = H_L(\omega) = H_{WLC}(\omega)$. Again, by convolution theorem, the output of the delay system can be written as

$$S_{system}(t) = \frac{1}{\sqrt{2}} \int_{-\infty}^{\infty} H_{total}(\omega) S(\omega) \exp(j\omega t) d\omega \tag{4.5}$$

Likewise, the reference pulse propagates through free space by the length of the data buffering system as well, and thus $S_{free}(\omega)$ is $S_{free}(t) = 1/\sqrt{2} \int_{-\infty}^{\infty} S(\omega) H_{free}(\omega) \exp(j\omega t) d\omega$ where $H_{free}(\omega) = \exp(-j\omega(2L + L_2)/c)$. Fig. 4.6 graphically illustrates $S_{free}(t)$ and $S_{system}(t)$. For illustration, we consider L_2=2557m. The WLCs and the input data pulse are the same as used in Fig. 4.3. The numerical simulation suggests that for one round trip (N=1), the data pulse is delayed by as much as $2L_2/c = 1.7 \times 10^{-5}$ sec. For one

hundred round trips (N=100), the delay time is observed as $200L_2/c = 1.7\times10^{-3}$ sec with an intensity attenuation due to the transmission of the two PRs. It is equal to approximately 5000 times input pulse duration ($\approx 1.7\times10^{-3}/t_0 = 5000$). The bandwidth of a delay system is defined as the maximum frequency spectrum width of a data pulse that the system can delay without distortion. One can note that $\Delta\nu_{FWHM}$ of WLC is an important parameter to determine our system bandwidth and it increases up to 340MHz in the presence of the WLC effect as shown in Fig. 4.3(a). The data pulse of $\Delta\nu_{pulse}$=29MHz is loaded to the intermediate zone through LWLC without distortion. The carrier frequency of the pulse is deviated from the empty cavity resonance by as much as $1.5\times\Delta\nu_{pulse} = 33.5$MHz. Since $\Delta\nu_{FWHM}$ of the WLCs in the absence of the WLC effect corresponds to 2.9MHz, the pulse is non-resonant with the cavities. We eliminate the WLC effect on LWLC after loading to the intermediate zone. The pulse can be spatially confined inside the delay zone until we activate RWLC. One can either downshift or upshift an input data pulse from the empty cavity resonance. To calculate the system bandwidth, we note that the spectral region is the WLC resonance spectrum region with the exclusion of the empty cavity resonance peak. We shift the carrier frequency of the pulse within the spectral range. . Therefore, our system bandwidth $\Delta\nu_{system}$ is approximately equal to (340–2.9)/2≈168MHz. Due to the tunable linewidth of WLC, it is easily expandable. Therefore, one can easily adjust the delay bandwidth to be wider than that which current systems can provide. Another remarkable feature is that the delay time is independent of $\Delta\nu_{system}$ and simply corresponds to the time elapse inside

the region between LWLC and RWLC. Therefore, our system gives a solution to delay time-bandwidth product encountered by delay systems in current optical communication.

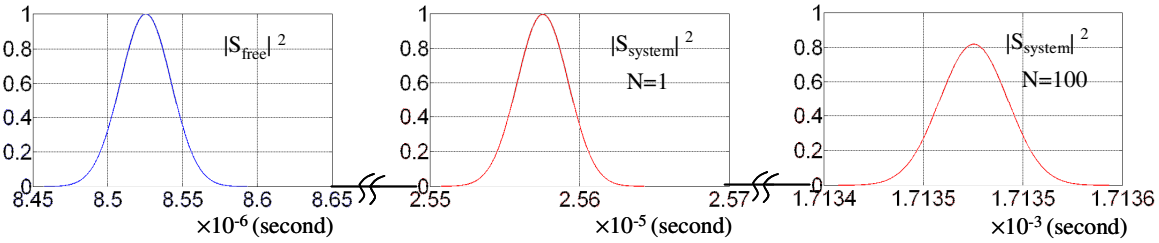

Fig. 4.6. Series of pulses in time domain. At t=0, the reference and the data pulse are launched at the entrance of the RWLC. Blue is the reference pulse ($S_{free}(t)$). It propagates the optical path of $2L+L_2$ in free space and the center of the pulse appears at $t = (2L + L_2)/c \approx 8.55 \times 10^{-6}$ sec ond . The data pulses are observed at $t = (2L + 3 \times L_2)/c \approx 2.56 \times 10^{-5}$ second for one round trip (N=1) and $t = (2L + 201 \times L_2)/c \approx 1.71 \times 10^{-3}$ second for N=100.

CHAPTER V

DATA BUFFER SYSTEM IN FIBER RESONATORS

A. Motivation for data buffer in fiber optics

Slow light phenomenon in optical fibers has been of interest due to its applicability to current optical devices for fiber optic communication such as optical buffers, optical delay lines and fast memory access [6]~[9]. A nano-second data pulse was delayed by the interaction of the pulse with a single Brillouin pump. However, the delay time was less than the pulse duration which is a short delay from the view of practical points. A data pulse was stored by the writing pulse (pulsed Brillouin pump) as an acoustic excitation. The read-out pulse converted such excitation to the original data pulse [42]. The storage time was several times the data pulse duration. Since the pulse was stored in the form of the decaying acoustic disturbance, however, the storage time in this scheme was limited by the acoustic lifetime.

In chapter IV, we have shown that fast-light technique can be paradoxically employed to build a data buffering system. In a so called white light cavity (WLC), a cavity contains fast-light medium whose negative dispersion compensates for wavelength change. As such, it resonates over a broader spectral range compared to an empty cavity of equal length and finesse without the reduction of cavity build-up [15]. The buffering system was composed of two WLCs in Fabry-Perot (FP) and the intermediate delay zone. In theoretical analysis, a data pulse was delayed several thousand times the pulse duration with minor attenuation. However, the intermediate

zone was required to be long enough to obtain a long delay time so that it is hard to be constructed in free space optics.

Coupling characteristics between a ring resonator and a waveguide have been important research areas in optical communication [46]~[50]. Their physical manifestations such as in power transfer and phase are consistent with that of fiber ring resonators [51]~[54]. A ring resonator's coupling coefficient is represented by the transmission in FP while transmission coefficient corresponds to reflection. In fast-light demonstration based on stimulus Brillouin scattering (SBS), negative dispersion was produced by bi-frequency Brillouin pumps in optical fibers [7]. Therefore, we can expect that the combination of the fiber resonator with the fast-light technique possibly provides a solution to create the WLC effect in a fiber resonator.

For more practical application to existing telecommunication, we design a fiber white light cavity in this chapter. We employ it to build a fiber-based data buffering system. We propose that the broadband negative dispersion (on the order of GHz) is obtained by using two broadened gains, and thus the system bandwidth can be extended to multiple times the Brillouin frequency (ν_B: 8~12GHz [55], [56]).

B. Application of fiber resonators to data buffering system

First, let us review the optical fiber resonator [46], [47] in fig. 5.1(a). We are interested in the field amplitude transfer characteristic b_1/a_1 of this configuration. Provided that a 2 by 2 coupler is internally lossless, the relationship between the complex amplitudes a_i and b_i can be described by the matrix for a 2 by 2 coupler

$$\begin{bmatrix} b_1 \\ b_2 \end{bmatrix} = \begin{bmatrix} \sqrt{1-k} & j\sqrt{k} \\ j\sqrt{k} & \sqrt{1-k} \end{bmatrix} \begin{bmatrix} a_1 \\ a_2 \end{bmatrix} \tag{5.1}$$

where k is the intensity coupling coefficient. In addition, the transmission of the resonator can be described as $a_2 = \alpha e^{j\theta} b_2$ in terms of the internal transmission factor α and the round trip phase shift θ. For α=1, the coupled field a_2 travels one round without attenuation. The phase shift θ is written as $-\omega n(\omega) L/c$ where L is the circumference of the ring resonator. n(ω) is the refractive index of the fiber. In order to explain the induced dispersion by SBS, we consider Taylor expansion of n(ω) about the cavity resonance frequency ω_0. ω_0 is close to the Stokes frequency $\omega - \nu_B$ where ω is the frequency of an incident laser beam (Brillouin single pump) and ν_B is the Brillouin shift frequency. Using Eq.(5.1) together with $a_2 = \alpha e^{j\theta} b_2$, we can derive the ratio of the complex transmission amplitude to that of the input,

$$\frac{b_1}{a_1} = \frac{\sqrt{1-k} - \alpha e^{j\theta}}{1 - \alpha\sqrt{1-k}\, e^{j\theta}} \tag{5.2}$$

Likewise, the input and the circulating field are related by

$$\frac{a_2}{a_1} = \frac{j\alpha\sqrt{k}\, e^{j\theta}}{1 - \alpha\sqrt{1-k}\, e^{j\theta}} \tag{5.3}$$

Next, we consider a fiber resonator coupled to another fiber. As can be seen in Fig. 5.1(b), the input port of the second coupler is connected to that of the first coupler to construct a semicircle. Another semicircle is constructed by likewise connecting the output ports of the two couplers. The two semicircles form a closed loop. This configuration can be regarded as the microresonator coupled to a second waveguide in

Ref. 46. It will be used as a building block for our fiber-based data buffering system. In the presence of the second coupler, we define the intensity coupling coefficients k_1 and k_2 (the subscripts '1' and '2' represent 'first' and 'second' couplers, respectively) and

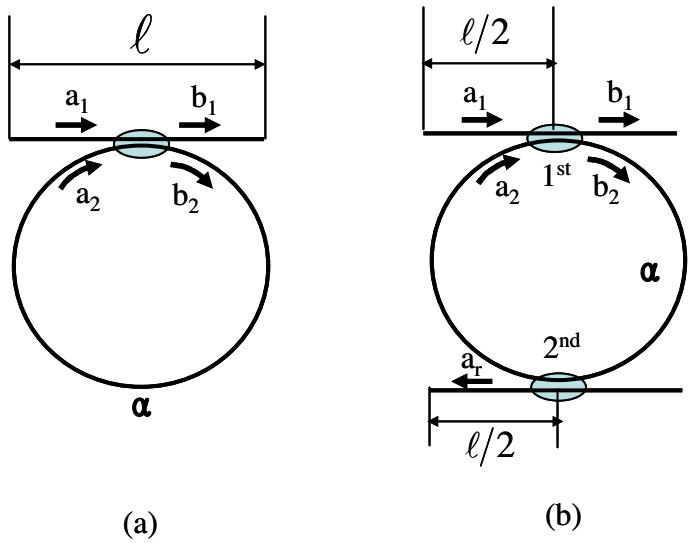

Fig. 5.1. Schematics of (a) fiber ring resonator, (b) ring resonator coupled to a fiber.

modify the internal transmission from α to $\alpha\sqrt{1-k_2}$. Substituting k_1 and $\alpha\sqrt{1-k_2}$ into k and α in Eq.(5.3) respectively, the ratio of the circulating amplitude to the input in the new configuration is written as

$$\frac{a_2}{a_1} = \frac{j\alpha\sqrt{k_1}\sqrt{1-k_2}e^{j\theta}}{1-\alpha\sqrt{1-k_1}\sqrt{1-k_2}e^{j\theta}} \tag{5.4}$$

The transmitted amplitude b_1 is related to a_1 by,

$$\frac{b_1}{a_1} = \frac{\sqrt{1-k_1}-\alpha\sqrt{1-k_2}e^{j\theta}}{1-\alpha\sqrt{1-k_1}\sqrt{1-k_2}e^{j\theta}} \tag{5.5}$$

Likewise, we also change from $a_2 = \alpha e^{i\theta} b_2$ to $a_2 = \alpha\sqrt{1-k_2}e^{j\theta}b_2$. Considering the power transfer from b_2 to a_r through the second coupler, we write,

$$a_r = \sqrt{\alpha} j \sqrt{k_2} e^{j\frac{\theta}{2}} b_2 \tag{5.6}$$

Inserting $a_2 = \alpha\sqrt{1-k_2}e^{j\theta}b_2$ into Eq.(5.4), expressing a_2 in terms of a_1 and substituting b_2 into Eq.(5.6), we obtain a_r/a_1,

$$\frac{a_r}{a_1} = \frac{-\sqrt{\alpha}\sqrt{k_1}\sqrt{k_2}e^{j\frac{\theta}{2}}}{1-\alpha\sqrt{1-k_1}\sqrt{1-k_2}e^{j\theta}} \tag{5.7}$$

where the round trip phase shift θ is expressed as $-\omega n(\omega)L/c$ and L is the circumference of the closed loop. Dispersion in the fiber loop via SBS process can be considered by using Taylor expansion of $n(\omega)$ about ω_0 as

$$n(\omega) = n_0 + (\omega-\omega_0)n_1 + (\omega-\omega_0)^3 n_3,\ n_1 = dn/d\omega\big|_{\omega=\omega_0},\ n_3 = (1/6)dn^3/d\omega^3\big|_{\omega=\omega_0}$$

where n_0 is the mean index of the fiber, and ω_0 is the cavity resonance frequency.

Fig. 5.2 displays $(|b_1|/|a_1|)^2$ and $(|a_r|/|a_1|)^2$ in the absence of dispersion (blue line, n_1=0, n_3=0) and in the presence of negative dispersion (red line, n_1<0, $n_3\neq0$). We consider $|a_1|$=1 so that $|b_1|^2$ and $|a_r|^2$ are normalized to the input. It is assumed that the internal loss is negligible (α=1). We choose n_1 to fulfill ideal White Light Cavity (WLC) condition [15]. For our case in which the length of the dispersive medium is equal to the circumference of the ring resonator, the ideal WLC condition is that the group index in the dispersive fiber n_g is zero [15]. Next, n_3 is adjusted so that the WLC linewidth has finite value. For other parameters, we choose k_1=k_2=0.01, $\ell = 1\text{m}$, n_0=1.45 and L=10m where L is the circumference of the closed fiber loop. For the ordinary ring resonator $n(\omega)$ =n_0, the input completely transfers to the output only at resonance. For the

resonator with the WLC effect, the resonant spectral region is expanded without the build-up loss. As such, frequency components of the input signal fully transmit through the resonator in the presence of the WLC effect.

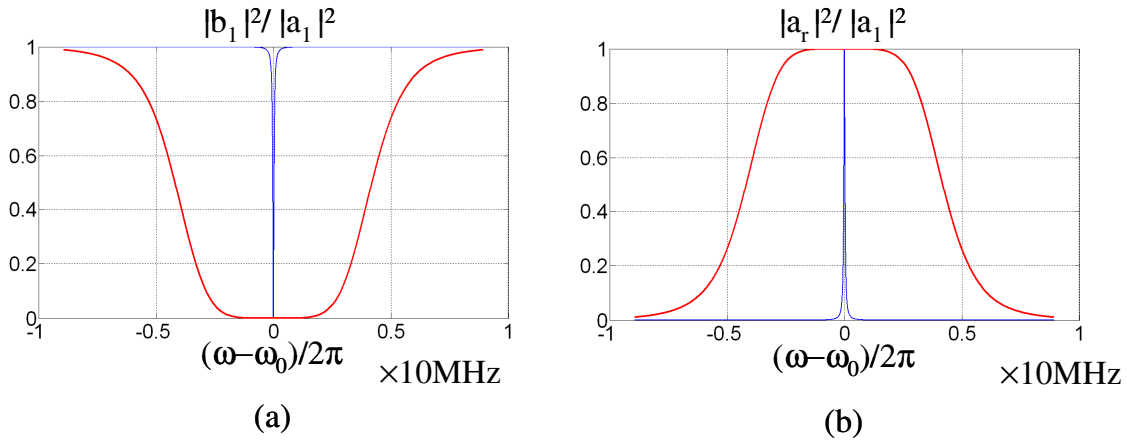

Fig. 5.2. Power transfer of the configuration associated with Fig. 5.1(b). (a) $|b_1|^2/|a_1|^2$ (b) $|a_r|^2/|a_1|^2$ for non-dispersive fiber (blue) and for negative dispersion (red) ($n_1 = -1.192\times10^{-15}/\text{rad}$, $n_3 = 1.223\times10^{-32}/\text{rad}^3$).

Next, we take into account Eq.(5.5) and Eq.(5.7) as the transfer functions of the configuration in Fig. 5.1(b). $H_{b1,a1}$ corresponds to Eq.(5.5). H_O and H_{WLC} represent Eq.(5.7) with $n(\omega)=n_0$ and with $n(\omega) = n_0 + (\omega-\omega_0)n_1 + (\omega-\omega_0)^3 n_3$, respectively. We use the subscript "o" for the ordinary fiber cavity in the absence of dispersion, and "WLC" for the cavity with the WLC effect. For H_{WLC}, we choose n_1 and n_3 equal to the values used in Fig. 5.2. In the previous Fabry-Perot (FP) analysis, we derived the group index n_g for pulse propagation through FP in terms of $\angle H_{WLC}$. Now, we are interested in n_g associated with the configurations in Fig. 5.1. The phase $\angle H_i(\omega)$ is the contribution of

the ring resonators to the total phase (the subscripts 'i' denotes O, WLC, or b1,a1). The phase shift associated with the propagation through the resonators is expressed by $(\omega n_{eff}\ell)/c = (n_0\omega\ell)/c - \angle H_i$ in terms of the fiber mean index n_0 and the effective refractive index of the resonators n_{eff}. Deriving n_{eff} as a function of $\angle H_i$ and inserting n_{eff} into $n_g = n_{eff} + \omega(dn_{eff}/d\omega)$, one can obtain n_g as

$$n_g = n_0 - \frac{c}{\ell}\frac{d\angle H_i}{d\omega} \tag{5.8}$$

Pulse distortion is characterized by $\Delta T \approx -(d^2\angle H_i/d\omega^2)\Delta\omega$ as done in chapter IV.

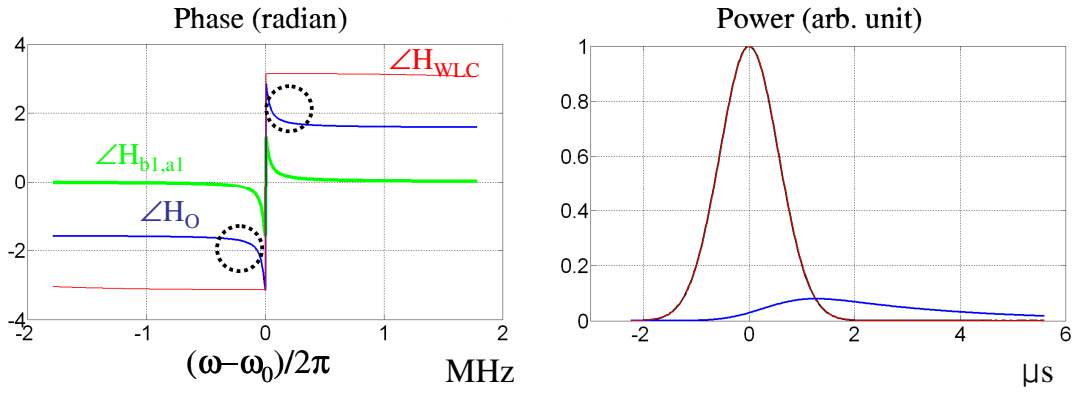

Fig. 5.3. (a) Phases associated with the transfer functions of the system in Fig. 5.1(b), which are $\angle H_{b1,a1} = \arg(b_1/a_1)$ and $\angle H_O = \arg(a_r/a_1)$ in the absence of WLC effect, and otherwise $\angle H_{WLC} = \arg(a_r/a_1)$ for $n_1 = -1.192\times10^{-15}/\text{rad}$, $n_3 = 1.223\times10^{-32}/\text{rad}^3$. (b) Reference pulse after propagating ℓ (black) and system outputs associated with H_O (blue), H_{WLC} (red). Output pulse in the presence of the WLC effect is overlapped with the reference.

Fig. 5.3(a) exhibits $\angle H_{b1,a1}$, $\angle H_O$ and $\angle H_{WLC}$. Fig. 5.3(b) presents the pulse output after propagating distance ℓ through free space (black) and the outputs of the systems associated with H_O (blue) and H_{WLC} (red). The cavity parameters are the same as those used in Fig. 5.2. For illustration, we choose the input pulse to be of the form $S(t) = \exp(-t^2/t_0^2)\exp(j\omega_0 t)$. The pulse bandwidth $\Delta\nu_{pulse}(\approx 1/t_0)$ is 10 times the full width at half maximum (FWHM) of the resonator $\Delta\nu_{cavity}$. By convolution theorem, we obtain the output amplitude as $S_{out}(t) = 1/\sqrt{2}\int_{-\infty}^{\infty} S(\omega)\exp(-jk_0\ell)H_i(\omega)\exp(j\omega t)d\omega$ where $k_0 = n_0\omega\ell/c$. Since the amplitude transmission factor $\alpha\sqrt{1-k_2}$ is equal to the transmission coefficient of the 1st coupler, $\sqrt{1-k_1}$, the system can be regarded as a critically coupled fiber ring cavity. Therefore, $\angle H_{b1,a1}$ is discontinuous at resonance and leaps by as much as π. Such discontinuity and phase jump correspond to the case of a critically coupled microresonator as indicated in Ref. 47. Note that there is a sign difference between our case and Ref. 47. We define the phase shift as $\phi = \omega t - \omega n_{eff}\ell/c$, but Ref. 47 uses $\phi = \omega n_{eff}\ell/c - \omega t$. Due to the additional phase shift π resulting from the second coupler, $\angle H_O$ and $\angle H_{WLC}$ jump at resonance by π more than $\angle H_{b1,a1}$, thereby the phase leap being 2π. $\angle H_O$ indicates $n_g > n_0$ inside the dotted circle. The pulse carrier frequency ω_0 corresponds to the cavity resonance, and $\Delta\nu_{pulse} = 10\times\Delta\nu_{cavity}$. As such, the spectrum of $\Delta\nu_{pulse}$ completely covers the slow light zone corresponding to $d\angle H_O/d\omega < 0$ and $d^2\angle H_O/d\omega^2 \neq 0$ in $\angle H_O$. However, it mostly belongs to the

spectral region of $|H_O|=0$ as well. The pulse output associated with H_O is delayed with serious distortion (attenuated) as displayed in Fig. 5.3(b). $\angle H_{WLC}$ in Fig. 5.3(a) suggests that the system resonance occurs sufficiently broadly to cover the pulse spectrum. Under the resonance condition, the property of WLC exhibits $\left|H_{WLC}\right|=1$, $d\angle H_{WLC}/d\omega=0$, and $d^2\angle H_{WLC}/d\omega^2 \approx 0$. Therefore, the output (red) associated with H_{WLC} in Fig. 5.3(b) indicates that the output pulse is not delayed but maintains its original shape.

Now, we employ the fiber ring cavity investigated in Fig. 5.1(b), 5.2, and 5.3 to design a fiber-based buffering system. In the previously proposed system, the FP based buffering system is composed of right white light cavity (RWLC), intermediate delay zone and left white light cavity (LWLC). Fig. 5.4 displays our fiber-based buffering system.

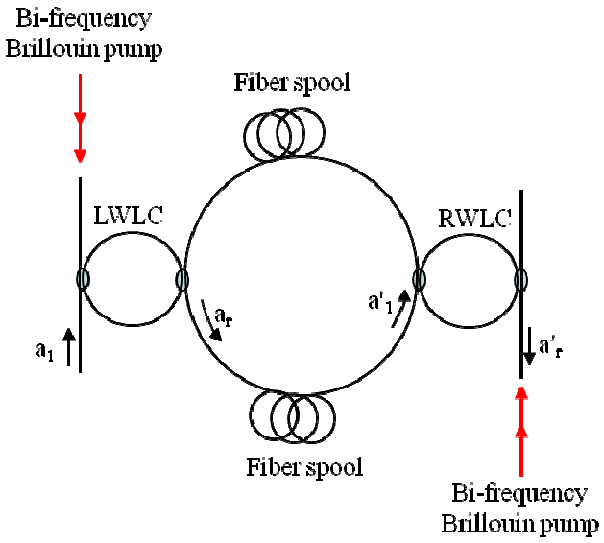

Fig. 5.4. Schematics of the fiber-based buffering system. LWLC and RWLC represent left WLC and right WLC, respectively.

Two ring cavities serve as LWLC and RWLC. The ports at the right side of a left ring resonator ($\mathscr{S}$rr) are connected to the ports at the left side of a right ring resonator ($\mathscr{R}$rr) through fiber spools in order to construct a closed loop delay zone. Let us assume that the bandwidth of the input pulse is much broader than FWHM of the resonators. We consider the operating scheme to delay such broadband input pulse without distortion. To load the pulse to the intermediate delay loop, we turn on bi-frequency Brillouin pumps to activate the WLC effect on the right resonator. The WLC bandwidth is sufficiently wide to resonate over the pulse spectrum. As such, the pulse is successfully loaded retaining its original shape as indicated in Fig 5.3(b). After loading, we turn off the pumps so that the pulse is trapped and circulates inside the delay zone. At this trapping stage, we need to consider the constraint on the carrier frequency of the pulse. If the carrier frequency corresponds to the resonant frequency ω_0 of the fiber ring cavities in the absence of the WLC effect (i.e. ordinary ring cavity), the major spectral components of pulse spectrum around ω_0 resonate with the ring cavity. At every passage through the couplers inside the delay loop, the resonating spectral components leak out through $\mathscr{R}$rr and $\mathscr{S}$rr to cause the pulse to distort. To avoid such loss of frequency components, we shift the carrier frequency from the cavity resonance by several times $\Delta\nu_{cavity}$. The pulse circulates the loop with minor loss associated with $\sqrt{k_1}$ and $\sqrt{k_2}$, which denote the coupling coefficients of the two couplers in $\mathscr{S}$rr, and $\mathscr{R}$rr, respectively. Activating the WLC effect on $\mathscr{R}$rr, we can extract the data pulse from the delay loop. Let us assume that $\mathscr{R}$rr and $\mathscr{S}$rr have same physical parameters ($\sqrt{k_1} = \sqrt{k_2} = \sqrt{k}$, α and

$\Delta\nu_{cavity}$). The amplitude transfer characteristics through the WLCs, $H_{1r}= a_r/a_1$ and $H_{1'r'}= a'_r/a'$, are given by Eq.(5.7). Next, after N multiple round trips, a_r is related to a'_1 by

$$H_{rl'} = \left(\sqrt{1-k_1}\sqrt{1-k_2}\right)^N e^{-jk_0\frac{2N+1}{2}L_2} \tag{5.9}$$

where L_2 is the delay zone length and $k_0 = \omega n_0/c$. Fig. 5.5 displays data pulse outputs after propagating the distance ℓ (reference), 5 round trips, and 10 round trips. For illustration, we choose a Gaussian pulse with the shifted carrier frequency so that $S(\omega) = t_0/\sqrt{2}\exp\left[\{(\omega-\omega_0-\xi)t_0\}^2/4\right]$ where $\xi = 1.5\times\Delta\nu_{pulse}$. After propagating ℓ, the reference pulse is $S_{ref}(t) = 1/\sqrt{2}\int_{-\infty}^{\infty}\exp(-jk_0\ell)S(\omega)\exp(j\omega t)d\omega$. The system output is written as

$$S_{out}(t) = 1/\sqrt{2}\int_{-\infty}^{\infty}\exp(-jk_0\ell)H_{1'r'}(\omega)H_{rl'}(\omega)H_{1r}(\omega)S(\omega)\exp(j\omega t)d\omega \tag{5.10}$$

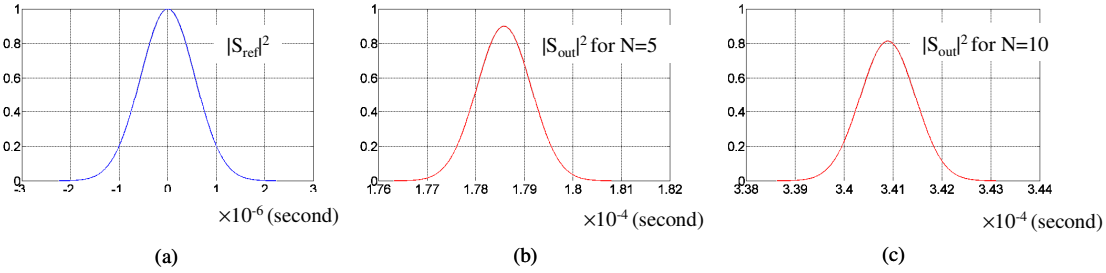

Fig. 5.5. Output pulses sequence of the fiber-based buffering system (a) Reference pulse, (b)5 round trips, and (c) 10 round trips inside the delay zone.

We use the resonator investigated in Fig. 5.2 for $\mathscr{R}$rr and $\mathscr{S}$rr. We choose $\ell = 1\text{m}$ and $L_2 = 6.7\text{km}$. The output pulses lag behind the reference as much as 1.78×10^{-4} sec for N=5 and 3.40×10^{-4} sec for N=10. The delay times are equal to the number of round trips

by $[n_0(2N+1)L_2]/c$. One can observe the attenuation associated with the coupling ratio of the fiber couplers of $\mathscr{R}$rr and $\mathscr{S}$rr during the propagation inside the delay zone.

C. GHz bandwidth negative dispersion

The numerical simulations in Fig. 5.2 suggest that half of the WLC linewidth $\Delta\nu_{WLC}/2$ corresponds to the dynamic range of our system where a data pulse can be delayed without distortion. The WLC linewidth depends on the spectral region of negative dispersion. Since the negative dispersion is produced in the middle of two gain lines under a gain doublet condition, the achievable $\Delta\nu_{WLC}$ was determined by the gain separation δ. It was estimated proportionally to $\delta^{2/3}$ [15]. If the gain separation increases too much, however, the dispersion slope around at the center of the two gains is not negative but close to zero. In the broader gain bandwidth system, the separation distance between the two gains can be increased to obtain broader spectral range of negative dispersion. As such, $\Delta\nu_{WLC}$ increased by broadening gain bandwidth $\Delta\nu$. The Brillouin pump spectrum was broadened by superposing Gaussian white noise on laser diode dc current. Such Brillouin pump was widely used to produce broadband gain profile [57]~[60]. When double Brillouin pumps were separated by $2\nu_B$ (ν_B: Brillouin frequency) and had equal power, the gain bandwidth was expanded to $2\nu_B$ [60]. Now we adopt the double pumps technique in Ref. 60 to produce broadband negative dispersion. We use two groups of the double equal power pumps. Pumps 1 and 1′ (2 and 2′) are separated by ν_B, and pumps 1 and 2 (1′and 2′) by δ. Due to the separation by ν_B as well as the equal power, the loss induced by pump 1 (pump 2) is completely cancelled by the

gain line of pump 1′ (pump 2′). Therefore, we can eliminate the overlapping between the gain and the loss of pump 1 (pump 2) to avoid the gain spectrum distortion. We increase the gain bandwidth $\Delta\nu_B$ to $2\nu_B$ and stop increasing before the gain of pump 1 (pump 2) meets the loss of pump 1′ (pump 2′). In Fig. 5.6(c), two broadened gain lines of pump 1 and pump 2 survive with the separation of δ. In the two groups of the double pumps configuration, however, Fig. 5.6(d) indicates that the loss spectrum of pump 1′ extends beyond the gain of pump 2. Note inside the dotted area. Such overlapping causes the gain distortion. To prevent it, Fig. 5.6(d) suggests that δ should fulfill $\delta + \nu'/2 = 2\nu_B$, where ν' is the width measured along the bottom of the gain. The single gain bandwidth can be more expanded if we employ more pumps in the individual group.

More generally speaking, N pumps create a single gain with the maximum bandwidth of $N\nu_B$ [60]. We consider two groups of pumps. Each group consists of the N pumps. In the two groups, the gain separation is related to ν' by $\delta + \nu'/2 = N\nu_B$. Since the Brillouin frequency of optical fibers is 8~12GHz, δ in the range of GHz can be easily obtained. Negative dispersion occurs in such GHz spectral area between the two gains and thus one can increase the WLC linewidth to be on the order of GHz.

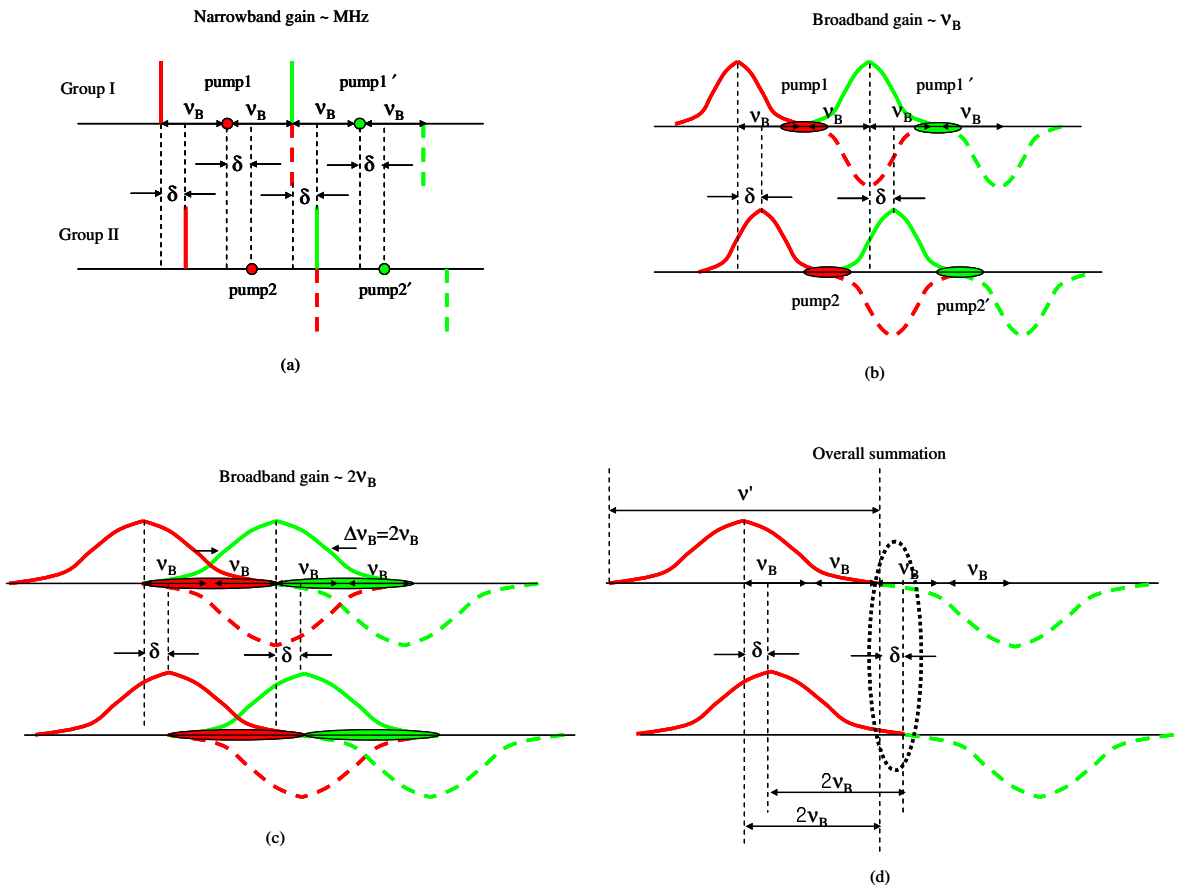

Fig. 5.6. Scheme to create negative dispersion in the scale of GHz. (a) Double pumps (red, and green) in groups I and II. The pumps in green provide gain spectrums to compensate for the loss spectra of the pump in red. (b) Pump spectrum is broadened by Gaussian white noise to create the broadband gain equal to Brillouin shift ν_B. (c) Gain bandwidth is broadened by a factor of $2\nu_B$. (d) Due to the overlap of the gain in group II with the loss in group I, we find the condition that $\delta + \nu'/2 = 2\nu_B$ to avoid gain distortion resulting from such an overlap.

CHAPTER VI

PRELIMINARY EXPERIMENT

A. Motivation

When light propagates through optical fibers, it is back-scattered by the gratings modulated by the refractive index associated with a sound wave of Brillouin shift frequency ν_B [61]. This non-linear process, the so-called stimulated Brillouin scattering (SBS), has been investigated in conventional silica fibers [62], [63] or in fibers with enhanced Brillouin coefficient [56], [64]. It leads to many applications such as Brillouin amplifier, lasing, and optical pulse delay [6], [65]~[68]. Using a Brillouin pump to induce group index change, the data pulse was delayed by less than the pulse duration of 20~50ns [68].

In chapter V, white light cavity (WLC) in a fiber ring resonator was proposed to build a data buffering system to trap data pulses in a long fiber loop. WLC is a cavity that contains anomalously dispersive medium. Such dispersion compensates for the frequency-dependent wavelength change. WLC resonates without the reduction of build up factor over a frequency range that is broader than those of conventional cavities. The proposed buffering system overcame the delay-bandwidth constraint imposed on current slow light technique.

In this chapter, we discuss the construction of a fiber ring cavity based on the Brillouin characteristics of fiber in use. With a resonance enhanced single pump, the 1^{st}, 2^{nd}, and 3^{rd} orders of Brillouin threshold are investigated. For bi-frequency pumps, the

pumps are simultaneously locked to different longitudinal modes of the ring cavity. Two Brillouin lasing modes at the frequencies corresponding to the dual gains exhibit equal intensity without any noticeable cross-talk between two resonant pumps. For the application to WLC in fiber resonators, our analysis of cavity modes, pump beams and dual gains offer proper gain separations as well as free spectral range (FSR) of the cavity.

B. Theoretical background

Before constructing a fiber ring resonator, we review the theoretical model of complex Brillouin gain factors. Afterward, we will show the experimental demonstration to examine the Brillouin characteristics of a fiber. Material density variation induced by optical fields is a source of SBS process. The material system responds to an incident laser light and exhibits the refractive index variations (gratings). The gratings move with a sound wave of frequency Ω away from the incident light. The laser with the frequency of ω_L is scattered by the gratings. Since the acoustic wavefronts are moving with the

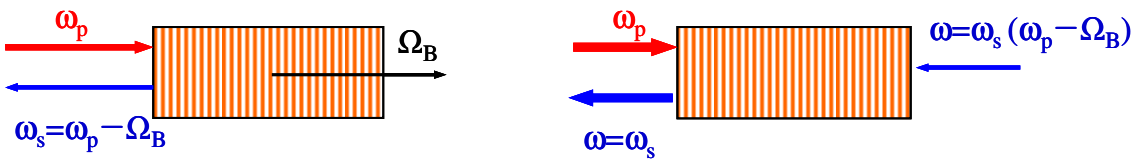

Fig. 6.1. Schematic representation of (a) Stimulated Brillouin Scattering (SBS), (b) an SBS amplifier. ω_p; Pump frequency, Ω_B; Brillouin shift frequency, ω_s; and Stokes frequency.

frequency of Ω from the laser, the counterpropagating scattered light is downshifted as much as Ω from ω_L. As such, it has the Stokes frequency of ω_s ($=\omega_L - \Omega$) indicated in Fig. 6.1(a). In such circumstances, the interference of the laser with the Stokes wave contributes to amplifications of the sound wave, or beating of the sound wave with the laser strengthens the Stokes wave. Material systems exhibit different sound wave frequencies. The frequency of the sound wave is called the Brillouin shift frequency Ω_B. It is an important parameter to characterize an SBS amplifier. Fig. 6.1(b) displays the configuration of the amplifier. In the SBS amplifier, the Stokes field and the laser are externally applied. When ω_s corresponds to $\omega_L - \Omega_B$, the maximum amplification of the sStokes field occurs.

Information about the Brillouin characteristics of fibers is useful in building the ring resonator. Let us consider the coupling of the Stokes field (probe) at frequency ν to the pump field via SBS process. The Stokes field propagates in the fiber with length L where the pump counterpropagates. Assuming that the pump is non-depleted, the slowly varying amplitudes of the Stokes field at steady state after the interaction with the pump field is described by

$$E_S = E_{S0} e^{(\alpha+\beta j)L} \tag{6.1}$$

where E_s is the amplitude after the Brillouin interaction, E_{s0} is the input field amplitude (weak Stokes seed), And α and β are expressed as $\alpha = (g_0 I_P) \Big/ \left\{2(1+4(\nu-\nu_B)^2/\Gamma_B{}^2)\right\}$ and $\beta = \left(g_0 I_P (\nu-\nu_B)/\Gamma_B\right) \Big/ \left\{(1+4(\nu-\nu_B)^2/\Gamma_B{}^2)\right\}$ in terms of the Brillouin frequency ν_B,

gain coefficient g_0 , gain linewidth Γ_B and pump intensity I_p. For the case in which one uses bi-frequency pumps to produce Brillouin gain-doublet, α and β are rewritten as

$$\alpha = \frac{1}{2}\left[\frac{g_0 I_{P1}}{1+4(\nu-\nu_B-\Delta)^2/\Gamma_B{}^2} + \frac{g_0 I_{P2}}{1+4(\nu-\nu_B+\Delta)^2/\Gamma_B{}^2}\right] \tag{6.2a}$$

$$\beta = \frac{g_0 I_{P1}(\nu-\nu_B-\Delta)/\Gamma_B}{1+4(\nu-\nu_B-\Delta)^2/\Gamma_B{}^2} + \frac{g_0 I_{P2}(\nu-\nu_B+\Delta)/\Gamma_B}{1+4(\nu-\nu_B+\Delta)^2/\Gamma_B{}^2} \tag{6.2b}$$

provided the pumps are separated by 2Δ. I_{P1} and I_{P2} are the intensities of the bi-frequency pumps. In the gain-doublet system, the gain separation corresponds to 2Δ. We define the parameter G as $g_0 I_{Pj}/2$ (j=1,2) corresponding to the amplitude gain peak.

C. Brillouin characteristics measurement

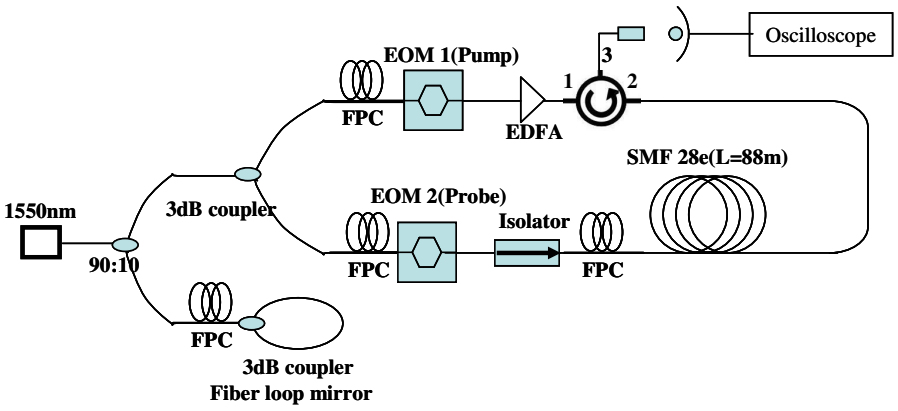

Fig. 6.2. Experimental set-up to measure Brillouin spectrum. Components include: FPC, fiber polarization controller; EDFA, Er-doped fiber amplifier; and EOM, Electro-optic modulator.

Next, we measure the Brillouin frequency, gain linewidth and G factor while increasing the pump power. Fig. 6.2 displays the schematics of the experimental set-up for Brillouin gain spectrum measurements. The light source is 1550nm CW laser diode (LD), (linewidth<1MHz). The LD output is divided by a 90:10 coupler. A 3dB coupler is used to build a fiber loop mirror [69] and 10% of the LD output is inserted into the port of 1m fiber pigtail of the coupler. Hence, the 1m external cavity is implemented by the loop mirror so that it provides optical feedback to decrease the linewidth of LD. The 90% output is divided again by another 3dB coupler. One of two outputs is inserted into an electro-optic modulator (EOM-1) and is augmented by an Er-doped fiber amplifier (EDFA) to serve as the Brillouin pump. The pump from EOM-1 without modulation is used to produce a single gain. To generate the double peaks, the DC voltage on EOM-1 is adjusted to eliminate the fundamental. Two sidebands of EOM-1 provide dual pumps and thus the gain separation corresponds to $2f_M$ (f_M: modulation frequency). The modulation frequency of the EOM-2 is swept by $\Delta\nu$ around ν_B to provide a probe.

Fig. 6.3 illustrates the Brillouin spectrum of 88m Corning SMF-28e fiber. In Fig. 6.3(a), the single gain profile is obtained by scanning around ν_B as much as $\Delta\nu$=40MHz with the step size of 0.5MHz. We increase the pump power until the gain is saturated. The Brillouin shift frequency and gain width are measured as 10.867GHz and ~10MHz, respectively. ν_B is 50 MHz higher and Γ_B is a factor of 3 less than the values from the previous measurement for SMF-28e [62]. In Ref. 62, they used a longer fiber (6.4km) as well as a lower power pump, in the scale of mW, than ours. Hence, the Brillouin interaction length (L) for the given pump is long and thus the pump depletion [63]

occurs to broaden the linewidth by about a factor of six more than in our case. Fig. 6.3(b) illustrates the gain factor, G (meter^{-1}) associated with the gain spectrum displayed in Fig. 6.3(a). Assuming the absence of saturation, we plot the linearly increasing graph (purple line). The slope is calculated from the experimental data for the pump powers of 600 and 800mW. G for the higher power (1, 1.5, 2W) is plotted by the calculated slope.

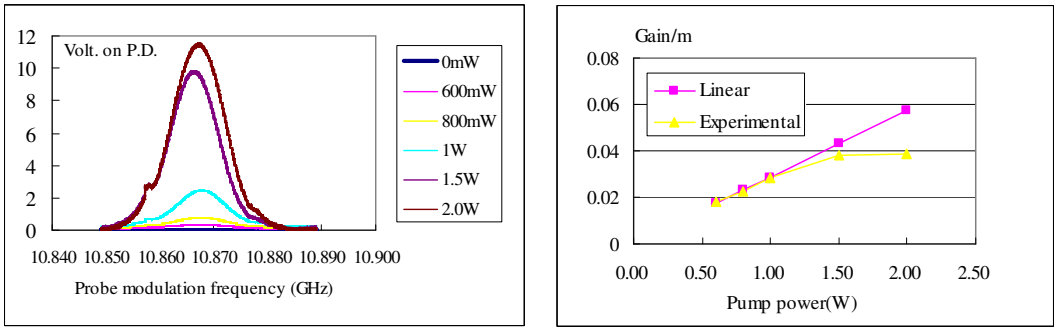

(a) (b)

Fig. 6.3. (a) Brillouin gain spectrum of a 88m single mode fiber. Y axis represents the voltage on photodiode (Volt. on PD). (b) Gs (Gain peak amplitude at resonance: meter^{-1}) for linear increase without saturation and for real experimental data.

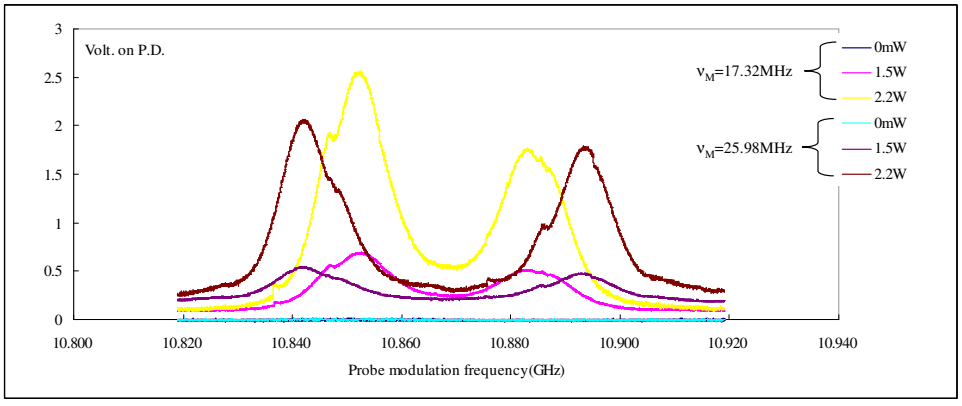

Fig. 6.4. Dual Brillouin gain spectra for the gain separations of 34.64MHz (ν_M =17.32MHz) and 51.96MHz (ν_M =25.98MHz).

In the comparison to the experimental data displayed in the yellow graph, we can confirm that the gain factor, G (meter^{-1}) starts to saturate at the pump of 1.5W.

In Fig. 6.4, the double gain peaks are displayed for the case in which the modulation frequencies of EOM-1 are ν_M=17.32MHz and 25.98MHz. The scan range of the probe is $\Delta\nu$=100MHz. The anti-symmetric double gains result from the unbalanced sideband output of EOM-1. In dual Brillouin gains, the peak of the individual gain approximately corresponds to that of the single gain associated with the single pump power which is equal to a half of the bi-frequency pump power. Γ_B is measured as ~12MHz.

Fig. 6.5 displays the schematics of the experimental setup to demonstrate a Brillouin fiber laser. 90% of LD output is divided by a 3dB coupler. One output is inserted into a Fabry-Perot (FP) with FSR of 37GHz and a finesse of 30. It provides a reference spectrum which corresponds to the LD frequency ν_L. The other is modulated by EOM while suppressing the fundamental ν_L and the remaining two sidebands are amplified by EDFA to generate bi-frequency pumps. For a single pump, we remove the EOM. The coupling ratio of a variable coupler (VC) is set to critical coupling condition [54]. Full width at half maximum (FWHM) of our fiber resonator is measured as 0.23MHz. A lock-in amplifier (LIA) and AC servo lock the cavity length to the pump resonance. First, we observe cascaded Brillouin lasing while the single pump is resonant with the cavity. We adjust the coupling ratio of VC as well as the pump power to attain higher order Brillouins. Fig. 6.6 shows Brillouin lasers monitored by the FP spectrum analyzer. Fig. 6.6(a) indicates that in the presence of a 20mW pump, the smaller peak is

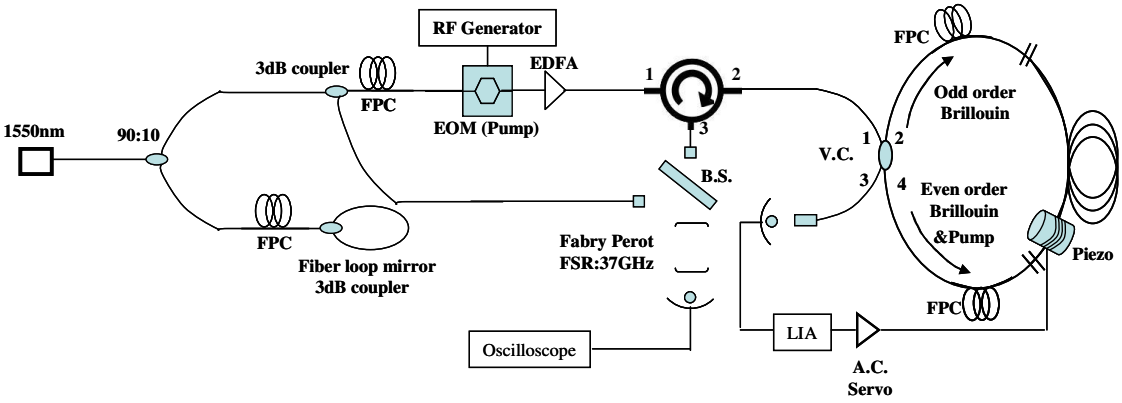

Fig. 6.5. Schematic of cascaded and bi-frequency Brillouin fiber lasers.

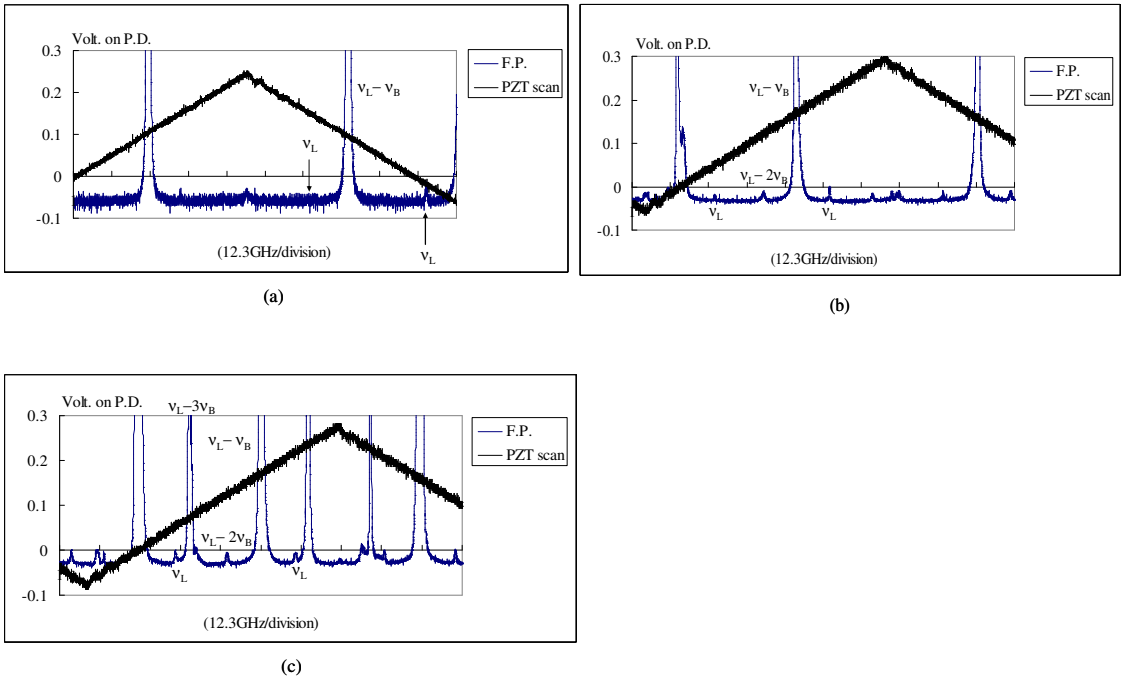

Fig. 6.6. (a) 1st order (Pump power: P=20mW), (b) 1st and 2nd order (60mW), (c) 1st, 2nd and 3rd order (100mW) Brillouin laser.

a back reflection of the pump and the main peak is the 1st order Brillouin. The 2nd order and 3rd order Brillouin lasers are observed at 60mW and 100mW, respectively, as displayed in Fig. 6.6(b) and (c). The separation between adjacent orders of the Brillouin spectra is equal to ν_B (10.867GHz). The clockwise propagating 2nd order Brillouin produces a smaller spectrum peak compared to the odd orders due to high isolation between ports 1 and 2 of VC.

D. Cavity modes, pump spectra and dual gains under Bi-frequency pumps resonance

Based on the measured ν_B and Γ_B in Fig. 6.3 and 6.4, a fiber ring cavity is designed to obtain $N \times FSR = \nu_B$ where N is an arbitrary integer. Our cavity FSR is 17.3262MHz, which is broader than Γ_B. Due to $N \times FSR = \nu_B$, one longitudinal cavity mode is present close to the center of the gain. Provided that FSR is broader than Γ_B, the Brillouin single gain supports only one longitudinal cavity mode at the peak of the gain profile. As such, we can generate a single mode Brillouin laser. Next, for future applications such as white light cavity (WLC) demonstration, let us consider the case in which the bi-frequency pumps are simultaneously resonant with the cavity. Fig. 6.7(a) and (c) illustrate EOM outputs monitored by the fiber cavity. They consist of two sidebands $\nu_L \pm \nu_M$ and the fundamental ν_L. The two sidebands equally share the cavity length of L for $\nu_M = (2k+1)/2 \times FSR$, and L^* for $\nu_M = k \times FSR$ where k is 0 or a positive integer. For L^*, k=0 implies that EOM provides the fundamental. However, the sidebands occupy the different modes. For example, $(N+2)\lambda_1 = L$ and $(N+3)\lambda_2 = L$,

where λ_1 and λ_2 are the wavelengths associated with $\nu_L-\nu_M$ and $\nu_L+\nu_M$ (ν_M =8.6631MHz) respectively, N is an arbitrary positive integer. After eliminating ν_L, the cavity is locked at L or L^* so that $\nu_L\pm\nu_M$ simultaneously resonate in the cavity. Fig. 6.7(b) and (d) display the configurations of cavity modes (thick bars), double gains and pump spectrums (color arrows). The bi-frequency pumps create the gain-doublet which is represented by the same color as the pumps in use. Fig. 6.7(b) illustrates that for the cavity lock to L, the even number of cavity modes appear between the two gains. No cavity mode exists at the center of two gains. If the length is changed to L^*, the cavity modes are displaced from the modes of the cavity with length L by $\delta = 1/2 \times \mathrm{FSR}$ indicated in Fig. 6.7(d). Therefore, the center of the two gains coincides with the cavity mode corresponding to $\nu_L-\nu_B$. To explain the lasing mode in Fig. 6.6, note that the single cavity mode supports the center of the single gain (brown). As such, the Brillouin laser demonstrated in Fig. 6.6 is a single mode. The WLC demonstration requires the cavity mode to be equal to $\nu_L-\nu_B$ or to deviate from $\nu_L-\nu_B$ by a small factor in comparison to gain separation. The gain doublet is symmetrically arranged around $\nu_L-\nu_B$. Since we can scan a probe around $\nu_L-\nu_B$ to observe the WLC effect, the configurations illustrated in Fig. 6.7(d) are more suitable for WLC demonstration. However, it could have the residual fundamental after suppression; thereby the residual is possibly resonant with the cavity to distort the double gain profile. Since the sidebands are locked onto a position different from the fundamental illustrated in Fig. 6.7(b), the dual gains might be generated without distortion. In WLC demonstration, we choose the

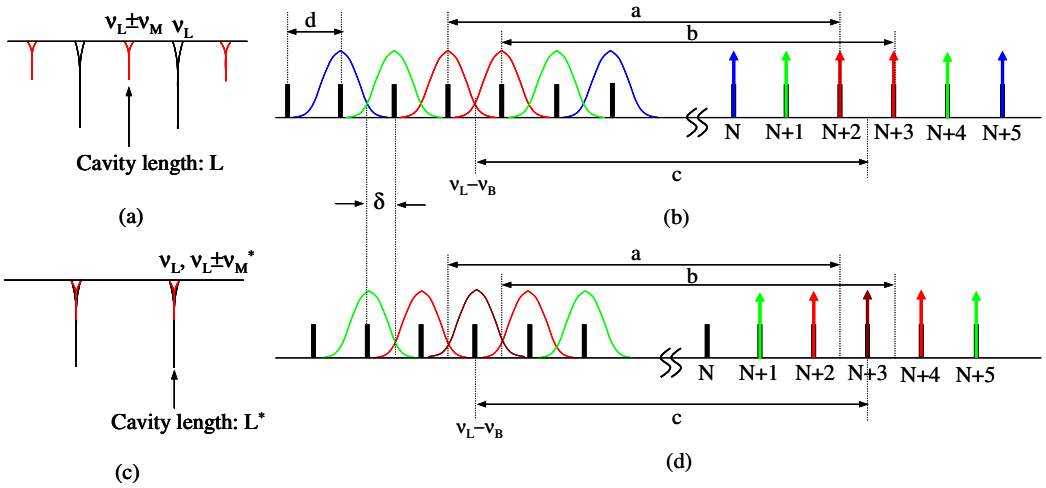

Fig. 6.7. (a) Pump resonance peaks. The EOM-1 outputs are resonant with the fiber ring cavity. The pump is modulated at $\nu_M = (2k+1)/2 \times FSR$. (b) Bi-frequency pumps (color arrows) are resonant with the cavity modes (black bars). The pumps produce dual gains which are downshifted from the pump spectra as much as by a, b and c, which are equal to ν_B=10.867GHz. The gains contain two modes at the center of each gain profile. For $\nu_M = FSR/2$, the resonant pumps (red arrows) produce the two gains (red). As increasing ν_M, the gain separations are expanded to 3FSR for $\nu_M = 3/2 \times FSR$ (green) and 5FSR for $\nu_M = 5/2 \times FSR$ (blue). (c) $\nu_M = k \times FSR$. (d) The gain separation is even number times FSR. For example, 2FSR for $\nu_M = FSR$ and 4FSR for $\nu_M = 2 \times FSR$. The single pump and gain are represented by the brown. The mode under the single gain profile agrees with that of the 1st order Brillouin laser presented in Fig. 5(a).

cavity mode nearest to the center of the two gains and scan the probe frequency around it. Negative dispersion is created in the middle of the separated gains. Note that the center of the dual gains ($\nu_L - \nu_B$) in Fig. 6.7(b) is separated from its neighboring cavity modes by FSR/2. Provided that the gain separation is sufficiently wider than FSR/2, the scanning range completely belongs to the spectral range of negative dispersion. As such, the probe experiences constant negative slope even though the probe scanning mode is displaced from $\nu_L - \nu_B$. By considering particular experimental constraints, we will choose the separation. Wavelength change due to the probe scanning is compensated by the negative dispersion slope associated with the group index. In our case in which the whole cavity exhibits dispersion in the presence of Brillouin pumps, the group index is close to zero to induce the WLC effect. The techniques presented in Fig. 6.7 make the gain profile support the cavity mode at the gain peak. Under such a mode arrangement, the single mode Brillouin-shifted wave (Stokes wave) is allowed to resonate and subsequently to be lasing. Since the probe can be embedded in the lasing signal, the Brillouin laser becomes the major source of background noises in WLC demonstration.

For WLC operation below the Brillouin lasing threshold, we could propose alternative FSR to fulfill $(N + 1/2)\mathrm{FSR} = \nu_B$. Fig. 6.8 illustrates the pumps and gains for the case of the cavity FSR of 17.4016MHz. Once the cavity length is fixed at L or L^*, the resonant pumps produce the gain profiles downshifted from the pump frequencies by as much as ν_B. Due to the given condition $(N + 1/2)\mathrm{FSR} = \nu_B$, the gain peaks appear in the middle of the two neighboring cavity modes illustrated in Fig. 6.8. Since the Brillouin linewidth is less than the FSR, the resonant modes are present sufficiently apart from the

gain peaks. Hence, we can achieve higher gain peaks than in the Brillouin resonant cavity, while staying below the Brillouin threshold. To demonstrate dual frequency Brillouin lasers, the pumps are modulated at ν_M=7.9932GHz that satisfies $\nu_M = (2k+1)/2 \times FSR$ with k=461. To keep below the Brillouin threshold, the cavity condition presented in Fig. 6.8 is useful in principle for WLC application. To evidently prove the generation of dual gains in the cavity, however, we use the cavity with FSR of 17.3262MHz so that $N \times FSR = \nu_B$. As such, we observe two different Brillouin lasing modes at the frequencies associated with dual gain peaks. Fig. 6.9(a) illustrates the EOM output observed by a photodetector (PD) at the port 3 of VC while scanning the ring cavity. Fig. 6.9(b) displays the dual frequency Brillouin lasers. According to the investigation in Fig. 6.7, the lasing frequencies correspond to the longitudinal cavity modes, $\nu_L - \nu_B \pm \nu_M$. From the equal intensity for the lasing peaks, one can determine that the two resonant pumps have the same intensity and produce the gains without causing noticeable cross-talks.

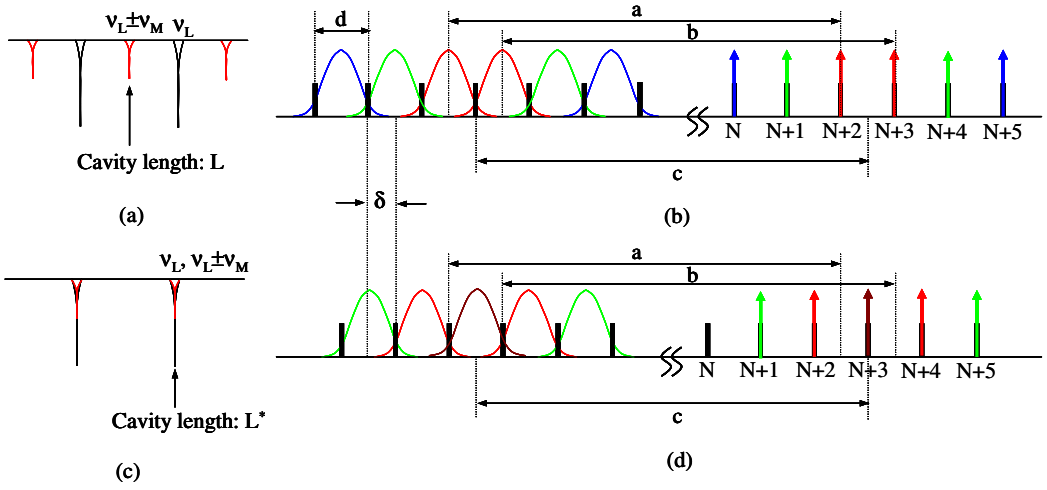

Fig. 6.8. FSR is modified equal to 17.4016MHz so that $(N+1/2)\text{FSR} = \nu_B$. (a) Pump resonance peaks for $\nu_M = (2k+1)/2 \times \text{FSR}$. (b) Gain profiles, pump spectra and cavity modes associated with the cavity lock on L. (c) $\nu_M = k \times \text{FSR}$. (d) Same diagram as (b) when $\nu_M = k \times \text{FSR}$.

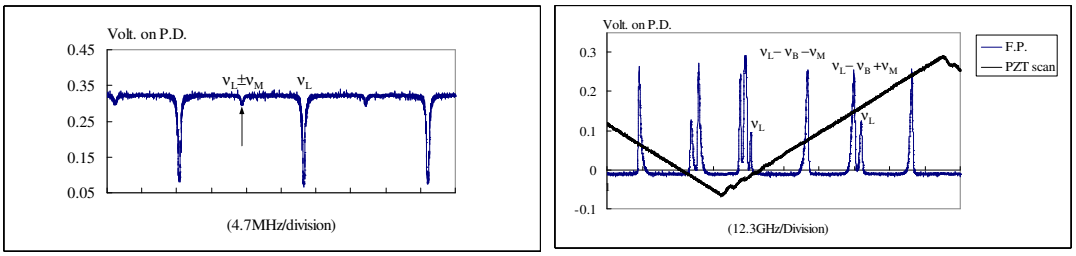

Fig. 6.9. (a) Pump resonance peaks. (b) Dual frequency Brillouin lasing. The two lasing peaks are separated by $2\nu_M$ (=17.326GHz).

CHAPTER VII

EXPERIMENT AND PARAMETER CONSTRAINTS

A. Motivation

Techniques to create negative dispersion over a limited frequency range have been performed through stimulated Brillouin scattering (SBS) [7], [8], [70]. In a so-called fast-light demonstration, optical pulse propagates through materials with an anomalous dispersion faster than in free space. Fast-light in optical fibers via SBS process has attracted much attention, due to availability in current communication and potential applications. In chapter V, data buffering systems based on fast-light technique in fibers was proposed to exceed the delay-bandwidth constraint encountered in conventional data buffers by means of slow light. Also, fast-light can be employed to enhance the rotational sensitivity of a passive resonator gyroscope [13] as well as to realize superluminal ring laser as a versatile hypersensitive sensor.

White Light Cavity (WLC) is fundamental to implement all these devices. WLC is a cavity that resonates over wider frequency range than in an ordinary cavity without the drop of a build-up factor. It has been implemented in a cavity filled with rubidium vapor where dual Raman gains were produced around the cavity resonance to achieve the fast-light condition ($n_g<1$) [15]. In chapter VI, primary analysis and experiments have been carried out to find out the proper free spectral range (FSR) as well as the optimal pump power level for WLC demonstration in fiber. FSR was adjusted to ensure

that the cavity mode exists at the center of dual Brillouin gains. The Brillouin pump power was controlled to maintain WLC below Brillouin lasing threshold.

In this chapter, we investigate physical constraints in realizing WLC via SBS in conventional single mode fibers. In the experiment, Brillouin pump is resonantly enhanced in the cavity. To create negative dispersion, either a single pump induces the probe depletion (Brillouin absorption) or bi-frequency pumps provide dual gains. In both cases, the cavity resonance is observed to be broadened by a very small amount due to small WLC effect. Numerical simulation confirms that under given experimental conditions the group index change can be small ($\Delta n_g = -0.01 \sim -0.03$). As such, negative dispersion is not sufficient to induce large WLC effect. Theoretical analysis shows that major restraints on WLC in conventional optical fibers are the requirements of extremely high pump power as well as the power damage threshold of optical elements. Key solution to these problems is higher Brillouin coefficient and low transmission loss fiber. To our knowledge, however, current fabrication technique can provide fibers with high Brillouin coefficient but higher transmission loss than conventional silica fibers. We propose an alternative fiber resonator to realize WLC with the high Brillouin coefficient but lossy fibers.

B. Theoretical background for WLC effect in fiber resonators

First, let us consider the optical field propagating an optical fiber resonator. Fig. 7.1 displays that a fiber ring resonator is built by a 2 by 2 coupler. Provided that the coupler is internally lossless, the complex field amplitudes are explained by the matrix

$$\begin{bmatrix} b_1 \\ b_2 \end{bmatrix} = \begin{bmatrix} \sqrt{1-K} & j\sqrt{K} \\ j\sqrt{K} & \sqrt{1-K} \end{bmatrix} \begin{bmatrix} a_1 \\ a_2 \end{bmatrix} \tag{7.1}$$

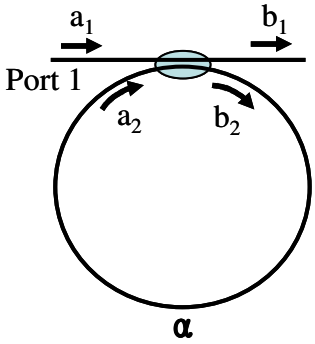

Fig. 7.1. Schematics of fiber ring resonator.

where K is the intensity coupling coefficient. Next, we include the internal loss in the resonator. The relationship between a_2 and b_2 is expressed in terms of the loss characteristics of the resonator α and the round trip phase shift θ

$$a_2 = \alpha e^{j\theta} b_2 \tag{7.2}$$

Using Eq.(7.1, 2), we can derive the power transmission ratio $|b_1/a_1|^2$ and the inserted power ratio into the resonator $|b_2/a_1|^2$ to the input $|a_1|^2$

$$\left|\frac{b_1}{a_1}\right|^2 = \frac{\alpha^2 + |t|^2 - 2\alpha|t|\cos\theta}{1 + \alpha^2|t|^2 - 2\alpha|t|\cos\theta} \tag{7.3a}$$

$$\left|\frac{b_2}{a_1}\right|^2 = \frac{1-|t|^2}{1 - 2\alpha|t|\cos\theta + \alpha^2|t|^2} \tag{7.3b}$$

where t is the complex amplitude transmission coefficient ($K + T = 1$, $T = |t|^2$). For simplicity, we will choose $|a_1|^2 = 1$. Next, consider θ in the presence of bi-frequency Brillouin pumps. The probe at frequency ω propagates the ring resonator whose

circumference is L. The phase shift resulting from the propagation is written as kL. The wave vector amplitude of the probe is represented by k. To observe the WLC effect, the bi-frequency pumps produce dual gains via SBS process in the fiber resonator and negative dispersion is created between the gains. For our case in which Brillouin gain medium length corresponds to L, the zero group index n_g=0 is required to achieve WLC condition [15]. The Brillouin dual gains α_{Br} and the phase β are given by

$$\alpha_{Br} = \frac{1}{2}\left[\frac{g_0 I_{P1}}{1+4(\nu-\nu_B-\Delta)^2/\Gamma_B{}^2} + \frac{g_0 I_{P2}}{1+4(\nu-\nu_B+\Delta)^2/\Gamma_B{}^2}\right] \tag{7.4}$$

$$\beta = \frac{g_0 I_{P1}(\nu-\nu_B-\Delta)/\Gamma_B}{1+4(\nu-\nu_B-\Delta)^2/\Gamma_B{}^2} + \frac{g_0 I_{P2}(\nu-\nu_B+\Delta)/\Gamma_B}{1+4(\nu-\nu_B+\Delta)^2/\Gamma_B{}^2} \tag{7.5}$$

where ν_B, g_0, and Γ_B are Brillouin frequency, gain coefficient, and linewidth, respectively. I_{P1} and I_{P2} are pump intensities per unit area. We consider the equal intensity so that I_{P1}= I_{P2}= I_P (W/m^2). 2Δ corresponds to the gain separation. The probe propagates the cavity where negative dispersion is created by SBS. The phase shift after one round trip can be written as $kL = n_f \omega L/c + \beta L$. n_f and c are the mean index of the fiber and speed of light, respectively. The loss characteristics of the resonator in the presence of the dual gains can be given by $\alpha\exp(\alpha_{Br}L)$. Let us call $\alpha\exp(\alpha_{Br}L)$ the modified gain. k is expressed by Taylor expansion around the cavity resonance frequency ω_0 as $k = k_0 + k_1(\omega-\omega_0) + k_2(\omega-\omega_0)^2 + k_3(\omega-\omega_0)^3$ where $k_0 = n_f\omega_0/c$, $k_1 = n_f/c + d\beta/d\omega\big|_{\omega_0}$ and $k_3 = (1/6)d^3\beta/d\omega^3\Big|_{\omega_0}$. Assuming $\omega_0 = \nu_B$, the second order term is k_2=0 due to the antisymmetric dispersion profile around ω_0. Finally, we substitute kL of Taylor expansion and $\alpha\exp(\alpha_{Br}L)$ into θ and α in Eq.(7.3a),

respectively, to obtain the transmitted power spectrum of the fiber-based WLC. In the experiment, we control the cavity length with a lock-in detection circuit so that the pumps resonate with the ring cavity. Eq.(7.3b) at resonance ($\theta=2m\pi$, m is integer) describes the relationship between the input pump intensity at port 1 and the resonant pump intensity inside the cavity. Suppose that the resonant pumps are non-depleted. The Brillouin pumps in the cavity is $I_j(1-|t|^2)/(1-\alpha|t|)^2$ where I_j (in Watt) is the individual pump power at port 1, (j=1 and j=2 denote 1st and 2nd pumps, respectively). Using the effective area A_{eff} (m^2) of a fiber, this yields $I_p= I/A_{eff}$ where $I = I_j(1-|t|^2)/(1-\alpha|t|)^2$. For the case in which a single pump produces Brillouin absorption to create negative dispersion, all the expressions and the arguments given above can be applied, provided that we change

$$\alpha_{Br} \rightarrow -1/2\, g_0 I_P/(1+4(\nu-\nu_B)^2/\Gamma_B{}^2)$$

$$\beta \rightarrow -(g_0 I_{Pl}(\nu-\nu_B)/\Gamma_B)/(1+4(\nu-\nu_B)^2/\Gamma_B{}^2)$$

Let us briefly estimate the WLC linewidth in comparison to an ordinary cavity. The frequency change of light causes the wave number to change. When the probe frequency is scanned, the wave number for the probe varies in the dispersive fiber resonator. We define the dephasing parameter φ resulting from the change of the wave number Δk as $\varphi = \Delta kLN$, where N is the number of round trips. For the ring resonator, $N = \gamma_0/(n_f L/c)$. γ_0 is a cavity life time in the absence of Brillouin pump. Its reciprocal corresponds to the cavity linewidth. $\Delta k = n_g \Delta\omega/c$ in the dispersive medium can be

easily derived from $dk/d\omega = n_g/c$ (n_g is group index). We ignore the additional dephasing resulting from higher order dispersions, i.e. $(d^n n/d\omega^n, n > 1)$. Inserting Δk and N into φ and recalling that $\varphi=2\pi$ where $\Delta\omega$ corresponds to the linewidth of the dispersive resonator leads us to $\Delta\omega_0 n_f/n_g = \Delta\omega$. It describes the relation between the WLC linewidth $\Delta\omega$ and the linewidth of the ordinary ring resonator $\Delta\omega_0 = 2\pi/\gamma_0$.

C. WLC demonstration under Brillouin single absorption (gain) condition

In the WLC experiment, we first employ Brillouin absorption spectrum.

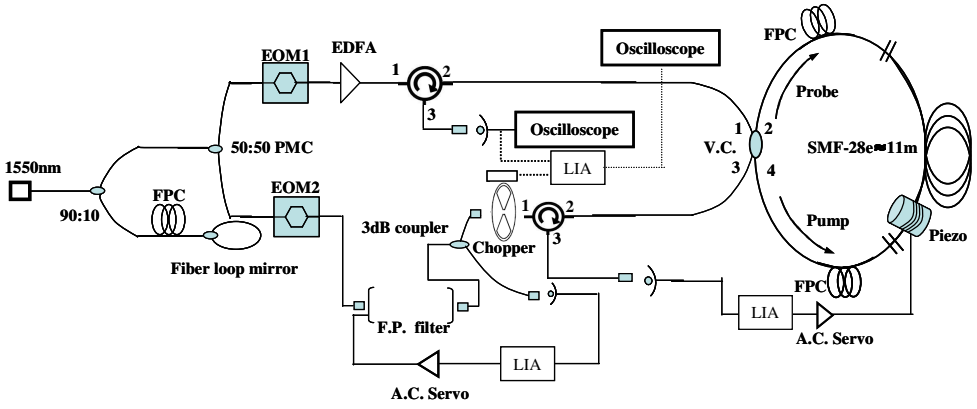

Fig. 7.2. Schematics of the experimental setup to observe the WLC effect. The components are: LIA, lock-in amplifier; EOM, electro-optic modulator; FPC, fiber polarization coupler; PMC, polarization maintaining coupler; and VC, variable coupler. The optical chopper combined with LIA will be used to capture the data presented in Fig. 7.7.

Fig. 7.2 displays the experimental set-up for WLC demonstration. We use the fiber ring cavity which is made of Corning SMF-28e with a free spectral range (FSR) of

17.32MHz. It is the same one as used in the previous chapter. The cavity length was adjusted so that one of the cavity modes corresponds to the Brillouin frequency ν_B. A fiber loop mirror [69] is used to stabilize the laser diode (LD) [71]. 50:50 polarization maintaining coupler (PMC) divides 90% of LD output. One is amplified by Er-doped fiber amplifier (EDFA) to provide a Brillouin single pump. A probe is modulated by EOM at the Brillouin frequency, which was previously measured as 10.867GHz. The fundamental is suppressed by adjusting the DC on EOM. The two sidebands are delivered to a Fabry-Perot (FP) spectrum filter. It is actively controlled by an AC servo and lock-in-amplifier (LIA) to filter one of the sidebands. The upper sideband $\nu_L+\nu_B$ is transmitted to interact with the Brillouin absorption for WLC demonstration. After FP filter is locked to $\nu_L+\nu_B$, the modulation frequency of the probe is slowly swept around ν_B by the amount $\Delta\nu$=3MHz to attain a resonance peak. We use the lower sideband $\nu_L-\nu_B$ to observe narrowing peaks due to normal dispersion in a single gain and compare them to the broadened cavity response with the upper sideband probe $\nu_L+\nu_B$.

Fig. 7.3(a) and (b) display experimental results and numerical simulations of the cavity resonance for different pump power. To obtain the probe transmission peak (black) without SBS inside the cavity, we modulate the probe at 7.0145GHz which is sufficiently separated from the Brillouin shift frequency of ν_B =10.867GHz. It provides a reference cavity transmission. As such, it propagates the cavity without interacting with the Brillouin pump while the cavity is locked to the pump resonance. The linewidth of the ordinary cavity is measured as 0.24MHz. We change the pump power below Brillouin threshold to avoid mixing the probe with Brillouin lasing noise. As increasing

pump power, we observe the broadening (narrowing) of the resonance peak from its interaction with Brillouin absorption (gain). The probe transmission is lower (higher) in the presence of Brillouin absorption (gain) than the reference transmission. We attribute such transmission variation to the induced (reduced) cavity internal loss by Brillouin absorption (gain). Fig. 7.3(b) displays the simulations for the cavity response associated with the experimental results. In chapter VI, we defined G factor as $-1/2\,g_0 I_P$ for absorption ($1/2\,g_0 I_P$ for gain). Note that in single absorption (gain) configuration, G implies absorption (gain) amplitude at Brillouin resonance $\nu=\nu_B$, It increases proportionally to the input pump intensity. In simulation, we choose the Gs associated with pump power, with fixed $\alpha=\sqrt{0.97}, t=\sqrt{0.945}$, to obtain consistency with the experimental data. The simulations confirm our interpretation of the transmission variation in the experiment. Recall the transmission as a function of α presented in Ref. 54. The transmission of the cavity without the pump is over-coupled ($\alpha>t$) so that the internally circulating field coupled into the output of the resonator $\sqrt{K}a_2$ is excessive compared to the transmitted field $\sqrt{T}a_1$. After applying a Brillouin pump, the probe of $\nu_L+\nu_B$ undergoes Brillouin loss such that $\sqrt{K}a_2$ reduces to $\sqrt{T}a_1$. As such, the cavity reaches critical coupling point ($\alpha\exp(\alpha_{Br}L)=t$) . $\sqrt{T}a_1$ completely interferes with $\sqrt{K}a_2$ at 2mW pump ($|G|=0.0005$) and thus the probe transmission vanishes at resonance. As the pump power becomes higher (4mW, $|G|=0.0015$, and

6mW, $|G| = 0.0018$), $\sqrt{K}a_2$ decreases again due to the augmented Brillouin loss, i.e. $\sqrt{T}a_1 > \sqrt{K}a_2$. The cavity is in under-coupled region ($\alpha \exp(\alpha_{Br} L) < t$) . Note that $|b_1|^2$

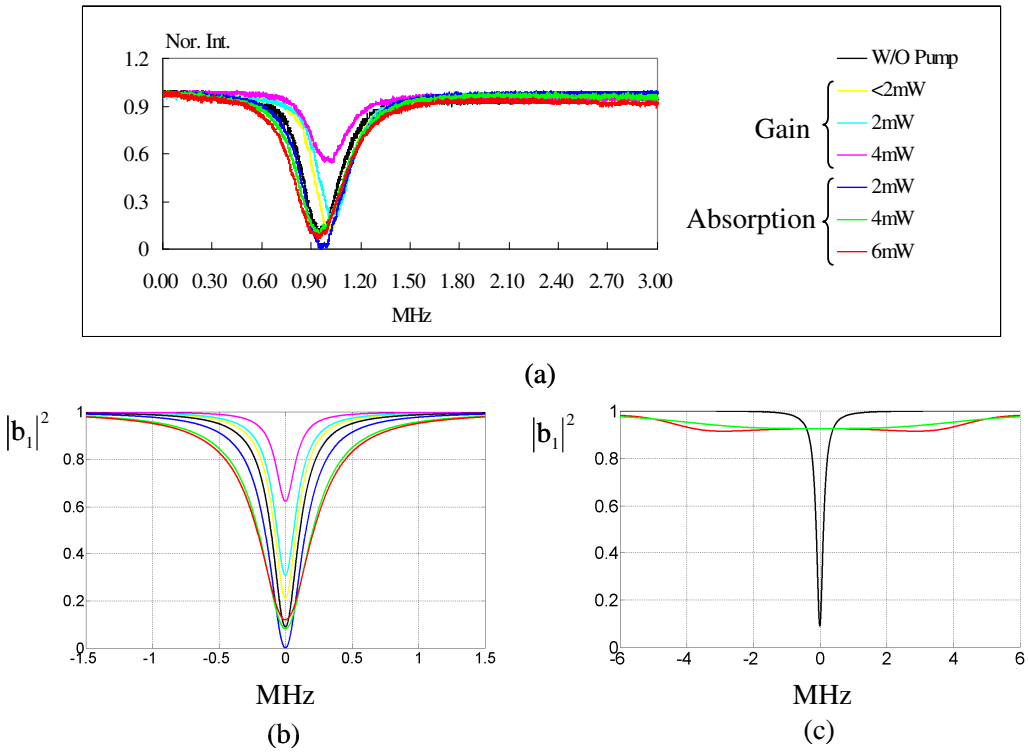

Fig. 7.3. (a) Experimental data of the cavity response for Brillouin absorption and gain with varying pump power. (b) Simulation results indicating close agreement with the experimental results. The colors of the peaks correspond to the colors as displayed in (a). G used in simulation and the calculated n_g associated with the particular G are: G=0.0002 and n_g =1.4538 for yellow; G=0.0003 and n_g =1.4557 for cyan; G=0.0005 and n_g=1.4595 for magenta; G=–0.0005 and n_g =1.4405 for blue; G=–0.0015 and n_g=1.4214 for green; G=–0.0018 and n_g=1.4156 for red. The negative (positive) G represents absorption (gain). (c) Black is a reference resonance peak without SBS. Red represents the cavity response at WLC condition (n_g=0, G=0.0759). Green is the result of a simulation with the condition that the cavity fiber is non-dispersive (i.e. n_g=n_f, n_f =1.45 for SMF-28e) but contains the induced loss as amount of Brillouin absorption.

corresponds to the resultant power after the interference. As the absorption is more induced, $|b_1|^2$ exhibits the value of 0.1 at resonance due to the residual $\sqrt{T}a_1$ after the destructive interference. When gain is introduced to the resonator, $\sqrt{K}a_2$ is increased by more than that in the absence of the pumps. As such, $|b_1|^2$ is raised compared to the reference after including the Brillouin gain. The gain amplitude at $\nu=\nu_B$ corresponds to $|G|$ for the absorption of the equal pump power. However, we also notice that in the numerical simulation for the particular power values, different $|G|$ s are chosen to provide consistency with the experimental results. For example, $|G|$=0.0005 and 0.0015 are for the gain and for the absorption at the pump of 2mW, respectively. In principle, the absolute amplitude of Brillouin gain peak corresponds to that of the absorption peak. However, the power of the resonant pump with the cavity depends on the stability of the cavity lock to fulfill the resonance. The achievable gain (absorption) amplitude at $\nu=\nu_B$ $|G|$ is determined by such resonant power inside the cavity. The gain amplitude ($|G|$=0.0015) is high compared to the absorption ($|G|$=0.0005) due to the more stable lock condition. Fig. 7.3 indicates that the resonance peak broadening (narrowing) is small with the allowed pump power below Brillouin lasing threshold due to small group index change. Furthermore, the absorption causes the linewidth to broaden. Therefore, it is difficult to conclude whether the broadening results from negative dispersion or from the induced Brillouin absorption. Before proceeding to the experimental demonstration, we simulate the WLC response displayed in Fig. 7.3(c). In the simulation, the WLC

exhibits finite linewidth due to the third order dephasing term k_3. Since $\sqrt{K}a_2$ is reduced by the extra loss of Brillouin absorption, the residual $\sqrt{T}a_1$ (T=0.945) after destructive interference contributes to the transmitted power $|b_1|^2$ associated with the resonance peak. As the pump power increases, therefore, $|b_1|^2$ approaches complete transmission at WLC condition. For comparison, we simulate $|b_1|^2$ (green) for the normal cavity ($n_g=n_f$) with loss corresponding to the induced Brillouin absorption in the presence of the WLC effect. WLC response is broader compared to the normal cavity (black), but the reduction in cavity buildup factor due to the additional Brillouin absorption loss makes the WLC effect undistinguishable from a non-dispersive cavity with equal loss (green).

For future experiment, we propose a diagnostic to observe the probe at $\nu_L+\nu_B$ embedded in the lasing background signal. We can use the optical filter elements such as fiber Bragg grating (FBG) and add it to port 3 of circulator 1 in Fig. 7.2. As such, we can filter the lasing light from the cavity resonance peak associated with Brillouin absorption probe $\nu_L+\nu_B$. We can increase the pump power regardless of Brillouin threshold restraint in order to attain $n_g=0$ for ideal WLC effect.

D. WLC demonstration under Brillouin gain doublet condition

Next, we used Brillouin dual gains to demonstrate WLC. The cavity length is controlled to resonate with bi-frequency pumps as presented in chapter VI. Fig. 7.4 displays the experimental setup. Light is modulated by EOM-1 to provide the bi-frequency pumps. The modulation frequency is chosen to be 17.32MHz. EOM-2

modulates the probe at ν_B. The fundamentals of the two EOMs are suppressed. The EOM-2 output is inserted into the fiber ring cavity through an optical circulator with the upper sideband $\nu_L+\nu_B$ remaining. Due to strong Brillouin absorption at $\nu_L+\nu_B$ inside the cavity, we expect that the anti-Stokes component $\nu_L+\nu_B$ of the probe is depleted and negligibly affects the Brillouin interaction between the pumps and the Stokes probe $\nu_L-\nu_B$.

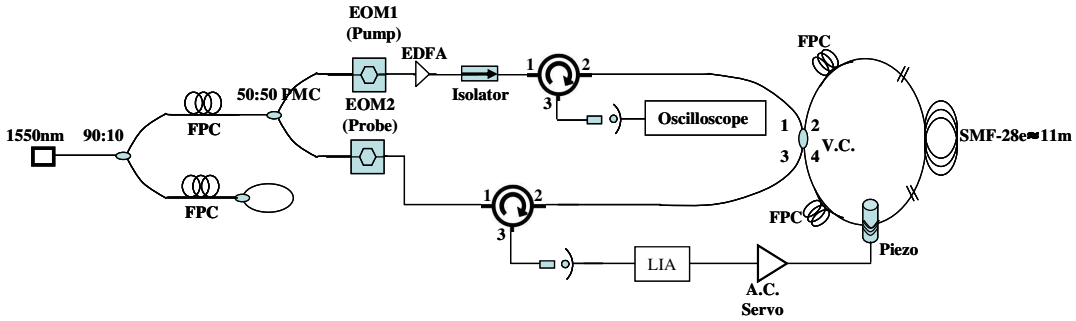

Fig. 7.4. Schematics of experimental setup for WLC with dual gains.

Fig. 7.5(a) and (b) illustrate the experimental results and numerical simulations. In the experiment, we monitored the pump resonance peak from port 3 of the variable coupler (VC) and adjusted the coupling ratio of VC to be the critical coupling point ($t=\alpha$), i.e. the transmitted power is zero at resonance [46]. To evaluate the cavity linewidth under no-gain condition, we measured the full width at half maximum (FWHM) of the pump resonanceto be 0.36MHz. In the critically coupled cavity, there is no transmitted light at resonance due to the perfect destructive interference between $\sqrt{T}a_1$ and $\sqrt{K}a_2$. In Fig. 7.5(a), the probe transmission peak confirms that the cavity in the presence of the 2mW pumps is near the critical point. Its linewidth is close to

0.36MHz. As pump power is increased, the probe experiences more gains such that the complete destruction of $|b_1|^2$ does not occur due to the excessive $\sqrt{K}a_2$. The resonant peaks approach the DC level of $\sqrt{T}a_1$. We increased the pump power until lasing occurred. The simulations in Fig. 7.5(b) confirm the effect of such =gain. To obtain agreement with the experimental data, we choose the G values according to pump power with fixed $t = \sqrt{0.93}$, and $\alpha = \sqrt{0.93}$.

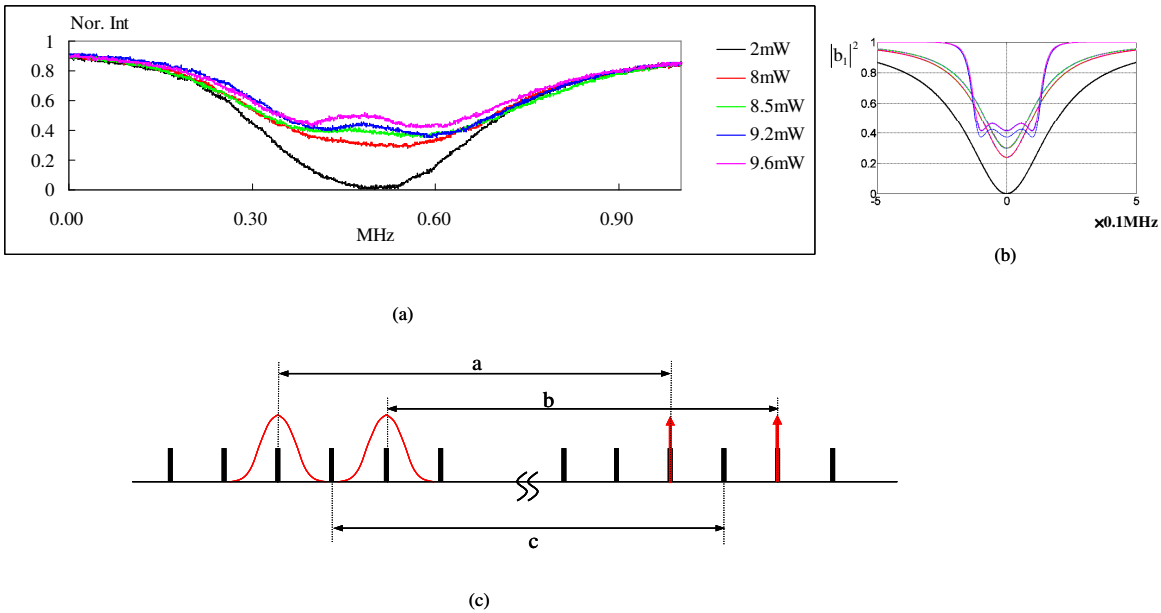

Fig. 7.5. (a) Pump power varies with the gain separation of 34.64MHz corresponding to 2×FSR. (b) Numerical simulations performed with G=0.001 (n_g=1.4499) for 2mW, G=0.013 (n_g=1.4338) for 8mW, G=0.0014 (n_g=1.4326) for 8.5mW, G=0.015 (n_g=1.4314) for 9.2mW, and G=0.0155 (n_g=1.4499) for 9.6mW. The group indexes are calculated from the G values. The colors of the peaks correspond to the power values indicated in (a). (c) Cavity modes (black bars), pump spectra (red arrows) and gain lines (red peaks). The frequencies a, b and c correspond to Brillouin shift frequency (10.867GHz). FSR is 17.32MHz.

For the pump of 9.2 and 9.6mW, the transmission peaks exhibit the horizontal area concomitant with distortion around resonance. We attribute this effect to mode competition between the Stokes probe and the residual anti-Stokes wave. In the simulation, we raised $d^3\beta/d\omega^3\Big|_{\omega_0}$ independently from $d\beta/d\omega\Big|_{\omega_0}$ to include the dephasing effect resulting from such a mode competition. Also, the experimental results show the peaks that are broadened in comparison to those in the simulations due to the depletion of the anti-Stokes probe. Fig. 7.5(c) illustrates the configurations of the cavity mode, dual gains and pump spectra associated with the experiment.

Again, we use the setup presented in Fig. 7.2 to block the upper sidebands $\nu_L+\nu_B$. In Fig. 7.6(a)~(d), we compare the transmission peaks under the dual gains to the peaks of the single gain. Also, the reference transmission without Brillouin interaction is displayed. The gain separation is 69.28MHz (=4FSR) as indicated in Fig. 7.6(e). First, the reference cavity linewidth was determined by scanning the probe around 7.0145GHz. In the gain doublet system, Brillouin gain compensates for the internal cavity loss so that the cavity response exhibits a narrow resonance peak. The linewidth is broadened by the WLC effect under dual gains as well. Since there is no experimental diagnostics to separate them, we observe the combination of these two effects. Fig. 7.6(a) indicates that for the case of 4mW bi-frequency pumps, the WLC effect is balanced by the linewidth narrowing. As a result, its linewidth is almost equal to the reference peak. As the pump power is increased, the WLC effect is small compared to the linewidth narrowing induced by the gains. With the dual pumps of 8 and 12 mW, we observed the

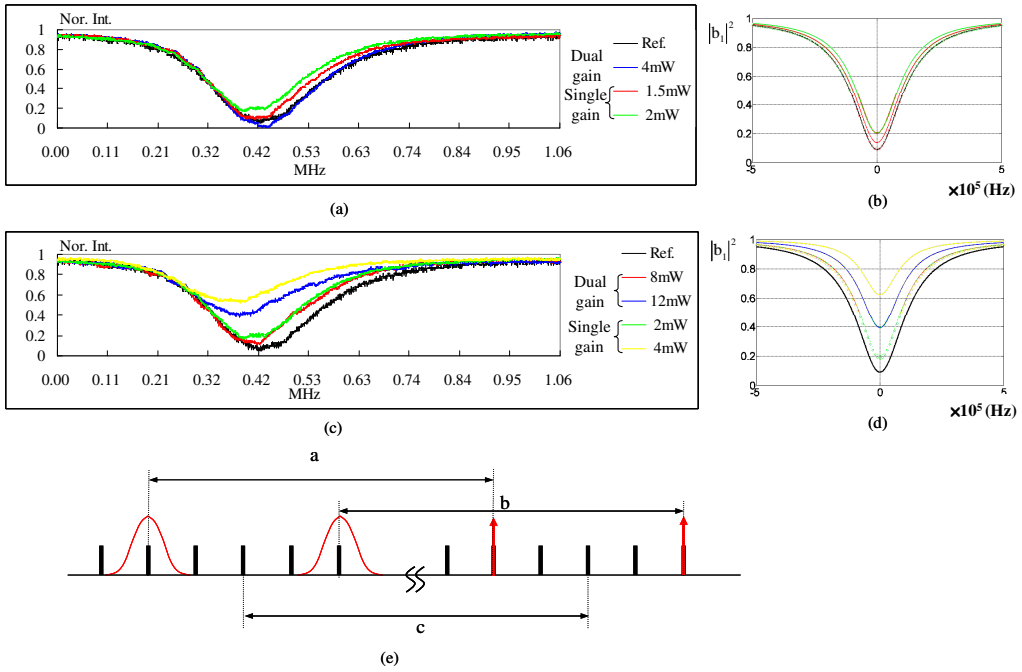

Fig. 7.6. (a) Experimental data comparing the ring cavity response for gain doublets to the cases for a single gain with varying pump power. The black peak is the response without Brillouin interaction. The anti-Stokes component $\nu_L+\nu_B$ of the probe is blocked by the FP spectrum filter. (b) Numerical simulations showing the agreement with the experimental data. The colors correspond to those of the graphs in (a). Blue dot represents the case of 4mW pump. The parameters for single gain are $G=1.9\times10^{-4}$, $n_g=1.4518$ (1.5mW), and $G=3.8\times10^{-4}$, $n_g=1.4536$ (2mW), and those for dual gains are $G=0.5\times10^{-4}$, $n_g=1.4481$ (4mW). (c) Experimental data showing the cavity response with the pump power different from (a). (d) Numerical simulations with parameters for a single gain are $G=3.8\times10^{-4}$, $n_g=1.4536$ (2mW) and $G=1.0\times10^{-3}$, $n_g=1.4595$ (4mW) and those for dual gains are $G=0.8\times10^{-2}$, $n_g=1.447$ (8mW) and $G=1.8\times10^{-2}$, $n_g=1.4433$ (12mW). (e) Configurations of cavity modes (black bars), pump spectra (red arrows) and gains (red peaks). The frequencies a, b and c correspond to Brillouin shift frequency (10.867GHz). For the comparison of linewidths in (a) and (c), we moved the data to align the rising portions of the peaks. In the experiment, the resonances (minimum transmission) were observed at the same frequency as the reference.

transmission peaks narrower than the reference. However, we notice that in the case of the single pump, there is additional linewidth narrowing caused by normal dispersion. Therefore, it can be seen that the probe transmission of the 4 mW dual pump is broader than that of the 1.5mW single pump, and that the transmission of the 8mW dual pump is also broader than that of the 2mW single pump.

We revised the cavity length so that FSR obeys $\mathrm{FSR}(N+1/2)=\nu_B$ to ascertain that the gain peaks do not support any cavity mode. With this design, we can prevent the Brillouin-shifted wave (Stokes wave) from resonating simultaneously. As such, Brillouin lasing threshold grows higher than in the previous cases. The new FSR was measured as 17.4016MHz. The gain separation was chosen to be 3×FSR (52.2MHz). We increased the pump power to the level where Brillouin lasing occurs at modes close to the gain peaks. However, we stopped the increase before the probe mode started lasing. Again, we used the setup displayed in Fig. 7.2. The optical chopper is added to separate the probe from the lasing signal of the gain peaks. To evaluate the cavity linewidth without the SBS process, we scanned the probe around 8.7008GHz which is sufficiently separated from ν_B (10.867GHz). The lasing occurs at the cavity mode close to $\nu_L-\nu_B$ within the Brillouin gain profile.

Fig. 7.7 illustrates the experimental data and the configurations of cavity modes, pump spectra, and dual gain peaks. The cavity response at 14mW becomes broad due to the small amount of the WLC effect.

So far, from the simulations and experimental results, we found that the WLC effect under given experimental parameters is small due to the small group index change

($\Delta n_g = -0.01 \sim -0.03$, i.e. $n_g \approx n_f$) . In the next chapter, we will consider the experimental constraints in realizing a large WLC effect. We will propose the experimental setup to exhibit a noticeable WLC effect under particular constraints.

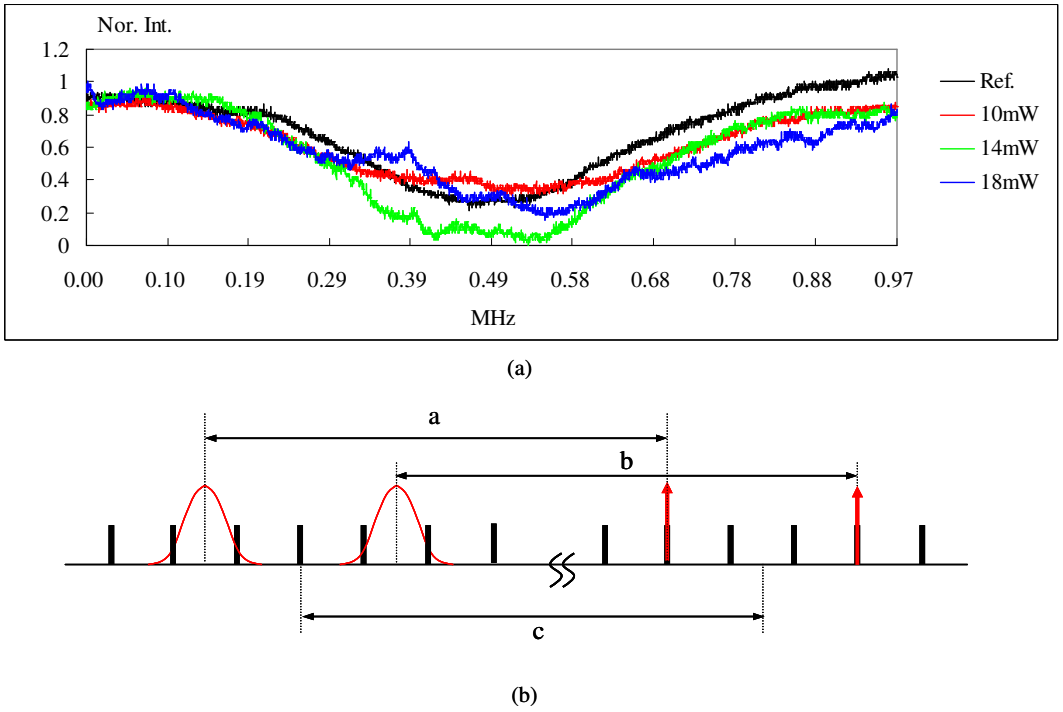

Fig. 7.7. (a) Probe transmission profiles showing a small WLC effect. It is separated by the optical chopper from the lasing signal. The lasing occurs at the modes close to the gain peaks. When the pump power reaches 18mW, the probe mode starts lasing as well. (b) FSR (=17.4016MHz) is adjusted to be larger than the gain bandwidth Γ_B. The gain peaks are shifted from the pump spectra by amount ν_B. According to $\mathrm{FSR}(N+1/2)=\nu_B$, the peaks are located at the center of the two neighboring cavity modes. The frequencies a, b, and c are equal to ν_B (10.867GHz) in magnitude.

E. Investigation of experimental constraints in realizing WLC based on SBS in conventional optical fibers

To create a noticeable WLC effect, we investigate necessary parameters to induce n_g=0.1, 0.725 and 1.1. According to the relationship $\Delta\omega_0 n_f / n_g = \Delta\omega$, we can anticipate that the WLC linewidth will broaden by a factor of approximately 14.5 for n_g=0.1, 2 for n_g =0.725 and 1.32 for n_g =1.1 in comparison to the normal cavity. For the investigation, we choose FSR to yield $\mathrm{FSR}(N+1/2)=\nu_B$. The gain separation is chosen to correspond to FSR so that a single longitudinal cavity mode is located at the center of the two gains. To observe the WLC effect, we scan the probe frequency around such a mode. We inspect allowable FSRs of WLC for the given n_g to keep below Brillouin threshold at the probe scanning mode. First, let us consider the gain that the probe experiences during one round trip in the ring cavity, the so-called gain per pass. The cavity resonance frequency ν_0 in the middle of two gains is equal to ν_B due to the cavity design rule $\mathrm{FSR}(N+1/2)=\nu_B$ as well as the proper gain separation. In the double gains, Eq.(7.5) indicates that at resonance (i.e. ν_0=ν_B) the probe experiences the exponential Brillouin gain of $\alpha_{Br(\nu=\nu_0)} = 2G/(1+4\Delta^2/\Gamma_B{}^2)$. The probe is scanned around ν_B within the spectral region where negative dispersion occurs. To observe the linewidth broadening due to the WLC effect, the scan range is required to be larger than FWHM of the reference cavity. We consider the cases in which the cavity FSR is almost equal to the width measured at the bottom of the gain profile, i.e. ~$2\Gamma_B$. Due to high Q of fiber cavities, the cavity FWHM is less than FSR by a factor of 10~100. As such, FWHM

approximately corresponds to $0.02\Gamma_B$ ~$0.2\Gamma_B$. The minimum scan range is substantially less than $2\Gamma_B$ and thus most of such scan region exhibits the Brillouin gain close to $\alpha_{Br(\nu=\nu_0)}$. Therefore, we can assume that the probe feels the constant gain $\alpha_{Br(\nu=\nu_0)}$ while scanning around ν_0. Before proceeding to find gain per pass for the probe, let us discuss the effective cavity length (L_{eff}). When we introduce significant internal cavity loss in numerical simulation, L_{eff} is no longer equal to L. Note that α is associated with the loss characteristic for our case. As such, L_{eff} in Ref. 56, 64, 68, 72 is redefined as $L_{eff} = -L(1-\alpha)/(\ln\alpha)$ in terms of the cavity length. It leads to the exponential gain per pass for the probe $\alpha_{Br(\nu=\nu_0)}L_{eff}$. Using L_{eff}, the modified gain is changed to $\alpha\exp(\alpha_{Br}L_{eff})$. According to $a_2 = \alpha\exp(\alpha_{Br(\nu=\nu_0)}L_{eff})e^{i\theta}b_2$, $\alpha\exp(\alpha_{Br(\nu=\nu_0)}L_{eff})$ represents the round trip gain. Sufficient pump power can allow values of $\alpha\exp(\alpha_{Br(\nu=\nu_0)}L_{eff})$ to be larger than 1. At $\alpha\exp(\alpha_{Br(\nu=\nu_0)}L_{eff}) = 1$, the induced Brillouin gain completely compensates for the internal cavity loss and thus the probe reaches the lasing threshold. As we are interested in observing WLC effect under Brillouin threshold, the cavity gain factor is $\alpha\exp(\alpha_{Br(\nu=\nu_0)}L_{eff}) < 1$. It leads to the condition below Brillouin threshold at the probe scanning mode i.e. $\alpha_{Br(\nu=\nu_0)}L_{eff} < -\ln(\alpha)$. Define $d\beta/d\omega|_{\omega_0} = 2G(d\gamma/d\omega|_{\omega_0})$ where γ is the sum of two remaining Lorentzians after factoring out $G = g_0I_P/2$ from β. Using $k_1 = n_f/c + d\beta/d\omega|_{\omega_0} = n_g/c$ together with the new definition, we can express $G = (n_g - n_f)/(2c\gamma')$ where $\gamma' = d\gamma/d\omega|_{\omega_0}$ is negative. It

is instructive to graphically compare $-\ln(\alpha)$ to $\alpha_{Br(\nu=\nu_0)}L_{eff}$ for n_g=0.1, 0.725, and 1.1.

Fig. 7.8 illustrates the lasing threshold $-\ln(\alpha)$ and the exponential gain per pass $\alpha_{Br(\nu=\nu_0)}L_{eff}$ as the function of FSR. For illustration, we consider different internal cavity loss so that α=0.955, 0.911 and 0.855. We choose t=0.955 and n_f=1.45. Based on the previous measurement in chapter VI, we use Γ_B=10MHz. Recall that the gain separation 2Δ is equal to FSR.

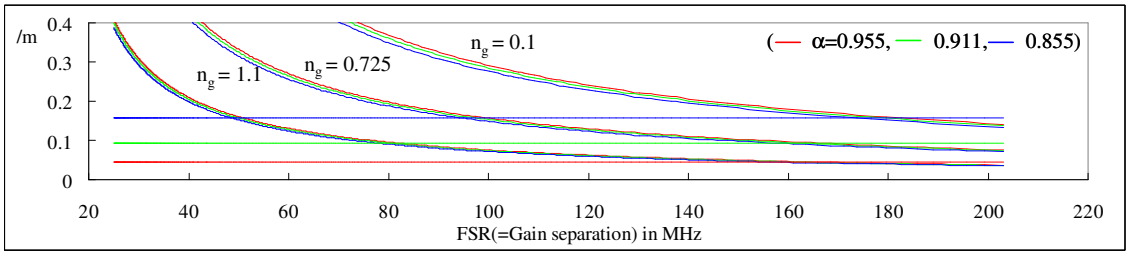

Fig. 7.8. For each n_g, the curves represent $\alpha_{Br(\nu=\nu_0)}L_{eff}$ associated with different α values. The straight lines correspond to $-\ln(\alpha)$. The operational FSR is FSR>176MHz for n_g=0.1 and α=0.855, FSR>95MHz for n_g=0.725 and α=0.855, FSR>160MHz for n_g=0.725 and α=0.911, FSR>48MHz for n_g=1.1 and α=0.855, FSR>80MHz for n_g=1.1 and α=0.911, and FSR>180MHz for n_g=1.1 and α=0.955. There are no available operational FSRs for the case of α=0.955 or α=0.911 for n_g=0.1, and α=0.955 for n_g=0.725.

Due to the low lasing threshold in high Q resonator ($\alpha\approx1$), $-\ln(\alpha)$ decreases as we withdraw the cavity loss i.e. $\alpha\rightarrow1$. To understand the behavior of $\alpha_{Br(\nu=\nu_0)}L_{eff}$, note that G should be essentially increased to induce larger group index change Δn_g. The gain $\alpha_{Br(\nu=\nu_0)}$ seen by the probe increases proportionally to G and thus small n_g (large

Δn_g) requires higher $\alpha_{Br(\nu=\nu_0)}L_{eff}$. Since the inclusion of the cavity loss reduces L_{eff}, $\alpha_{Br(\nu=\nu_0)}L_{eff}$ for the equal n_g increases as $\alpha \rightarrow 1$. The cavity mode for the probe should stay below the lasing threshold. For WLC demonstration, we can employ the cavity FSR to fulfill the condition $\alpha_{Br(\nu=\nu_0)}L < -\ln(\alpha)$. Let us call the available FSR as the operational FSR. For example, the operational FSR is FSR>176MHz for n_g=0.1, α=0.855. Since the reduction of n_g entails the addition of $\alpha_{Br(\nu=\nu_0)}L_{eff}$, we can note that for n_g=0.1 with α=0.955 or α=0.911, $\alpha_{Br(\nu=\nu_0)}L_{eff}$ is higher than the lasing threshold over all FSRs of interest.

Fig. 7.9 illustrates G for n_g=0.1, 0.725, and 1.1. To understand the behavior of G, we discuss n_g together with the negative dispersion slope as well as gain separation. Negative dispersion slope becomes large to decrease the group index. Fig7.9 suggests that either larger G for constant gain separation or narrow gain separation for constant G leads to the small n_g. Fig. 7.10 displays the input pump power I_j for the cavities of different α values associated with the internal loss. Using Brillouin coefficient g_0=0.7682×10^{-11} m/W for conventional silica fibers [68], we first find the pump intensity per unit area I_p inside the cavity. Consider briefly the polarization property of the fiber. Taking the polarization into account, G can be rewritten as $1/2 g_0 I_P \kappa$ where $\kappa = 1$ if the polarization is maintained or otherwise 0. While the probe propagates inside the cavity, its polarization direction is properly adjusted to correspond to the pumps. Hence, the previous definition $G = 1/2 g_0 I_P$ (i.e. $\kappa = 1$) is suitable for our cases. To demonstrate

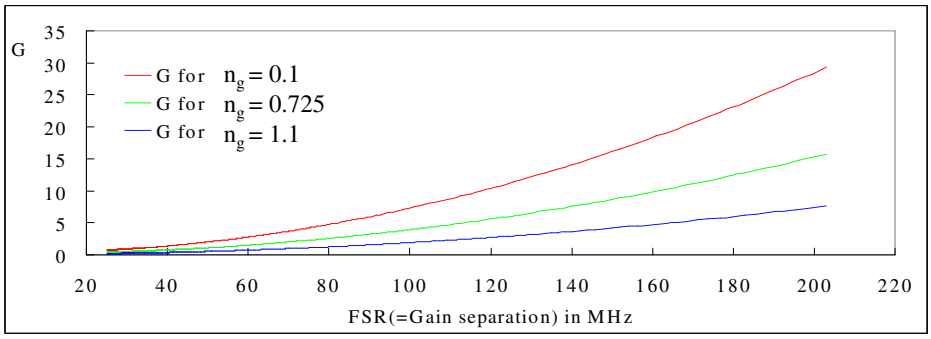

Fig. 7.9. Exponential Brillouin gain peak amplitudes for different n_g values.

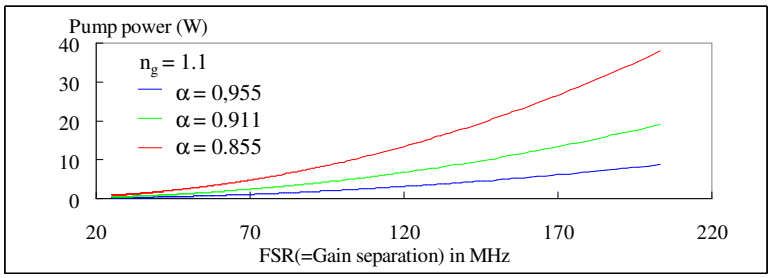

(a)

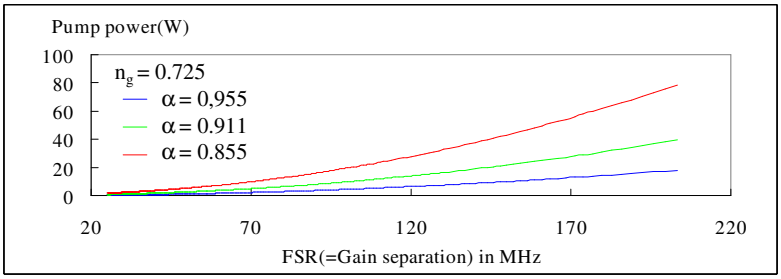

(b)

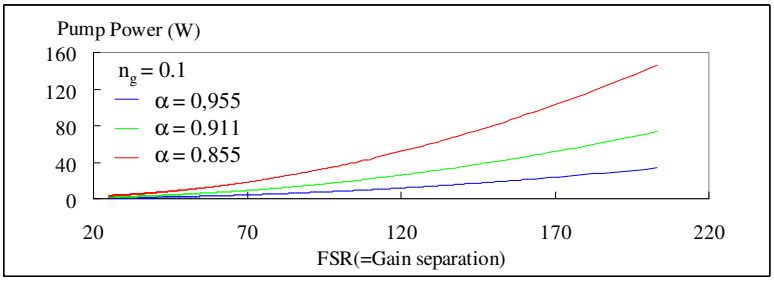

(c)

Fig. 7.10. Pump power being required to obtain n_g. Note the power within the operational FSR mentioned in Fig. 7.8.

WLC, we control the cavity length to force Brillouin pumps to be resonant with the cavity. According to the pump build-up factor $\eta = (1-|t|^2)/(1-\alpha|t|)^2$, I_j is related to I_p by $I_j = I_p A_{eff}/\eta$. We choose $A_{eff}= 5\times10^{-11}$ m^2 for silica single mode fibers [68]. Consider I_j within the operational FSR. To achieve the particular n_g in the operational FSR, I_j is essentially needed higher than the maximum power achievable from commercial EDFAs as well as the power limitation imposed on the fiber optic elements such as circulators and couplers. Even though we could experimentally increase I_j to such a high power level, G stops increasing due to Brillouin gain saturation. In the previous Brillouin characteristics measurement, the fiber used for our cavity exhibited that it was saturated at G=0.04. Insertion of I_j into G yields $G = (1/2g_0)(I_j\eta/A_{eff})$. According to the equation for G, the saturation problem is overcome by using fibers of high Brillouin coefficient and small effective area. Tellurite fiber (g_0=1.6986×10^{-10} m/W, A_{eff}= 0.6967×10^{-11} m^2) or As_2Se_3 chalchogenide fiber (g_0=6.08×10^{-9} m/W, A_{eff}= 3.9×10^{-11} m^2) has 20~800 times larger g_0 and smaller A_{eff} than conventional fibers. However, their transmission loss is major drawback when the cavity is controlled to achieve the pump resonance. For example, we built a 6m ring resonator which was composed of 4m tellurite fiber and 2m SMF28e. While scanning the cavity, the pumps were coupled into the cavity to obtain the resonance peak. As it is reported to exhibit large loss at low input power [56], the coupled light $\sqrt{K}a_2$ was completely absorbed before one round trip. We could not observe the resonance peaks but only the transmitted field $\sqrt{T}a_1$.

F. Alternative experimental set-up for future works

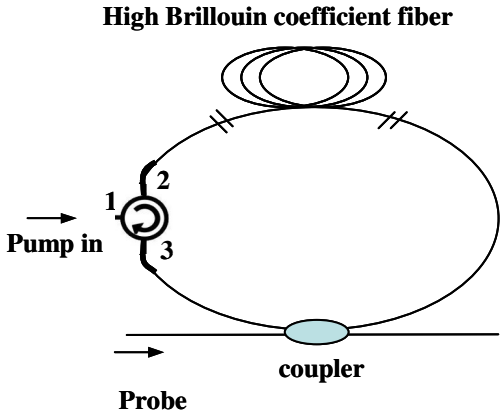

Fig. 7.11. Schematics of proposed setup for WLC demonstration.

Alternatively, we propose a WLC experimental set-up illustrated in Fig. 7.11. A fiber ring resonator is built by a coupler spliced with the high Brillouin coefficient fibers. Low loss optical circulator is used to insert Brillouin pumps into the ring cavity [73], [74]. The pumps propagate without resonating with the cavity and thus the transmission loss problem is avoided due to no requirement of the cavity length control. However, we need more input power for this cavity than the resonantly enhanced pump cavity. The high power EDFA compensates for it. Furthermore, high g_0 fibers allow us to drop the input power level which is required to achieve sufficient Δn_g for large WLC effect.

CHAPTER VIII

CONCLUSION

We have demonstrated superluminal light propagation using the dual-frequency pumped photorefractive crystal. The results prove that the crystal is a promising candidate for the design of a White light Cavity (WLC). The desired bandwidth for the LIGO applications is only a few kHz. The bandwidth of the crystal used in this experiment was on the order of 1Hz, which is too narrow for such an application. However, the bandwidth can be increased up to a few KHz by using a fast response crystal such as an SPS.

We developed a theoretical model for the WLC behavior of an active resonator: a superluminal ring laser. Since the laser operates under the condition where the gain per pass balances the loss per pass, the conventional model for a white light cavity did not apply. However, we showed that if the gain profile is flat over the region of interest, with a dip in the middle, the lasing mode centered at the dip behaves like WLC, with its frequency becoming highly sensitive to mirror displacement or rotation. The enhancement factor was calculated as high as 10^7, comparable to what is achievable in a passive cavity. We also presented a physical interpretation of this behavior in terms of an effective Kramers-Kroenig relation, and showed that the process works with both homogeneously or inhomogeneously broadened gain media.

Next we have proposed that WLC can be used to design an optical pulse delay system. The bandwidth $\Delta\nu$ ($1/t_0$=29MHz) of a Gaussian data pulse $\exp(-t^2/t_0^2)$ was

broader than the FWHM (2.9MHz) of the cavities in the absence of the WLC effect. However, the pulse was successfully loaded to the system without distortion while the WLC effect is on. It was delayed being compared to a free space propagating reference much larger than the input pulse duration. Our system bandwidth corresponded to the half of the WLC linewidth. The system bandwidth can be easily expanded broader than the data pulse spectrum. Furthermore, the system delay time is adjustable by switching WLC effect. Regardless of $\Delta\nu_{system}$, the delay time can be augmented as much as required. This represents the improvement over standard optical delay devices and is an important step toward solving the delay time-bandwidth problem in such devices.

For more practical application to the current fiber optic communication systems, we proposed a theoretical model of a fiber-based data buffering system. Delay time was determined by the number of round trips inside the intermediate loop and the fiber length of the loop. We could lengthen the fiber of the loop so that the increased traveling time causes more delay time per one round trip. Hence, the number of the round trips in the loop which is required for a specific time delay was decreased. It means that the number of crossing through the couplers decreases to obtain same delay and thus a data pulse can be delayed with the negligible coupling loss. The bandwidth of a Gaussian pulse was 10 times the full width at half maximum of the ring resonator. However, in the presence of the WLC effect, the pulse spectrum belonged to the region of the constant amplitude ($|H_{1r}|=1$) for the WLC effect induced fiber resonator. The input pulse was loaded into the loop without distortion. 2μs pulse was delayed by using the 6.7km fiber loop. The delay time was in the time scale of 10^{-4} second retaining its original shape. To increase

achievable WLC linewidth, we also proposed the scheme to create negative dispersion over the spectral range corresponding to multiple times Brillouin frequency. It was possible to improve the dynamic range of our system. Unlike the previous system in the version of Fabry-Perot, this fiber-based buffering system can be realized by a simple configuration with the expandable dynamic range.

We have demonstrated dual pumps locking to different longitudinal modes of a fiber ring cavity. For the application of the ring cavity to WLC demonstration, the cavity FSR was chosen to satisfy $(N+1/2)FSR = \nu_B$ or $N \times FSR = \nu_B$. For both cases, various pump separations were considered to ensure that there was an available cavity mode at the center of two Brillouin gains. Also, the cavity mode existed at the frequency which is downshifted as much as ν_B from the center of the two pumps spectrum. The corresponding dual gains were characterized indirectly by observing the production of two Brillouin lasing modes at frequencies corresponding to the gain peaks. The resulting two lasing peaks exhibited essentially the equal intensity. It indicates that the presence of two resonant pumps do not cause any noticeable cross-talks. When the input intensity of a single frequency pump was increased beyond the secondary threshold, we observed first, second and third order Brillouin lasing simultaneously. We inspected the configurations of the modes, single gain and pump spectrums. It confirmed that the lasing signal was a single mode. The information obtained from these observations can be used to determine the optimal combination of power level in each of the two pumps as well as the proper choice for FSR of WLC to operate WLC below Brillouin lasing threshold.

Next, we have investigated the feasibility of realizing WLC using SBS, under two different configurations. In one case, we used a single frequency Brillouin pump resonantly enhanced in the cavity. The single frequency probe counterpropagated and was tuned to be resonant at a different longitudinal mode of the cavity. The cavity FSRs were chosen to ensure that the probe experiences depletion due to the SBS process of the pump. The probe was modulated at 7.0145GHz which is sufficiently separated from Brillouin shift frequency (ν_B =10.867GHz). It was scanned to characterize the cavity linewidth without Brillouin interaction in the presence of the pump. When the probe was scanned around ν_B, the observed linewidth was broadened. The broadening in this case was due to a combination of the WLC effect, and the pump induced depletion. Experimentally, it is impossible to separate out these two effects. We developed an analytical model, and used it to simulate numerically the probe transmission profile under conditions that match the experiment closely. The simulation showed that only a very small fraction of the broadening is due to the WLC effect. An analysis of the theoretical model also reveals that this is a fundamental constraint for such Brillouin absorption induced cavity. In the second case, we used a pump with two frequency components, each locked to a cavity mode. The counterpropagating, single frequency probe was also resonant, at a different cavity mode. The various gain separations as well as FSR were chosen to ensure that the probe frequency was tuned to the center of the two gains. During the probe scanning around ν_B, the probe transmission profile was seen to be broadened by a very small amount, due to the WLC effect. Analytical model and simulation confirmed the conclusion that the WLC effect under the experimental

parameters is very small, and consistent with our experimental observation. In order to identify optimal conditions for observing a large WLC effect, we extended our model to allow for an arbitrary combination of bare cavity loss, free spectral range, pump power, and Brillouin coefficient. The results show that, given the properties of the fiber we are using, the key limitations are due to the damage thresholds of the various components (such as couplers and circulators), as well as the maximum power available from commercial EDFAs. Alternatively, these constraints can be overcome by using a fiber with the Brillouin coefficient that is significantly higher than that of the fiber we are using, without a significant transmission loss.

Future efforts at realizing a high bandwidth WLC using a fiber resonator therefore have to be directed towards overcoming these constraints. For future work, we suggested the alternative experimental setup to realize WLC. High Brillouin coefficient fiber together with commercial high power EDFA can possibly provide enough pump power to induce large WLC effect. Low insertion loss optical element is required for the setup, as well.

REFERENCES

[1] L.V. Hau, S.E. Harris, Z. Dutton and C. H. Behroozi, "Light speed reduction to 17 meters per second in an ultracold atomic gas," *Nature* vol. 397, pp. 594~598, 1999.

[2] D.F. Philips, A. Fleischhauer, A. Mair, and R.L. Walsworth, and M.D. Lukin, "Storage of light in atomic vapor," *Phys. Rev. Lett.* vol. 86, pp. 783~787, 2001.

[3] A.V. Turukhin,V. S. Sudarshanam, M. S. Shahriar, J. A. Musser, B. S. Ham and P. R. Hemmer, "Observation of ultraslow and stored light pulses in a solid," *Phys. Rev. Lett.* vol. 88, No.2, pp. 023602-1~023602-4, 2002.

[4] L.J. Wang, A. Kuzmich and A. Dogariu, "Gain-assisted superluminal light propagation," *Nature,* vol. 406, pp. 277~279, 2000.

[5] E. Podivilov, B. Sturman, A. Shumelyuk and S. Odoulov, "Light pulse slowing down up to 0.025cm/s by photorefractive two-wave coupling," *Phys. Rev. Lett.* vol. 91, pp. 083902-1~083902-4, 2003.

[6] Y. Qkawachi, M.S. Bigelow, J.E. Sharping, Z. Zhu, and A. Schweinsberg "Tunable all-optical delays via Brillouin slow light in an optical fiber," *Phys. Rev. Lett.* vol. 94, pp. 153902-1~153902-4, 2005.

[7] K.Y. Song, K.S. Abedin and K. Hotate, "Gain-assisted superluminal propagation in tellurite glass fiber based on stimulated Brillouin scattering," *Opt. Exp.* vol. 16, pp. 225~230, 2008.

[8] K.Y. Song, M.G. Herráez and L. Thévenaz, "Observation of pulse delaying and advancement in optical fibers using stimulated Brillouin scattering," *Opt. Exp.* vol. 12, pp. 82~88, 2005.

[9] K.Y. Song, K.S. Abedin, K. Hotate, M.G. Herráez and L. Thévenaz, "Highly efficient Brillouin slow and fast light using As_2Se_3 chalcogenide fiber," *Opt. Exp.* vol. 14, pp. 5860~5869, 2006.

[10] A.M. Steinberg and R.Y. Chiao, "Dispersionless, highly superluminal propagation in a medium with a gain doublet," *Phys. Rev. A,* vol.49, pp. 2071~2078, 1994.

[11] E. Hecht, *Optics,* 4th Ed. Munich, Germany, Addison-Wesley, 2002.

[12] R.W. Boyd and D.J. Gauthier, "Slow and fast light" in *Progress in Optics,* vol. 43, edited by E. Wolf, Amsterdam, The Netherlands: Elsevier, Chap. 6, pp. 497~517, 2002.

[13] M.S. Shahriar, G.S. Pati, R. Tripathi, V. Gopal, M. Messall and K. Salit, "Ultrahigh precision absolute and relative rotation sensing using fast and slow light," *Phys. Rev. A,* vol. 75, pp. 053807-1~053807-4, May 2007.

[14] G.S. Pati, M. Messall, K. Salit, and M.S. Shahriar, "Demonstration of tunable displacement-measurement-sensitivity using variable group index in a ring resonator," *Opt. Comm.* vol. 281 (19), pp.4931~4935, 2008.

[15] G.S. Pati, M. Messall, K. Salit, and M.S. Shahriar, "Demonstration of a tunable-bandwidth white light interferometer using anomalous dispersion in atomic vapor," *Phys. Rev. Lett.* vol. 99, pp. 133601-1~133601-4, 2007.

[16] M. Salit, G.S. Pati, K. Salit, and M.S. Shahriar, "Fast-light for astrophysics: super-sensitive gyroscopes and gravitational wave detectors," *J. of Modern Optics,* vol. 54, Issue 16 & 17, pp. 2425~2440, 2007.

[17] M.S. Shahriar and M. Salit, "Application of fast Light in gravitational wave detection with interferometers and resonators," *J. of Modern Optics,* vol. 55, Nos. 19-20, 10-20, pp. 3133~31478 Nov. 2008.

[18] M.S. Shahriar and M. Salit, "A fast-light enhanced zero-area sagnac ring laser gravitational wave detector," to be submitted to *Phys. Rev. Letts.* http://lapt.eecs.northwestern.edu/preprints/FE-ZASRL-GWD.pdf, Jan. 28th, 2009.

[19] M. Salit and M.S. Shahriar, "Enhancement of sensitivity-bandwidth product of interferometric gravitational wave detectors using white light cavities," submitted to *Phys. Rev. A*.

[20] S. Wise V. Quetschke, A. J. Deshpande, G. Mueller, D. H. Reitze, D. B. Tanner, and B. F. Whiting , "Phase effects in the diffraction of light: beyond the grating equation," *Phys. Rev. Lett.* vol. 95, pp. 013901-1~013901-4, 2005.

[21] A.A. Savchenkov, A.B. Matsko, L. Maleki, "White-light whispering gallery mode resonators," *Opt. Lett.* vol. 31, pp. 92~100, 2006.

[22] A. Wicht, K. Danzmann, M. Fleischhauer, M. Scully, G. Miiller, R.H. Rinkleff, " White-light cavities, atomic phase coherence, and gravitational wave detectors," *Opt. Comm.* vol. 134, pp. 1431~1450, 1997.

[23] Shumelyuk, K. Shcherbin, S. Odoulov, B. Sturman, E. Podivilov, K. Buse, "Slowing down of light in photorefractive crystals with beam intensity coupling reduced to zero," *Phys. Rev. Lett.* vol. 93, pp. 243604-1~243604-4, 2004.

[24] L. Solymer, D.J. Webb, and A. Grunnet-Jepsen, *The Physics and Application of Photorefractive Materials,* Oxford, UK: Clarendon Press, 1996.

[25] Z. Deng, De-Kui Qiing, P.R. Hemmer, C.H. Raymond Ooi, M.S. Zubairy, and M.O. Scully, "Time-bandwidth problem in room temperature slow light," *Phys. Rev. Lett.* vol. 96, pp. 023602-1~023602-4, 2006.

[26] P. Yeh, "Two-wave mixing in nonlinear media," *IEEE J. Quantum Electronics,* vol. 25, pp. 484~508, 1989.

[27] A. Dogariu, A. Kuzmich, and L.J. Wang, "Transparent anomalous dispersion and superluminal light-pulse propagation at a negative group velocity," *Phys. Rev. A,* vol. 63, pp. 053806-1~053806-15, 2001.

[28] G. Zhang, R. Dong, F. Bo, and J. Xu, "Slowdown of group velocity of light by means of phase coupling in photorefractive two-wave mixing," *Appl. Opt.* vol. 43, pp. 1167~1186, 2004.

[29] G.E. Stedman, "Ring-laser tests of fundamental physics and geophysics," in *Reports on Progress in Physics*, vol. 60 (6), pp. 615~688, 1997.

[30] G Comptes, "Sagnac," *Rendus*, vol. 157, pp. 708~710, 1913.

[31] M. Sargent, M.O. Scully, W.E. Lamb, *Laser Physic,* Boulder, CO: Westview Press, 1974.

[32] A. Yariv, *Quantum Electronics,* 3rd Ed. Hoboken, NJ: John Wiley & Sons, 1988.

[33] A. E. Siegman, *Lasers,* Sausalito, CA: University Science Books, 1986.

[34] C.S. Liu, B.E. Cherrington, and J.T. Verdeyen, "Dispersion effects in a high-gain 3.39 micron He-Ne maser," *J. of Applied Physics,* vol. 40, pp. 3556~3569, 1969.

[35] W.R. Bennett Jr, "Hole burning effects in a He-Ne optical maser," *Phys. Rev.* vol. 126, pp. 580~594, 1962.

[36] H. Greenstein, "Theory of a single-mode gas laser," *Phys. Rev.* vol. 175, pp. 438~450, 1968.

[37] B.K. Garside, "Mode pulling in ring lasers," *IEEE J. of Quantum Electronics,* vol. QE-5, pp. 97~110, 1969.

[38] F.R. Faxvog, C.N.Y Chow, T. Bieber, and J.A. Carruthers, "Measured pulse velocity greater than c in a neon absorption cell," *Applied Physics Letters,* vol. 17, pp. 192~193, 1970.

[39] K.R. Salit, "Optical switching via quantum interference effects in a multilevel atomic system," Ph.D. Dissertation, Northwestern University, Evanston, IL. At http://www.proquest.com/enUS/products/dissertations/individuals.shtml (2008)

[40] M.S. Shahriar, M. Salit, and J.H. Shapiro, "Model for beat noise in a fast-light enhanced ring laser gyroscope," http://lapt.eecs.northwestern.edu/preprints/beat-noise-in-FRLG.pdf, Jan. 27th 2009.

[41] H.N. Yum, M. Salit, G.S. Pati, S. Tseng, P.R. Hemmer and M.S. Shahriar, "Fast-light in a photorefractive crystal for gravitational wave detection," *Opt. Exp.* vol. 16, pp. 20448~20456, 2008.

[42] Z. Zhu, D.J. Gauthier, and R.W. Boyd, "Stored light in an optical fiber via stimulated Brillouin Scattering," *Science,* vol.318, pp. 1748~1752, 2007.

[43] M. Fleischhauer, and M.D. Lukin, "Quantum memory for photons: Dark-state polariton ," *Phys. Rev. A,* vol.65, pp. 022314-1~022314-15, 2002.

[44] J.J. Longdell, E. Fraval, M.J. Sellars, and N.B. Manson, "Stopped light with storage times greater than one second using electromagnetically induced transparency in a solid," *Phys. Rev. Lett.* vol. 95, pp. 063601-1~063601-4, 2005.

[45] J. Yu, S. Yuan, J. Gao and L. Sun, "Optical pulse propagation in a Fabry–Perot etalon: analytical discussion," *J. Opt. Soc. Am. A,* vol. 18, pp. 2153~2162, 2001.

[46] A. Yariv, "Universal relations for coupling of optical poser between microresonators and dielectric waveguide," *Elec. Lett.* vol. 36, pp. 321~322, 2000.

[47] J.E. Heebner and R.W. Boyd, " 'Slow' and 'fast' in resonator-coupler waveguide," *J. Mod. Opt.* vol. 49, pp. 2629~2648, 2002.

[48] J.E. Heebner, R.W. Boyd and Q. Park, "Slow light, induced dispersion, enhanced nonlinearity, and optical solitons in a resonator-array waveguide," *Phy. Rev. E,* vol. 65, pp. 036619-1~036619-8, 2002.

[49] J. K. S. Poon, J. Scheuer, S. Mookherjae, G. T. Paloczi, Y. Huang, and A. Yariv, "Matix analysis of microring coupled-resonator optical waveguides," *Opt. Exp.* vol. 12, pp. 90~97, 2004.

[50] J.E. Heebner, R.W. Boyd and Q. Park, "SCISSOR solitons and other novel propagation effects in microresonator-modified waveguides," *J. Opt. Soc. Am. B,* vol. 19, pp. 722~737, 2002.

[51] L.F. Stokes, M. Chodorow, and H.J. Shaw, "All single mode fiber resonator," *Opt. Lett.* vol. 7, pp. 288~291, 1982.

[52] J.E. Heebner, V. Wong, A. Schweinsberg, R.W. Boyd, and D.J. Jackson, "Optical transmission characteristics of fiber ring resonators," *IEEE J. Quan. Elect.* vol. 40, pp. 726~737, 2004.

[53] J.E. Heebner and R.W. Boyd, "Enhanced all-optical switching by use of a nonlinear fiber ring resonator," *Opt. Lett.* vol. 24, pp. 847~850, 1999.

[54] J.M. Choi, R. K. Lee and A. Yariv, "Control of critical coupling in a ring resonator-fiber configuration: application to wavelength-selective switching, modulation, amplification, and oscillation," *Opt. Lett.* vol. 26, pp. 1236~1239, 2001.

[55] A. Loayssa, R. Hernández, D. Benito, and S. Galech, "Characterization of stimulated Brillouin scattering spectra by use of optical single-sideband modulation," *Opt. Lett.* vol. 29, pp. 638~641, 2004.

[56] K S. Abedin, "Stimulated Brillouin scattering in single-mode tellurite glass fiber," *Opt. Exp.* vol. 14, pp. 11766~11774, 2006.

[57] S.H. Chin, M.G Herraez, and L. Thevenaz, "Zero-gain slow and fast light propagation in an optical fiber," *Opt. Exp.* vol. 22, pp. 10684~10693, 2006.

[58] R. Pant, M.D. Stenner, M.A. Neifeld, and D.J. Gauthier, "Optimal pump profile designs for broadband SBS slow-light systems," *Opt. Exp.* vol. 16, pp. 2764~2778, 2008.

[59] A.A. Juarez, R. Vilaseca, Z. Zhu, and D.J. Gauthier, "Room-temperature spectral hole burning in an engineered inhomogeneously broadened resonance," *Opt. Lett.* vol. 33, pp. 2374~2377, 2008.

[60] K.Y. Song and K. Hotate, "25 GHz bandwidth Brillouin slow light in optical fibers," *Opt. Lett.* vol. 32, pp. 217~220, 2007.

[61] R.W. Boyd, *Nonlinear Optics,* 3rd Ed. Burlington, MA: Academic Press, 2008.

[62] A. Loayssa, R. Hernandez, D. Benito, and S. Galech, "Characterization of stimulated Brillouin scattering spectra by use of optical single-sideband modulation," *Opt. Lett.* vol. 29, pp. 638~641, 2004.

[63] M. Nikles, L. Thevenaz, and P. A. Robert, "Brillouin gain spectrum characterization in single-mode optical fibers," *J. of Lightwave Tech.* vol.15, pp. 10~19, 1997.

[64] K.S. Abedin, "Observation of strong stimulated Brillouin scattering in single-mode As_2Se_3 chalcogenide fiber," *Opt. Exp.* vol.13, pp. 25~37, 2005.

[65] K.S. Abedin, "Single-frequency Brillouin lasing using single mode As2Se3 chalcogenide fiber," *Opt. Exp.* vol.14, pp. 9~15, 2006.

[66] S. Norcia, S. Tonda-Goldstein, D. Dolfi, J.P. Huignard and R.Frey, "Efficient single-mode Brillouin fiber laser for low-noise optical carrier reduction of microwave signals," *Opt. Lett.* vol. 28, pp. 20~23, 2003.

[67] G. Qin, A. Mori and Y. Ohishi, "Brillouin lasing in a single-mode tellurite fiber," *Opt. Lett.* vol. 32, pp. 15~18, 2007.

[68] G. Qin, H. Sotobayshi, M. Tsuchiya, A. Mori, and Y. Ohishi, "Stimulated Brillouin amplification in a tellurite fiber as a potential system for slow light generation," *Jap. J. of App. Phy.* vol.46 pp. 34~40, 2007.

[69] G.P Agrawal, *Nonlinear Fiber Optics,* 2nd Ed. San Diego, CA: Academic Press, 2001.

[70] K.Y. Song, M. G. Herraez and L. Thevenaz, "Gain-assisted pulse advancement using single and double Brillouin gain peaks in optical fibers," *Opt. Exp.* vol.13 pp. 24~30, 2005.

[71] R.W. Fox, C.W Oates, L.W. Hollberg "Stabilizing diode lasers to high-finesse cavities," *Exp. Method in the phys. Sci.* vol.40, pp. 1~46, 2002.

[72] J.S. Sanghera, I.D. Aggarwal, L.B. Shaw, C.M. Florea, P. Pureza, V.Q. Nguyen, F. Kung, "Nonlinear properties of chalcogenide glass fibers," *J. Optoelec. and Adv. Mat.* vol. 8, No. 6, pp. 2148~2158, 2006.

[73] Y. Makiuchi and H. Matsuura "Development of a low-loss optical circulator," www.furukawa.co.jp/review/fr022/fr22_09.pdf, Nov. 25th 2008.

[74] P. M. Kopera, "Components for fiber optic applications," *Proc. SPIE* vol. 1792, pp. 37~42, 2004.

APPENDIX

A. Analysis of cavity output

In chapter IV, we used Fourier analysis to find the data pulse output of Fabry-Perot (FP) cavity. In this appendix, Laplace and Fourier analysis are presented to calculate the FP output for a particular input pulse. We choose the amplitude of the input data pulse in time domain as

$$\begin{aligned} f(t) &= 1 - e^{-\alpha t} - e^{\alpha(t-b)} \text{(for } 0 < t < b\text{)} \\ f(t) &= -e^{-\alpha t} \text{(for } t > b\text{)} \end{aligned} \tag{A.1}$$

α and b are positive and real numbers. Laplace transform (LT) of the pulse amplitude function is written as

$$L(f(t)) = F(s) = \int_0^{\infty} f(t) e^{-st} dt \tag{A.2}$$

More explicitly, it is $F(s) = \int_0^{\infty} \left(1 - e^{-\alpha t}\right) e^{-st} dt - \int_0^{b} e^{\alpha(t-b)} e^{-st} dt - \left[\int_0^{\infty} e^{-st} dt - \int_0^{b} e^{-st} dt\right]$

Finally, we obtain

$$F(s) = \frac{\alpha}{s(s+\alpha)} + \frac{1}{s-\alpha}\left(e^{-sb} - e^{-\alpha b}\right) - \frac{1}{s} e^{-sb} \tag{A.3}$$

Next, we recall the transfer function of FP

$$H(\omega) = \frac{T e^{-j\frac{n\omega}{c}L}}{1 - R e^{-2j\frac{n\omega}{c}L}} \tag{A.4}$$

where R and T is transmission and reflection coefficient for intensity, respectively, n is refractive index, L is cavity length. According to A.4, H in s-domain is given by

$$H(s)=\frac{Te^{-\frac{ns}{c}L}}{1-Re^{-2\frac{ns}{c}L}} \tag{A.5}$$

The inverse LT of the product of F(s) and H(s) becomes

$$\begin{aligned}&L^{-1}\left(H(s)F(s)\right)\\&=\frac{1}{2\pi j}\int_{\gamma-\infty j}^{\gamma+\infty j}\left[\frac{\alpha}{s(s+\alpha)}\frac{Te^{-\frac{ns}{c}L}}{1-Re^{-2\frac{ns}{c}L}}+\frac{1}{s-\alpha}\left(e^{-sb}-e^{-\alpha b}\right)\frac{Te^{-\frac{ns}{c}L}}{1-Re^{-2\frac{ns}{c}L}}-\frac{1}{s}e^{-sb}\frac{Te^{-\frac{ns}{c}L}}{1-Re^{-2\frac{ns}{c}L}}\right]e^{st}ds\end{aligned} \tag{A.6}$$

Using partial fraction, Eq. A.6 becomes,

$$\begin{aligned}L^{-1}\left(H(s)F(s)\right)=\frac{1}{2\pi j}\int_{\gamma-\infty j}^{\gamma+\infty j}\Bigg\{&\frac{1}{s}\frac{T\exp\left[\left(t-\frac{nL}{c}\right)s\right]}{1-Re\exp\left[-2\frac{ns}{c}L\right]}-\frac{1}{s+\alpha}\frac{T\exp\left[\left(t-\frac{nL}{c}\right)s\right]}{1-Re\exp\left[-2\frac{ns}{c}L\right]}\\&+\frac{1}{s-\alpha}\frac{T\exp\left[\left(t-\frac{nL}{c}-b\right)s\right]}{1-Re\exp\left[-2\frac{ns}{c}L\right]}-\frac{e^{-\alpha b}}{s-\alpha}\frac{T\exp\left[\left(t-\frac{nL}{c}\right)s\right]}{1-Re\exp\left[-2\frac{ns}{c}L\right]}-\frac{1}{s}\frac{T\exp\left[\left(t-\frac{nL}{c}-b\right)s\right]}{1-Re\exp\left[-2\frac{ns}{c}L\right]}\Bigg\}ds\end{aligned} \tag{A.7}$$

$1/\left[1-Re\exp(-2nsL/c)\right]$ is expressed in the form of summation

$$\begin{aligned}L^{-1}(H(s)F(s))=\frac{1}{2\pi j}\int_{\gamma-\infty j}^{\gamma+\infty j}\Bigg\{&\left(\frac{1}{s}-\frac{1}{s+\alpha}-\frac{e^{-\alpha b}}{s-\alpha}\right)\sum_{k=1}^{\infty}TR^{k-1}\exp\left[\left(t-\frac{n(2k-1)L}{c}\right)s\right]\\&+\left(\frac{1}{s-\alpha}-\frac{1}{s}\right)\sum_{k=1}^{\infty}TR^{k-1}\exp\left[\left(t-\frac{n(2k-1)L}{c}-b\right)s\right]\Bigg\}ds\end{aligned} \tag{A.8}$$

Use inverse LT as below

$$L^{-1}\left(\frac{e^{-\tau s}}{s}\right)=\frac{1}{2\pi j}\int_{\gamma-\infty j}^{\gamma+\infty j}\frac{e^{s(t-\tau)}}{s}ds=u(t-\tau) \tag{A.9}$$

$$L^{-1}\left(\frac{e^{-\tau s}}{s+\alpha}\right)=\frac{1}{2\pi j}\int_{\gamma-\infty j}^{\gamma+\infty j}\frac{e^{s(t-\tau)}}{s+\alpha}ds=u(t-\tau)e^{-\alpha(t-\tau)} \tag{A.10}$$

where $u(t-\tau)$ is a step function, i.e. $u(t-\tau)=0$ for $t<\tau$, $u(t-\tau)=1$ for $t>\tau$

Eq.(A.8) gives the FP output pulse in time domain

$$
\begin{aligned}
&L^{-1}\big(H(s)F(s)\big) = f_{out}(t) \\
&= \sum_{k=1}^{\infty} TR^{k-1} u\left(t - \frac{n(2k-1)L}{c}\right) - \sum_{k=1}^{\infty} TR^{k-1} u\left(t - \frac{n(2k-1)L}{c}\right) \exp\left[-\alpha\left(t - \frac{n(2k-1)L}{c}\right)\right] \\
&+ \sum_{k=1}^{\infty} TR^{k-1} u\left(t - \frac{n(2k-1)L}{c} - b\right) \exp\left[\alpha\left(t - \frac{n(2k-1)L}{c} - b\right)\right] \\
&- \sum_{k=1}^{\infty} TR^{k-1} u\left(t - \frac{n(2k-1)L}{c}\right) \exp\left[\alpha\left(t - \frac{n(2k-1)L}{c} - b\right)\right] \\
&- \sum_{k=1}^{\infty} TR^{k-1} u\left(t - \frac{n(2k-1)L}{c} - b\right)
\end{aligned}
\tag{A.11}
$$

Next, let us consider Fourier analysis to obtain the FP output. Assuming that the carrier frequency of the envelop function f(t) is ω_0, Fourier transform (FT) of the input pulse is given by

$$
\begin{aligned}
&F(f(t)) = F(\omega) = \frac{1}{\sqrt{2\pi}} \int_{-\infty}^{\infty} f(t) e^{j\omega_0 t} e^{-j\omega t} dt \\
&= \frac{1}{\sqrt{2\pi}} \int_{0}^{b} \left(1 - e^{-\alpha t} - e^{\alpha(t-b)}\right) e^{j\omega_0 t} e^{-j\omega t} dt + \frac{1}{\sqrt{2\pi}} \int_{b}^{\infty} (-e^{-\alpha t}) e^{j\omega_0 t} e^{-j\omega t} dt \\
&= \frac{1}{\sqrt{2\pi}} \left\{ \frac{-e^{-j(\omega-\omega_0)b}}{j(\omega-\omega_0)} - \frac{e^{-j(\omega-\omega_0)b}}{\alpha - j(\omega-\omega_0)} + \frac{1}{j(\omega-\omega_0)} + \frac{e^{-\alpha b}}{\alpha - j(\omega-\omega_0)} - \frac{1}{\alpha + j(\omega-\omega_0)} \right\}
\end{aligned}
\tag{A.12}
$$

Using Eq.(A.4) and (A.12), inverse FT of $H(\omega)F(\omega)$ is

$$
\begin{aligned}
&\frac{1}{\sqrt{2\pi}} \int_{-\infty}^{\infty} H(\omega) F(\omega) e^{j\omega t} d\omega \\
&= \frac{1}{\sqrt{2\pi}} \int_{-\infty}^{\infty} \frac{1}{\sqrt{2\pi}} \left\{ \begin{aligned} &\frac{-e^{-j(\omega-\omega_0)b}}{j(\omega-\omega_0)} - \frac{e^{-j(\omega-\omega_0)b}}{\alpha - j(\omega-\omega_0)} + \frac{1}{j(\omega-\omega_0)} \\ &+ \frac{e^{-\alpha b}}{\alpha - j(\omega-\omega_0)} - \frac{1}{\alpha + j(\omega-\omega_0)} \end{aligned} \right\} \frac{T e^{-j\frac{n\omega}{c}L}}{1 - R e^{-2j\frac{n\omega}{c}L}} e^{j\omega t} d\omega
\end{aligned}
\tag{A.13}
$$

Defining $\delta = \omega - \omega_0$ and changing the integration variable from ω to δ, Eq.(A.13) yields

$$\frac{1}{\sqrt{2\pi}}\int_{-\infty}^{\infty}H(\omega)F(\omega)e^{j\omega t}d\omega$$
$$=\frac{1}{\sqrt{2\pi}}\int_{-\infty}^{\infty}\frac{1}{\sqrt{2\pi}}\left\{\begin{matrix}\frac{-e^{-j\delta b}}{j\delta}-\frac{e^{-j\delta b}}{\alpha-j\delta}+\frac{1}{j\delta}\\+\frac{e^{-\alpha b}}{\alpha-j\delta}-\frac{1}{\alpha+j\delta}\end{matrix}\right\}\frac{Te^{-j\frac{n(\omega_0+\delta)}{c}L}}{1-Re^{-2j\frac{n(\omega_0+\delta)}{c}L}}e^{j(\omega_0+\delta)t}d\delta \quad (A.14)$$

Again, express $1-Re^{-2jn(\omega_0+\delta)L/c}$ in the form of summation

$$f_{out}(t)=\frac{1}{\sqrt{2\pi}}\int_{-\infty}^{\infty}\frac{1}{\sqrt{2\pi}}\left\{\frac{-e^{-j\delta b}}{j\delta}-\frac{e^{-j\delta b}}{\alpha-j\delta}+\frac{1}{j\delta}+\frac{e^{-\alpha b}}{\alpha-j\delta}-\frac{1}{\alpha+j\delta}\right\}$$
$$Te^{-j\frac{n(\omega_0+\delta)}{c}L}e^{j(\omega_0+\delta)t}\sum_{N=1}^{\infty}R^{N-1}\exp\left(-2j\frac{(N-1)n(\omega_0+\delta)L}{c}\right)d\delta \quad (A.15)$$

Before evaluating the integral value, let us review the definite integral I [1] in complex plan

$$I=\oint_C f(z)e^{jaz}dz \quad .16)$$

where z is a complex variable and C is a closed contour. Fig. A.1 illustrates the possible integral path for different sign of a. Here are the required conditions for f(z). First, if a>0(a<0), then f(z) is analytic in the upper(lower) half-plane except for number of singularities. Second, $\lim_{|z|\to\infty}f(z)=0$, $0\le\arg(z)\le\pi$. The radius R_1 and R_2 for the contours C_1 and C_2, respectively, are infinite. By residue theorem, Eq.(A.16) can be evaluated as

For a>0, $\int_{-\infty}^{\infty}f(x)e^{iax}dx+\lim_{R_1\to\infty}\int_{C_1}f(x)e^{iax}dx=2\pi j\sum$ residues in upper half plane (A.17)

For a<0, $\int_{-\infty}^{\infty}f(x)e^{iax}dx+\lim_{R_1\to\infty}\int_{C_2}f(x)e^{iax}dx=-2\pi j\sum$ residues in lower half plane (A.18)

Right hand side (RHS) in Eq.(A.18) contains minus sign due to clockwise integration.

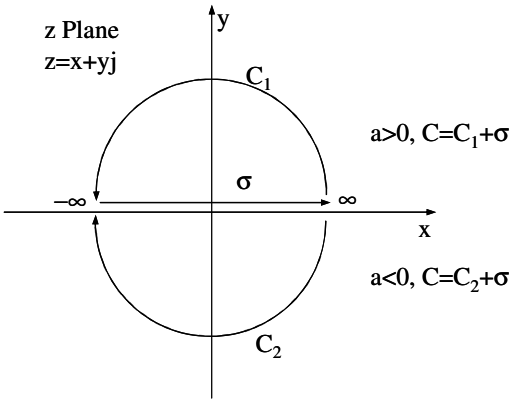

Fig. A.1. Contours.

The conditions for f(z) allows us to use Jordan's lemma [1]. As such, the second terms in the left hand side of Eq.(A. 17,18) becomes zero. It leads us to

$$\text{For a>0, } \int_{-\infty}^{\infty} f(x)e^{iax}dx = 2\pi j\sum \text{residues in upper half plane} \qquad (A.19)$$

$$\text{For a<0, } \int_{-\infty}^{\infty} f(x)e^{iax}dx = -2\pi j\sum \text{residues in lower half plane} \qquad (A.20)$$

Next, we consider the case that the singularities of f(z) are placed on x-axis. Let us assume there is a singularity at z=0. We can estimate Eq.(A.16), following the contours indicated in Fig. A.2. For each case of a, two different closed contours can be considered. Using the integral notation, for a>0, if excluding the singularity, $\oint_C = \int_{-\infty}^{-r} + \int_{C_2} + \int_{r}^{\infty} + \int_{C_1} = 0$. According to Jordan's lemma, $\int_{C_1} = 0$. It leads to

$\int_{-\infty}^{\infty} = -\int_{C_2} = j\pi\delta_0$ where δ_0 is the residue of f(z) at x=0. Note the radius of the semicircular detour around the singularity is infinitesimal, i.e. $\int_{-\infty}^{-r\to 0} + \int_{r\to 0}^{\infty} = \int_{-\infty}^{\infty}$. If including the singularity, $\oint_C = \int_{-\infty}^{-r} + \int_{C_2'} + \int_{r}^{\infty} + \int_{C_1} = 2\pi j\delta_0$. It becomes $\int_{-\infty}^{\infty} = 2\pi j\delta_0 - \int_{C_2'} = j\pi\delta_0$.

For a<0, $\oint_C = \int_{-\infty}^{-r} + \int_{C_2} + \int_{r}^{\infty} + \int_{C_1} = 0$ where the singularity is outside the contour C. It gives $\int_{-\infty}^{\infty} = -j\pi\delta_0$. If including the singularity, $\oint_C = \int_{-\infty}^{-r} + \int_{C_2'} + \int_{r}^{\infty} + \int_{C_1} = -2\pi j\delta_0$. As a result, $\int_{-\infty}^{\infty} = -j\pi\delta_0$. Hence, for the case in which the singularity is placed on the x-axis, we can estimate

$$\text{For a>0, } \int_{-\infty}^{\infty} f(x)e^{jax}dx = j\pi\delta_0 \tag{A.21}$$

$$\text{For a<0, } \int_{-\infty}^{\infty} f(x)e^{jax}dx = -j\pi\delta_0 \tag{A.22}$$

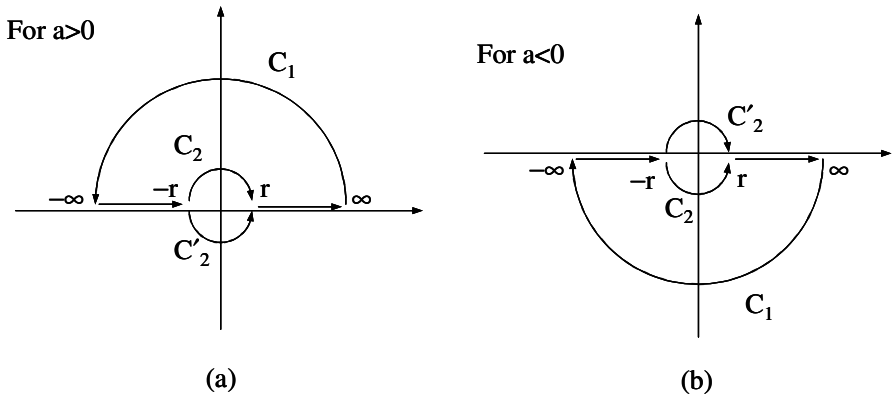

Fig. A.2. Possible integral paths showing that C'_2 includes the singularity but C_2 excludes it for (a) a>0 (b) a<0.

With the Eqs.(A.19~22), we are ready to evaluate the Fourier integral in Eq.(A.15). We expand the factors in $\{\ \}$ of Eq.(A.15) and evaluate term by term

The first term $f_{out1}(t)$ related to $-e^{-j\delta b}/j\delta$ is given by

$$f_{out1}(t)=\frac{1}{2\pi}\int_{-\infty}^{\infty}\frac{j}{\delta}e^{j\omega_0 t}T\sum_{N=1}^{\infty}R^{N-1}\exp\left[-j\frac{(2N-1)n\omega_0 L}{c}+j\left(t-b-\frac{(2N-1)nL}{c}\right)\delta\right]d\delta \quad (A.23)$$

There is singularity at δ=0. According to the range of t, we can use one of the integral paths in Fig. A.2(b) and evaluate Eq.(A.23)

For $t<(2N-1)nL/c$, use the path in Fig. A.2(b)

$$f_{out1}(t)=\frac{1}{2}e^{j\omega_0 t}T\sum_{N=1}^{\infty}R^{N-1}\exp\left(-j\frac{(2N-1)n\omega_0 L}{c}\right) \quad (A.24)$$

For $(2N-1)nL/c<t<b+(2N-1)nL/c$, use the path in Fig. A.2(b)

$$f_{out1}(t)=\frac{1}{2}e^{j\omega_0 t}T\sum_{N=1}^{\infty}R^{N-1}\exp\left(-j\frac{(2N-1)n\omega_0 L}{c}\right) \quad (A.25)$$

For $t > b + (2N-1)nL/c$, use the path in Fig. A.2(a)

$$f_{out1}(t) = -\frac{1}{2} e^{j\omega_0 t} T \sum_{N=1}^{\infty} R^{N-1} \exp\left(-j\frac{(2N-1)n\omega_0 L}{c}\right) \tag{A.26}$$

The second term $f_{out2}(t)$ related to $-e^{-j\delta b}/(\alpha - j\delta)$ is given by

$$f_{out2}(t) = \frac{1}{2\pi} \int_{-\infty}^{\infty} \frac{-j}{\delta + \alpha j} e^{j\omega_0 t} T \sum_{N=1}^{\infty} R^{N-1} \exp\left[-j\frac{(2N-1)n\omega_0 L}{c} + j\left(t - b - \frac{(2N-1)nL}{c}\right)\delta\right] d\delta \tag{A.27}$$

There is singularity at $\delta = -\alpha j$. According to the range of t, we can use C_1 or C_2 in Fig. A.1 and evaluate Eq.(A.27)

For $t < (2N-1)nL/c$, use the contour C_2. According to Eq.(A.20)

$$f_{out2}(t) = -e^{j\omega_0 t} T \sum_{N=1}^{\infty} R^{N-1} \exp\left[-j\frac{(2N-1)n\omega_0 L}{c} + \alpha\left(t - b - \frac{(2N-1)nL}{c}\right)\right] \tag{A.28}$$

For $(2N-1)nL/c < t < b + (2N-1)nL/c$, use C_2 and Eq.(A.20)

$$f_{out2}(t) = -e^{j\omega_0 t} T \sum_{N=1}^{\infty} R^{N-1} \exp\left[-j\frac{(2N-1)n\omega_0 L}{c} + \alpha\left(t - b - \frac{(2N-1)nL}{c}\right)\right] \tag{A.29}$$

For $t > b + (2N-1)nL/c$, use C_2 and Eq.(A.19). As such, there is no singularity inside C_2

$$f_{out2}(t) = 0 \tag{A.30}$$

The third term $f_{out3}(t)$related to $1/j\delta$ is given by

$$f_{out3}(t) = \frac{1}{2\pi} \int_{-\infty}^{\infty} \frac{-j}{\delta} e^{j\omega_0 t} T \sum_{N=1}^{\infty} R^{N-1} \exp\left[-j\frac{(2N-1)n\omega_0 L}{c} + j\left(t - \frac{(2N-1)nL}{c}\right)\delta\right] d\delta \tag{A.31}$$

There is singularity at $\delta = 0$. We can follow the paths in Fig. A.2

For $t < (2N-1)nL/c$, use the path in Fig. A.2(b)

$$f_{out3}(t) = -\frac{1}{2}e^{j\omega_0 t}T\sum_{N=1}^{\infty}R^{N-1}\exp\left(-j\frac{(2N-1)n\omega_0 L}{c}\right) \tag{A.32}$$

For $t > (2N-1)nL/c$, use the path in Fig. A.2(a)

$$f_{out3}(t) = \frac{1}{2}e^{j\omega_0 t}T\sum_{N=1}^{\infty}R^{N-1}\exp\left(-j\frac{(2N-1)n\omega_0 L}{c}\right) \tag{A.33}$$

The fourth term $f_{out2}(t)$ which is related to $e^{-j\delta b}/(\alpha - j\delta)$ is given by

$$f_{out4}(t) = \frac{1}{2\pi}\int_{-\infty}^{\infty}\frac{je^{-\alpha b}}{\delta+\alpha j}e^{j\omega_0 t}T\sum_{N=1}^{\infty}R^{N-1}\exp\left[-j\frac{(2N-1)n\omega_0 L}{c}+j\left(t-\frac{(2N-1)nL}{c}\right)\delta\right]d\delta \tag{A.34}$$

There is singularity at $\delta = -\alpha j$. We can use C_1 or C_2 in Fig. A.1 and evaluate (A.34)

For $t < (2N-1)nL/c$, use the contour C_2. According to Eq.(A.20)

$$f_{out4}(t) = e^{-\alpha b}e^{j\omega_0 t}T\sum_{N=1}^{\infty}R^{N-1}\exp\left[-j\frac{(2N-1)n\omega_0 L}{c}+\alpha\left(t-\frac{(2N-1)nL}{c}\right)\right] \tag{A.35}$$

For $t > (2N-1)nL/c$, use C_1. Due to the absence of the singularity in the contour

$$f_{out4}(t) = 0 \tag{A.36}$$

The fifth term $f_{out5}(t)$ which is related to $-1/(\alpha + j\delta)$ is given by

$$f_{out5}(t) = \frac{1}{2\pi}\int_{-\infty}^{\infty}\frac{j}{\delta-\alpha j}e^{j\omega_0 t}T\sum_{N=1}^{\infty}R^{N-1}\exp\left[-j\frac{(2N-1)n\omega_0 L}{c}+j\left(t-\frac{(2N-1)nL}{c}\right)\delta\right]d\delta \tag{A.37}$$

There is singularity at $\delta = \alpha j$. Using C_1 or C_2 in Fig. A.1 and evaluate Eq.(A.37)

For $t < (2N-1)nL/c$, there is no singularity in C_2.

$$f_{out5}(t) = 0 \tag{A.38}$$

For $t > (2N-1)nL/c$. Use C_1.

$$f_{out5}(t) = -e^{j\omega_0 t} T \sum_{N=1}^{\infty} R^{N-1} \exp\left[-j\frac{(2N-1)n\omega_0 L}{c} - \alpha\left(t - \frac{(2N-1)nL}{c} \right) \right] \qquad \text{(A.39)}$$

In order to verify that LT and FT provide same result, we plot the output pulses from LT Eq.(A.11) as well as FT Eq.(A.24~26, 28~30, 32, 33, 35, 36, 38, 39). For illustration, we choose the FP cavity parameters as free spectral range (FSR) 2.9GHz, Full width half maximum (FWHM) 1.46MHz. We choose $\alpha=1.46\times10^{7}$, $b=7.7616\times10^{-7}$ so that the bandwidth of the pulse spectrum is a half of the cavity FWHM. Fig. A.3 illustrates the input pulse, and the FP outputs of LT and FT. Note the pulse in Fig. A.3.(b) corresponds to that in Fig. A.3.(c). We have shown that the LT and FT presented in Appendix A are the powerful technique to analyze arbitrary pulse propagation through FP cavity.

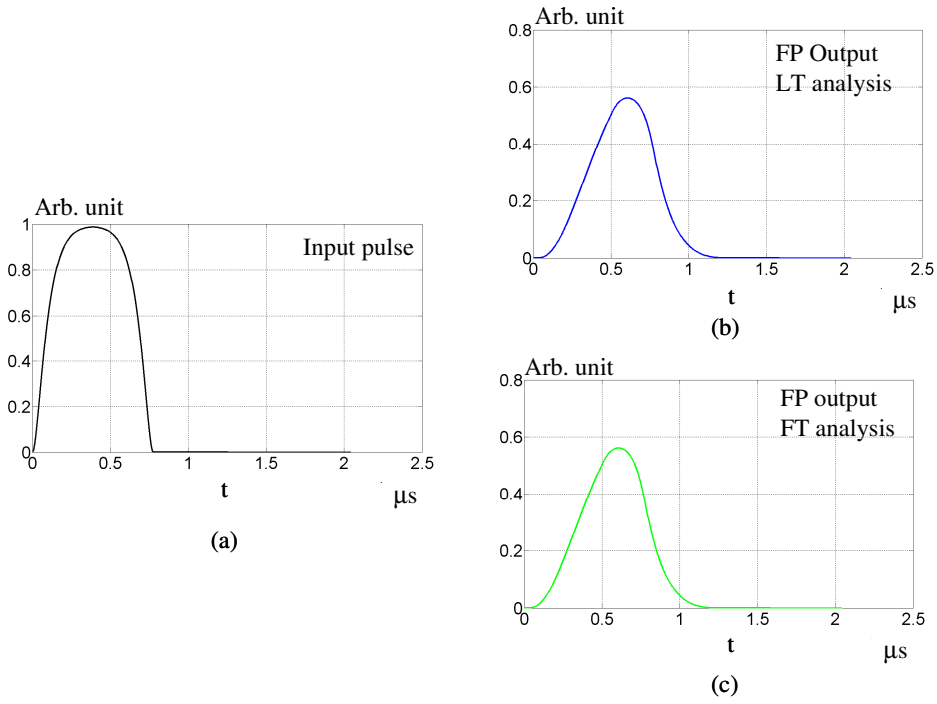

Fig. A.3. (a) input pulse f(t), FP Output calculated by (b) LT (c) FT.

In next section, we present the matlab codes for simulations displayed in Fig. A.3

B. Matlab codes for Fig. A.3

1.Laplace_anlaysis_FPout.m

This code is used to produce the numerical simulation result in Fig. A.3.(b)

```
n=1; %refractive index for vacuum between two Fabry-perot(FP) mirrors.
trans=sqrt(0.001); %Amplitude transmission coefficient for FP mirrors
refl=sqrt(0.999); %Amplitude reflection coefficient for FP mirrors
c=3e8; %Speed of light in free space
Finesse=refl/(1-refl^2); %Finesse of FP
w0=(2*pi*c)/(1550e-9);%Angular frequency for 1550nm light
m=3.3*10^4; %Mode number of 1550nm light in FP
L=2*pi*c*m/(n*w0) %FP cavity length
FSR=c/(2*n*L) %Free spectral range
FWHM_Cavity=FSR/Finesse % FWHM of FP cavity
FWHM_Pulse=FWHM_Cavity*0.5 %Define bandwidth of input pulse spectrum
t0=1/FWHM_Pulse %time width of the input pulse
beta=0.1;
alpha=1/(beta*t0) %alpha in f(t)
b=t0+2/alpha*log(2) % time where the pulse intensity falls a half
N=t0/10^2 %time increment
t=[0:N:3*t0]; %create time domain

%Generate input pulse
f1=1-exp(-alpha*t);
for t_index=1:length(t)
    if t(t_index)>=0&t(t_index)<b
        f2(t_index)=exp(alpha*(t(t_index)-b))
    else
        f2(t_index)=1;
    end
end
f=f1-f2; %input pulse
M=1500; % number of round trip in the FP cavity
%output pulse
T=trans^2;
R=refl^2;
for t_index=1:length(t)
    for k=1:M
        if t(t_index)>=0&t(t_index)<((2*k-1)*n*L/c) % time range
            out(k,t_index)=0; %output for given time range
        elseift(t_index)>=((2*k-1)*n*L/c)&t(t_index)<=((2*k-
1)*n*L/c+b)%time range
            out(k,t_index)=T*R^(k-1)-T*R^(k-1)*exp(-alpha*(t(t_index)-
(2*k-1)*n*L/c))-T*R^(k-1)*exp(alpha*(t(t_index)-(2*k-1)*n*L/c))*exp(-
alpha*b); %output for given time range
        else %time range
            out(k,t_index)=T*R^(k-1)-T*R^(k-1)*exp(-alpha*(t(t_index)-
(2*k-1)*n*L/c))+T*R^(k-1)*exp(alpha*(t(t_index)-(2*k-1)*n*L/c-b))-
T*R^(k-1)*exp(alpha*(t(t_index)-(2*k-1)*n*L/c))*exp(-alpha*b)-T*R^(k-
1); %output for given time range
        end
```

```
    end
    output(t_index)=sum(out(:,t_index)); %Amplitude of output pulse
end
int_output=output.^2; %Output intensity
int_input=f.^2; %Input intensity
figure(1)
plot(t,f1,'b',t,f2,'r') %plot element functions for input pulse
grid on
figure(2)
plot(t,int_input,'b') %plot input pulse
grid on
figure(3)
plot(t,int_output,'b') %plot output pulse
grid on
```

2. Fourier_anlaysis_FPout.m

This code is used to produce the numerical simulation result in Fig. A.3.(c)

```
n=1; %refractive index for vacuum between two Fabry-perot(FP) mirrors.
trans=sqrt(0.001); %Amplitude transmission coefficient for FP mirrors
refl=sqrt(0.999); %Amplitude reflection coefficient for FP mirrors
c=3e8; %Speed of light in free space
Finesse=refl/(1-refl^2); %Finesse of FP
w0=(2*pi*c)/(1550e-9);%Angular frequency for 1550nm light
m=3.3*10^4; %Mode number of 1550nm light in FP
L=2*pi*c*m/(n*w0) %FP cavity length
FSR=c/(2*n*L) %Free spectral range
FWHM_Cavity=FSR/Finesse % FWHM of FP cavity
FWHM_Pulse=FWHM_Cavity*0.5 %Define bandwidth of input pulse spectrum
t0=1/FWHM_Pulse %time width of the input pulse
beta=0.1;
alpha=1/(beta*t0) %alpha in f(t)
b=t0+2/alpha*log(2) % time where the pulse intensity falls a half
N=t0/10^2 %time increment
t=[0:N:3*t0]; %create time domain

%Generate input pulse
f1=1-exp(-alpha*t);
for t_index=1:length(t)
    if t(t_index)>=0&t(t_index)<b
        f2(t_index)=exp(alpha*(t(t_index)-b))
    else
        f2(t_index)=1;
    end
end
f=f1-f2; %input pulse
M=1500; % number of round trip in the FP cavity

%output pulse
T=trans^2;
R=refl^2;
for t_index=1:length(t)

    for k=1:M

        if t(t_index)>=0&t(t_index)<((2*k-1)*n*L/c) % time range
```

```
first(k,t_index)=1/2*exp(j*w0*t(t_index))*T*R^(k-1)*exp(-j*(2*k-
1)*n*w0*L/c);% f_out1
second(k,t_index)=-exp(j*w0*t(t_index))*T*R^(k-1)*exp(-j*(2*k-
1)*n*w0*L/c+alpha*(t(t_index)-b-(2*k-1)*n*L/c)); % f_out2
third(k,t_index)=-1/2*exp(j*w0*t(t_index))*T*R^(k-1)*exp(-j*(2*k-
1)*n*w0*L/c); % f_out3
forth(k,t_index)=-exp(-alpha*b)*exp(j*w0*t(t_index))*T*R^(k-1)*exp(-
j*(2*k-1)*n*w0*L/c+alpha*(t(t_index)-(2*k-1)*n*L/c)); % f_out4
fifth(k,t_index)=0; % f_out5

        elseif t(t_index)>=((2*k-1)*n*L/c)&t(t_index)<=((2*k-
1)*n*L/c+b) % time range
first(k,t_index)=1/2*exp(j*w0*t(t_index))*T*R^(k-1)*exp(-j*(2*k-
1)*n*w0*L/c); % f_out1
second(k,t_index)=-exp(j*w0*t(t_index))*T*R^(k-1)*exp(-j*(2*k-
1)*n*w0*L/c+alpha*(t(t_index)-b-(2*k-1)*n*L/c)); % f_out2
third(k,t_index)=1/2*exp(j*w0*t(t_index))*T*R^(k-1)*exp(-j*(2*k-
1)*n*w0*L/c); % f_out3
forth(k,t_index)=0; % f_out4
fifth(k,t_index)=exp(j*w0*t(t_index))*T*R^(k-1)*exp(-j*(2*k-
1)*n*w0*L/c-alpha*(t(t_index)-(2*k-1)*n*L/c)); % f_out5

        else % time range
first(k,t_index)=-1/2*exp(j*w0*t(t_index))*T*R^(k-1)*exp(-j*(2*k-
1)*n*w0*L/c); % f_out1
second(k,t_index)=0; % f_out2
third(k,t_index)=1/2*exp(j*w0*t(t_index))*T*R^(k-1)*exp(-j*(2*k-
1)*n*w0*L/c); % f_out3
forth(k,t_index)=0; % f_out4
fifth(k,t_index)=exp(j*w0*t(t_index))*T*R^(k-1)*exp(-j*(2*k-
1)*n*w0*L/c-alpha*(t(t_index)-(2*k-1)*n*L/c)); % f_out5
        end
total(k,t_index)=first(k,t_index)+second(k,t_index)+third(k,t_index)-
forth(k,t_index)-fifth(k,t_index);
    end
    output(t_index)=sum(total(:,t_index)); %Amplitude of output pulse
end
int_output=abs(output).^2; % Output pulse intensity
int_input=f.^2; %input pulse intensity
figure(1)
plot(t,f1,'b',t,f2,'r') % element functions for input pulse
grid on
figure(2)
plot(t,int_input,'b') % Plot input pulse
grid on
figure(3)
plot(t,int_output,'b') % plot output pulse
grid on
```

C. Photo images of the experimental setup

Photo images of the experimental setup are shown in this section with brief captions. Detailed information can be found in chapter VI and VII.

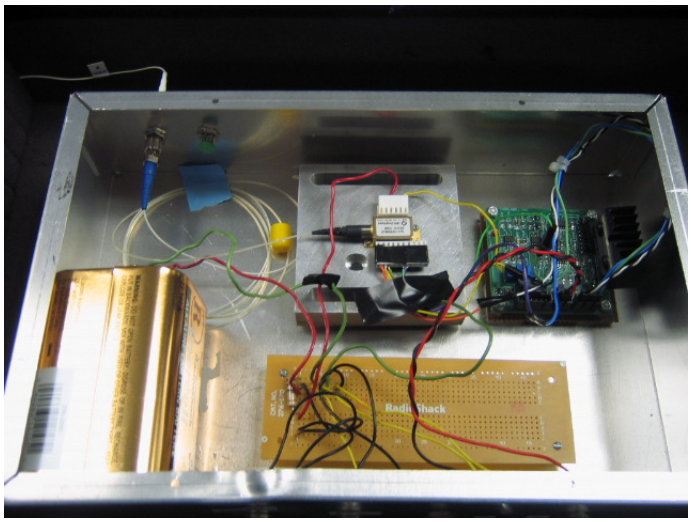

Fig. C.1. 1550nm Laser diode, current driver circuit and temperature controller circuit.

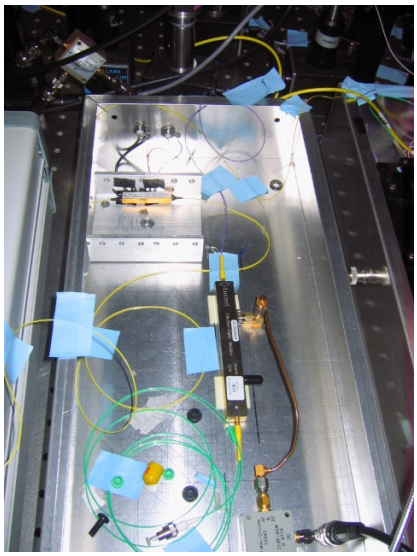

Fig. C.2. 10Gb/s and 2.5Gb/s electro-optic modulators.

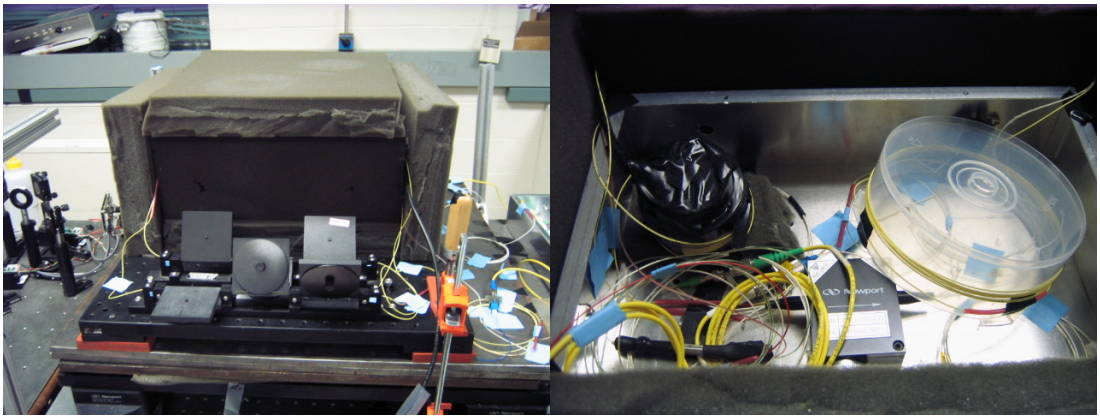

(a) (b)

Fig. C.3. (a) Black foam box mounted on vibration absorber to shield fiber ring cavity from noise (b) Fiber ring cavity inside the box.

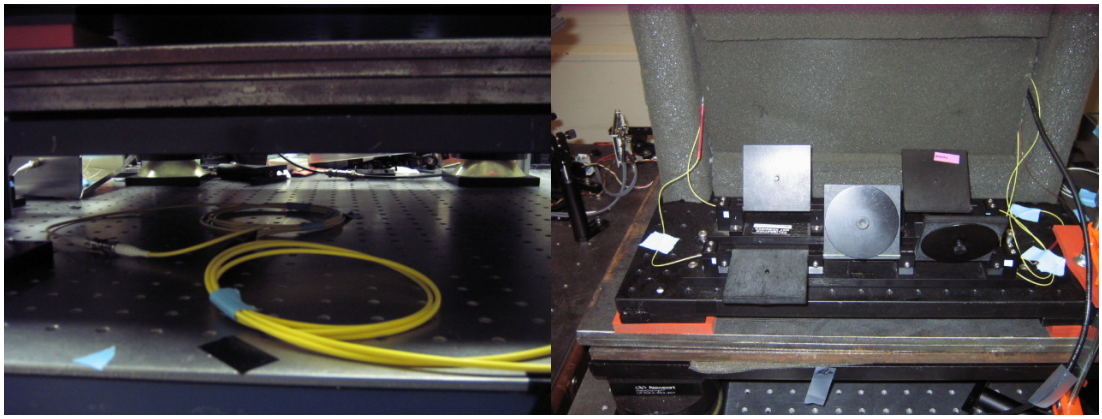

(a) (b)

Fig. C.4. (a) Fiber loop mirror (b) Fiber polarization controller.

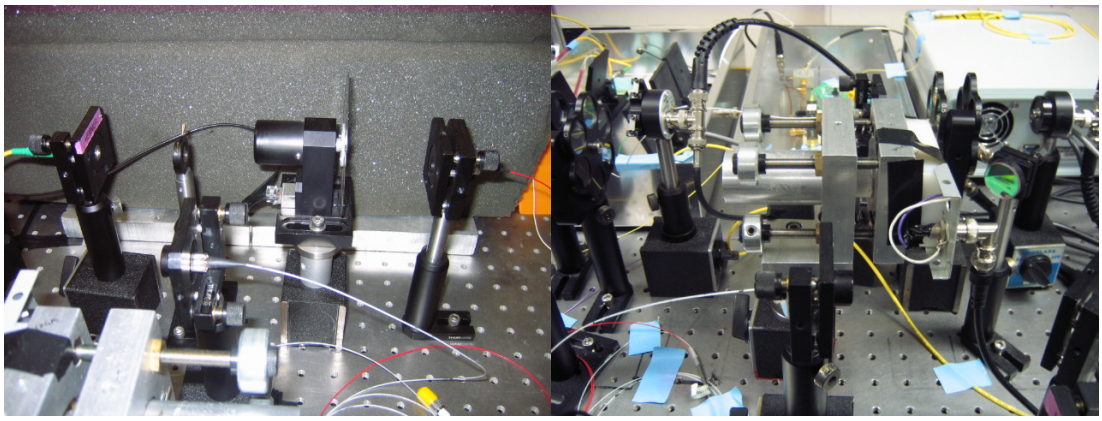

(a) (b)

Fig. C.5. (a) Optical chopper wheel, (b) Fabry-Perot spectrum analyzer.

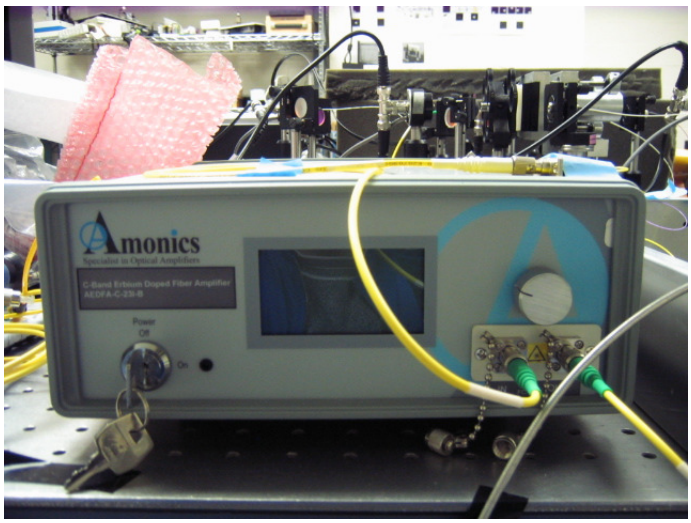

Fig. C.6. Er-doped fiber amplifier (EDFA), Maximum power output is 250mW.

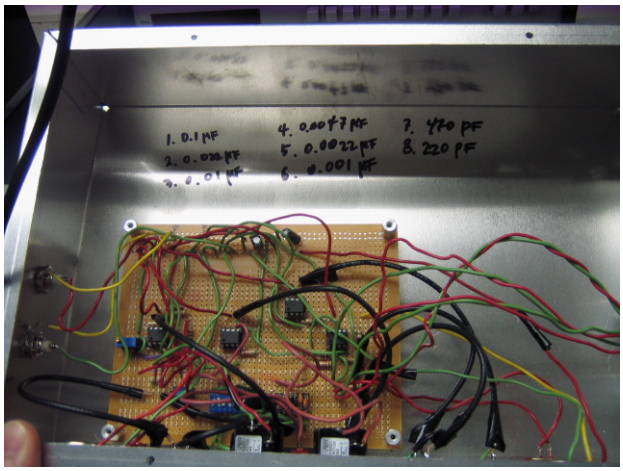

(a)

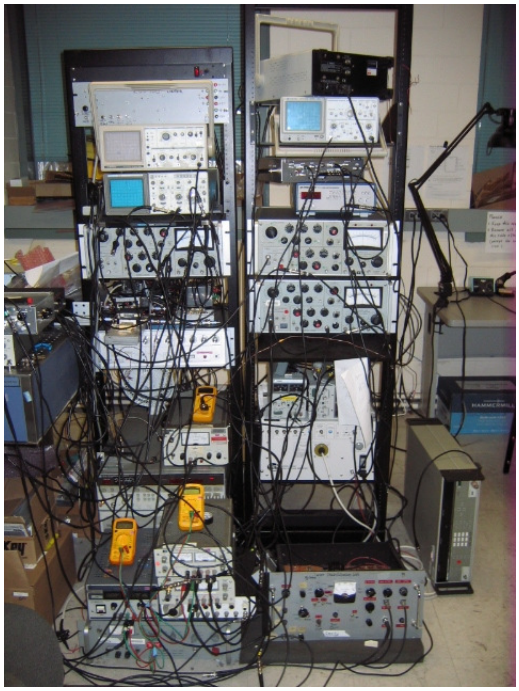

(b)

Fig. C.7. (a) A.C. servo (b) Electronics; Lock-in-amplifiers (LIA), Radio-frequency wave Generator, High Voltage Amplifier, and D.C. supplier.

REFERENCE FOR APPENDIX

[1] Arfken and Weber, “Mathematical methods for physicists” 5th Ed. San Diego, Academic Press, 1995.

VITA

Ho Nam Yum grew up in Korea. He received his Bachelor of Science degree in Ceramic Engineering from Yonsei University in 2000. In the fall of 2001, he came to Texas A&M University and started his master's in Electrical and Computer Engineering (ECE). His research work during his M.S. study was in the area of holography which lead to three journal publications. After finishing his M.S. in 2004, he started working for Liquid Crystal Display (LCD) a business of Samsung Electronics. He obtained thin film fabrication techniques and optical system design. He published 5 patents related to that work. After working for approximately a year and half and gaining valuable experience in the industrial field, he returned to Texas A&M in the fall of 2006 to begin his Ph.D in the ECE Program. His research projects during his Ph.D. study focused on pulse propagation in dispersive medium, fast-light intracavity medium and its applications to gyroscope, data buffer. After completion of his Ph.D, he is looking forward to continuing research work as post-doctor. He may be reached at the Department of Electrical and Computer Engineering, Texas A&M University, 3128 TAMU, College Station, TX 77843-3128, USA. His email is hn_yum@yahoo.com.